



**Politecnico
di Torino**

DIPARTIMENTO DI INGEGNERIA CIVILE

CORSO DI LAUREA MAGISTRALE IN INGEGNERIA CIVILE

TESI DI LAUREA
IN
INGEGNERIA CIVILE

**Calibration of Model Uncertainty
Safety Factors for NLFEMs of
reinforced concrete beams with
shear and flexural failure modes**

RELATORE:
Prof. Paolo Castaldo

LAUREANDO:
Filippo Trombetta

CORRELATORI:
Ing. Diego Gino
Ing. Elena Miceli

ANNO ACCADEMICO 2023 - 2024

Abstract

Pushing the boundaries of the design phase beyond the physical constraints to satisfy the needs imposed by the modern complex structures has led to ongoing advancements in data-processing performance and the development of high-tech software. These tools allow engineers to perform non-linear numerical analysis (NLNA) for reinforced concrete (RC) elements through an exhaustive investigation of the overall structural response under potential load cases. By accounting for non-linearities in material, geometric properties, and boundary conditions, NLNA offers the highest level of approximation for defining the structural model, constitutive laws, and resistance mechanisms. The Codes have proposed several safety formats for the NLNAs of RC structures to address the corresponding source of uncertainty, providing a general framework for integrating them within the Global Resistance Format (GRF) and thus ensuring a balanced tradeoff among safety, efficiency, and cost.

The thesis aims to investigate the discrepancy between numerical models and actual structures' performance by analyzing RC beams that fail in a flexural and shear mode. Comparing experimental results in terms of maximum load with those from NLFE models, this work quantifies the uncertainties that arise during the modeling phase, known as epistemic uncertainties. By assuming 3 model hypotheses that include all possible tensile concrete behaviors and cover any analyst assumptions for its constitutive law in 2 different software, Atena and Diana, the results from 210 Non-Linear Finite Element Analyses (NLFEAs) were gathered. The approach allows us to obtain 6 solution strategies that guarantee a comprehensive characterization of the global resistance model uncertainty random variable. Consequently, a probabilistic analysis was conducted employing the Bayesian method, avoiding the possibility of making a work that is just a representation of a narrow set of RC structures. The purpose is to pursue general outcomes that could contribute to the development of the next generation of Eurocodes. The overarching idea of this strategy is to first apply a statistical inference procedure to detect the appropriate probabilistic model and fit it to the data sample through the estimation of its parameters. After that, the process involves the calibration of the model uncertainty safety factor by generating new information using the Bayesian updating process. The result is the definition of posterior probability functions, which reflect both the prior information and the new data. The strength of this approach lies in its ability to incorporate into the analysis existing knowledge from the literature. This procedure performs the updating operation twice, leading to more robust results and a reduction of model uncertainty, enhancing the reliability of the findings.

Finally, after estimating the average posterior probability distribution, which is adopted to represent the resistance modeling uncertainty random variable θ and deleting the influence of experimental uncertainty from its key statistical parameters, the resistance model uncertainty partial safety factor γ_{Rd} can be estimated. The assessment assumes 3 different reliability indexes, 2 FORM factor scenarios, and various service life cases, in line with the GRF of the fib Model Code for concrete structures 2010. These options ensure safety, reliability, and feasibility in the design process by choosing a conservative value that adequately tackles model uncertainties.

Keywords: NLNA, RC Beams, Safety Formats, Epistemic Uncertainty, Safety Factor, Bayesian Approach

Contents

Introduction	1
1 Chapter 1	7
1.1 Global Resistance Format (GRF)	7
1.1.1 General aspects	7
1.1.2 NLNA procedure	9
1.1.3 Safety Formats within the Global Resistance Method (GRM)	11
2 Chapter 2	15
2.1 Experimental benchmark	15
2.1.1 Selection Criteria	15
2.1.2 Test typologies	16
2.1.3 Database	17
Specimens experiencing flexural failure	18
Specimens experiencing shear failure	25
3 Chapter 3	35
3.1 ATENA and DIANA: Modeling Assumptions and General Framework	35
3.1.1 Material hypothesis	35
3.1.2 Geometry characterization	37
3.1.3 Overview of the Proposed Hypotheses	38
3.1.4 General framework for modeling a beam in Atena and Diana	40
4 Chapter 4	41
4.1 NLFE Models	41
4.1.1 Identification of failure mechanism in RC beams	41
Bending failure	41
Shear failure	42
4.1.2 Finite Elements Models: NLNAs results	47
Specimens experiencing flexural failure	47
Specimens experiencing shear failure	51
5 Chapter 5	56
5.1 Uncertainty in NLNA Models of RC Beams	56
5.1.1 Model uncertainty safety factor	56
5.1.2 Assessing model uncertainty	57
Beams experiencing flexural failure	58
5.1.3 Statistic Inference	60
Chi-Squared (Pearson) Test	62

	Anderson-Darling Test	62
	Jarque-Bera Test	63
	Lilliefors Test	64
5.1.4	Calibration of model uncertainty safety factor	65
	Bayes approach A	65
	Bayes approach B	70
5.1.5	Influence of Experimental Uncertainty	72
5.1.6	Assessment of the partial safety factor for resistance model uncertainty	75
5.2	Beams experiencing shear failure	80
5.2.1	Statistic Inference	82
5.2.2	Calibration of model uncertainty safety factor	83
	Bayes approach A	83
5.2.3	Influence of Experimental Uncertainty	87
5.2.4	Assessment of the partial safety factor for resistance model uncertainty	88
	Bibliography	92

Introduction

Non-linear numerical analysis (NLNA) for reinforced concrete (RC) structural elements is an advanced method for designing and evaluating new and existing structures. It enables a more accurate analysis of structural behavior under real-world loading conditions by accounting for non-linearities in material, geometric properties, and boundary conditions [26]. Material non-linearity occurs when the constitutive law no longer follows the linear stress-strain relationship and the induced stress causes deformations beyond the yield point. It leads to permanent changes in the initial material's shape, necessitating ongoing updates to the stiffness matrix throughout the deformation process, considerably increasing computational demand. By considering geometric non-linearity, NLNA allows for structural analyses under large displacements and rotations, accounting for load redistributions and changes in the interaction among the different structural elements. Non-linearity in boundary conditions occurs when the supports or the constraints within the structure change their properties and responses under the loading phase. An example of this can be observed during the modeling of soil-structure interaction through non-linear spring stiffness. The non-linear approach can be particularly useful in scenarios where structures are exposed to dynamic forces like seismic actions or strong winds, as well as in foundation and retaining wall designs [48].

In the field of structural engineering, the current research is focused on overcoming physical limitations in designing increasingly complex structures. This pursuit is helped by ongoing advancements in computational capabilities, deeper knowledge of new advanced materials and their resistance mechanisms, and the development of smarter software. Furthermore, automated and parametric design techniques, such as Building Information Modeling (BIM) and finite element analysis, are rapidly advancing and becoming integral to the field. This growth is driven by increasing concerns for sustainability, efficiency, and safety, which are now essential for a project in all its stages. In parallel with these advancements in computational tools, there is the introduction of non-linear finite element analysis (NLFEA). This method typically yields higher design resistances compared to local structural analysis because failure in the most critical cross-section of a structure does not necessarily imply the failure of the overall structure. Instead, this latter can undergo plastic deformations and force redistributions, which often prevent immediate failure. Considering the real material properties, this method can reveal the "hidden" bearing capacity of the structures, neglected instead in linear calculations, empowering the engineers to push the boundaries of present and future design possibilities. Therefore, in evaluating the global behavior of a structural member, like columns or beams, or an entire structure, adopting NLFEA turns out to be an effective computational tool. This effectiveness is demonstrated by [30], where a comparison between local and global structural analyses of several beams, showed that higher design loads were obtained with non-linear analysis [15].

Concrete is a widely used construction material and one of the major contributors to

global greenhouse gas emissions. The European Cement Association, commonly known as Cembureau, has drawn up a 5C approach to reduce concrete’s environmental impact by fully exploiting its mechanical properties and minimizing unnecessary usage [10]. Implementing successfully this strategy requires a comprehensive understanding of the material’s performance as well as the software’s accuracy during the design and maintenance phases [44]. This is shown by Slobbe et al.’s study [47], which illustrates how a detailed physical concrete model can reveal significant structural reserves compared to standardized methods. The fib Model Code further highlights how the effort, in terms of time spent on an analysis, is correlated with its accuracy. This concept is depicted in figure 1, which introduces the “level of approximation” approach: increasing the level of approximation, so does the accuracy and the time required to solve the problem. The NLNA, being an advanced numerical simulation, operates at the highest levels of approximation.

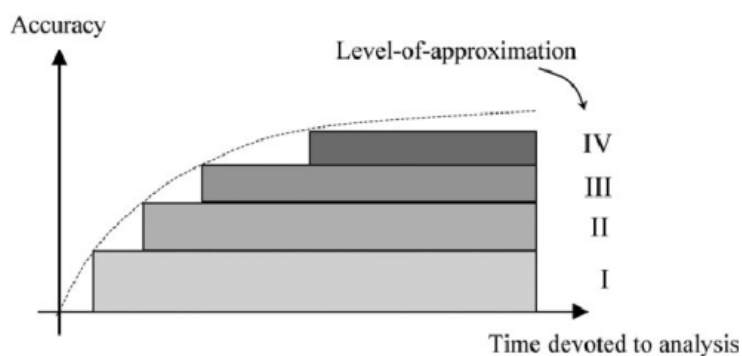


Figure 1: Levels of approximation [22]

In a country like Italy, which boasts a rich architectural heritage and numerous buildings from the last century, there is a growing need to re-assess old concrete structures. Ensuring that these facilities remain safe for use, even beyond their design lifetime, is leading the interest in this type of advanced analysis technique. These approaches can comprehensively account for factors such as aging, long-term effects, environmental conditions, and retrofitting measures, accurately predicting how these alterations affect structural behavior [13]. Similarly, also other countries are working on it, to ensure their infrastructures meet the population’s needs and comply with the new Codes. For example, in the Netherlands, the Dutch Ministry of Infrastructure and the Environment demonstrated the effectiveness of using NLFEAs over traditional methods by reassessing the load-bearing capacity of existing RC bridges. This need emerged from the increase in heavy traffic and the requirement to readjust emergency lanes. Safety verifications during this project showed that traditional local analysis methods did not fulfill the standards for some structures. This could have induced changes, significantly impacting economic, environmental, and socio-functional spheres. However, by adopting alternative methods such as NLFEA to verify structural carrying capacity, these structures could continue to safely bear loads for several more years with just refurbishment and periodic checks. The Dutch Ministry has pursued this approach, despite the lack of restrictive and specific norms and regulations in building codes for implementing this new method and conducting non-linear analyses [3].

This innovative method of designing and verifying the structures gathers global attention. A notable example is the project undertaken by Chile following one of the worst natural disasters in the country’s history: the 2010 earthquake. This tragedy underlined

the weaknesses of RC walls in buildings that were not designed to meet the latest codes, revealing their vulnerability to strong ground motions with resulting flexural damages. Consequently, numerous static and dynamic nonlinear analyses were conducted to evaluate the effects of various design enhancements, such as thicker walls, increased steel ratios, and the decoupling of the main wall. These improvements aimed to enhance durability and minimize earthquake-related damage to residential buildings. These enhancements involve refining the level of detail on the mechanical behavior of the RC preventing the structure's poor performance during future earthquakes. The building's seismic performance was predicted using Performance-Based Design (PBD), which employed non-linear modeling of structural components. This approach generated valuable data for structural engineers, helping to minimize future building damages during extreme events. Moreover, non-linear static and time-history analyses provided an accurate assessment of the material's mechanical behavior, including the detection of undesired phenomena such as sudden brittle failures, like those seen in shear failure [39].

Aligning with the ideas behind these projects and the objective to bridge the performance gap between the numerical models realized with software, which are mathematical representations, and real-world structures, this thesis analyzes RC beams exhibiting both flexural and shear failure. Comparing experimental results in terms of maximum load with those from software, this study helps future users minimize the uncertainties related to the model, known as epistemic uncertainties. Accurately predicting the actual behavior of a structure and determining the most probable value of the resistance, which is the mean value, enables the engineers to tackle the main challenge in performing this type of analysis: quantifying epistemic uncertainties. Even a perfect model is subject to numerical approximations and inherent uncertainties, which must be well-known and weighted when aiming to precisely represent the real structure in all its endless complexities. Each non-linear analysis involves a solution strategy drawn up by the analysts based on their experience and knowledge of the specific case. Different modelers can implement various solution strategies for the same structure, with different assumptions, and there is no universally better approach. Engen et al. [18] described the solution strategy as "choices regarding force equilibrium, kinematic compatibility, and constitutive relations". Each of these choices in a finite element solution contribute to the model uncertainty, either explicitly or implicitly: explicit contributions arise because different models include different approximations of physical reality, instead the implicit part emerges from everything not explicitly considered but still affecting the epistemic uncertainty. Therefore, it's crucial to be aware of these factors and understand how they impact the results. By using 3 model hypotheses that encompass all possible actual tensile concrete behaviors and embrace any analyst assumptions for the tensile concrete constitutive law, the results from 210 Non-Linear Finite Element Analyses (NLFEAs) are collected. This information is derived from the non-linear models implemented by applying the 3 different solution strategies in 2 software, Atena and Diana. Dividing the analysis into 2 cases, flexural failure and shear failure, the model uncertainty is defined as the ratio between the experimental result and the result assessed with NLFEA. According to the literature, such as the JCSS Probabilistic Model Code [31], the model uncertainty is a random variable that fits a log-normal probability distribution. Therefore, for each of the 3 model assumptions adopted, the key distribution parameters are determined and updated with new information through the Bayesian method. It involves 2 distinct approaches: Approach A uses non-informative prior distributions to allow the data to speak for themselves without the influence of strong prior beliefs. In contrast, Approach B assumes informative

prior distributions based on existing knowledge from previous research. As described in the MC2020 draft, the Bayesian updating procedure is used to determine the model uncertainty safety factor γ_{RD} for 3 different reliability indexes, 2 FORM factor cases, and multiple service life scenarios [15].

Even though the thesis' objective is to accurately evaluate γ_{RD} , the process of achieving this coefficient involves more than just considering the relationship between the predicted and experimental failure loads. Another crucial factor in assessing a finite element solution strategy is its ability to approximate the entire experimental load-deformation curve, closely matching both the load and deformation at the yield and failure points. This requirement is essential because one of the main purposes of adopting a non-linear approach is to provide engineers with a more accurate insight into real structural behavior.

Below, scheme 2 shows a summary of the entire process developed throughout this master's thesis.

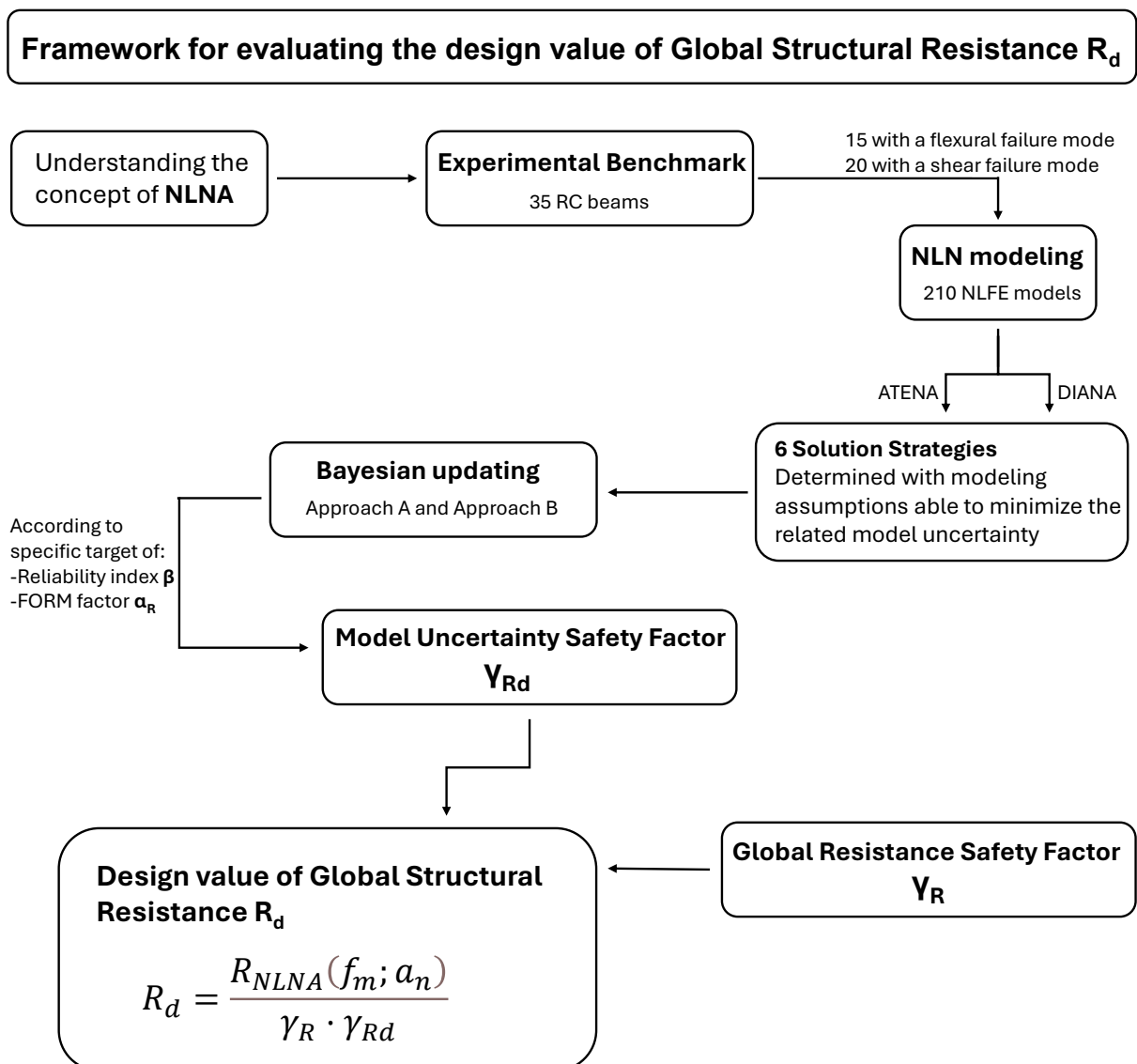


Figure 2: Framework for evaluating the design value of Global Structural Resistance R_d

Symbol and Notation Glossary

Symbol	Description
R_d	global structural resistance
F_d	global design external actions
E_d	design acting forces in the local analysis
R_d	sectional resistance in the local analysis
R_{NLNA}	global structural resistance estimated by nonlinear numerical analysis
R_{exp}	experimental value of the global structural resistance
$R_{NLFEA,i}$	global structural resistance estimated by non-linear numerical analysis with reference to the i th modeling hypothesis $i = 1-6$
M_j	j th modeling hypothesis to define the non-linear structural model with $j = 1-6$
X	vector of basic variables included into the resistance model
Y	vector of variables that may affect the resisting mechanism but are neglected in the resistance model
β	first-order-reliability-method (FORM) sensitivity factor
Z	quantile of the reliability index
θ	global resistance model uncertainty random variable (observed) with $i = 1-15$ for the flexural case and $i = 1-20$ for the shear one
μ_θ	mean value of the resistance model uncertainty random variable
CV_θ	coefficient of variation of the resistance model uncertainty random variable
σ_θ	variance of the resistance model uncertainty random variable (observed)
ϵ	experimental uncertainty random variable
μ_ϵ	mean value of the experimental uncertainty random variable
CV_ϵ	coefficient of variation of the experimental uncertainty random variable
θ_{act}	actual resistance model uncertainty random variable

Symbol	Description
$\delta_{R,m}$	mean-to-mean deviation
V_R	coefficient of variation of the global structural resistance
$\mu_{\vartheta,act}$	mean value of the actual resistance model uncertainty random variable
$CV_{\vartheta,act}$	coefficient of variation of the actual resistance model uncertainty random variable
z_j	vector which groups the statistical parameters of the lognormal distributions associated to the updating information for each structural model with $j = 1-6$
Z_A	vector of the average statistical parameters for the Approach A
Z_B	vector of the average statistical parameters for the Approach B
A_s	cross-sectional area of the longitudinal reinforcement in the compression area
A'_s	cross-sectional area of the longitudinal reinforcement in the tensile area
L	total length of the RC columns
d	effective height of RC beam
ρ	longitudinal reinforcement ratio
ρ_{sw}	stirrups reinforcement ratio
s	longitudinal spacing between shear reinforcements
f_c	experimental value of the cylinder concrete compressive strength
f_y	experimental value of the reinforcement tensile yielding strength
f_u	experimental value of the reinforcement tensile ultimate strength
P_y	beam yield point
P_u	beam ultimate point
δ_y	beam deformation at the yield point
δ_u	beam deformation at the ultimate point
γ_{Rd}	Model Uncertainty Safety Factor
γ_R	Global Resistance Safety Factor
$\varepsilon_{s,max}$	peak strain attained in the tensile primary reinforcement at failure
γ_{FM}	failure mode-based safety factor

Chapter 1

1.1 Global Resistance Format (GRF)

1.1.1 General aspects

The fib Model Code MC2010 [22] introduces a new method based on four levels of approximations (LoA), as shown in the image 1, for evaluating the design resistance of RC beams: levels I, II, III, and IV. As the level increases, so do the complexity, accuracy, and time needed to evaluate structural safety. Level I is grounded on the limit states approach and partial safety factor method, which continues to remain valid and widely used in practical applications and Codes. It's based on cross-sectional analysis: design acting forces E_d are compared against resisting forces R_d , such as bending moment, shear, and axial forces, ensuring always $E_d < R_d$. In this context, internal actions are assessed using linear elastic analysis, which combines the effects of external loads through linear superposition. On the other hand, the sectional internal resistance is evaluated based on the ultimate limit state considered. This method is known as the local approach because it focuses exclusively on sectional verifications of structural members, without accounting for the overall behavior of the entire element or the possibility of a progressive redistribution of internal forces within the RC structure. This type of analysis is useful and efficient when lower levels of approximation are tolerable since it relies on simplified assumptions for defining the structural model, constitutive laws, and resistance mechanisms. On the positive side, it significantly increases time efficiency and cost-effectiveness [8].

Unlike, a global approach becomes indispensable when greater accuracy and precision in structural reliability assessments are needed. This procedure, ranked as level IV, involves advanced numerical methods like NLFEMs, which allow the engineers to encompass the progressive damage and the structure's ability to redistribute internal forces under specific loading conditions. The underlying principle is that failure in the most critical cross-section of a structure does not necessarily lead to the failure of the entire building. Neglecting the structure's capacity for rearrangement of internal stresses can cause an important underestimation of its resistance, potentially generating unnecessary cost inflations and environmental damages. The method is based on the comparison between the global design external actions F_d , under a specific loading combination, with the global design structural resistance R_d through the following equation:

$$F_d \leq R_d \quad \text{with} \quad R_d = \frac{R_{\text{rep}}}{\gamma_R \cdot \gamma_{Rd}} \quad (1.1)$$

Where:

- R_{rep} is the global resistance of the structure.
- γ_R represents the global resistance safety factor for the aleatory uncertainties.
- γ_{Rd} corresponds to the global safety factor for the epistemic uncertainties.

The calibration process of these 2 safety factors is conducted separately, without any kind of interaction or influence between them, as demonstrated in this thesis and [26].

Nowadays, the global resistance format is regarded as the most effective design tool for the safety assessment of RC members. It allows for the management of the different sources of uncertainties through appropriate global safety factors, which are used to define the global design resistance of a structure [8]. Moreover, there is no unique procedure to evaluate R_d : various approaches can be implemented, each based on different levels of deepening of the probability theory. The accuracy in the estimate of the structural behavior can be progressively refined through a more accurate assessment of the uncertainties involved in the process. Consequently, in line with the general approach of the Global Resistance Format (GRF) proposed by fib Model Code 2010, the design resistance R_d may be evaluated via different safety formats, such as [2]:

- Probabilistic Method (PM)
- Partial Factor Method (PFM)
- Estimate of the Coefficient of Variation (ECOV)
- Global Resistance Factor (GRF)
- Global Safety Format (GSF)
- Strain-Based Method (SBM)

By applying the probabilistic method, the global structural resistance R is fully described by a suitable probabilistic distribution, which is tailored using NLFEMs. Based on the required level of reliability and depending on whether the structure is new or existing, the global design structural resistance can be assessed as follows:

$$R_d = \frac{1}{\gamma_{Rd}} \cdot R(\alpha_R, \beta) \quad (1.2)$$

Where:

- $R(\alpha_R, \beta)$ represents the quantile of R distribution corresponding to a target reliability index β , and a FORM sensitivity factor α_R

Although this procedure demands a high computational effort, it sometimes appears to be the only safety format capable of accurately assessing R . This is because it can consider factors such as the variability in the material's strength within the structure, which may be affected, among other factors, by interactions of different materials strengths (i.e. dowel action, tension stiffening effect) and aging. Being able to consider these variations the PM can provide an accurate and comprehensive evaluation of the structure's reliability, effectively capturing the actual variability of material properties and the effects of their combination.

Reducing computational demands is possible and highly desired by adopting global resistance methods (GRMs), which are the alternative safety formats mentioned earlier. These simplified approaches are valuable only if they can effectively capture the fundamental mechanical aspects that control the structural behavior of RC structures, like crack propagation and the failure mode. This latter is strongly influenced by the selection of the material properties adopted to set up the NLFEMs. The choice of the correct information and an accurate model calibration phase can result in changes in the failure mode, as different resisting mechanisms may involve concrete or reinforcement steel and even different regions of the structure [46].

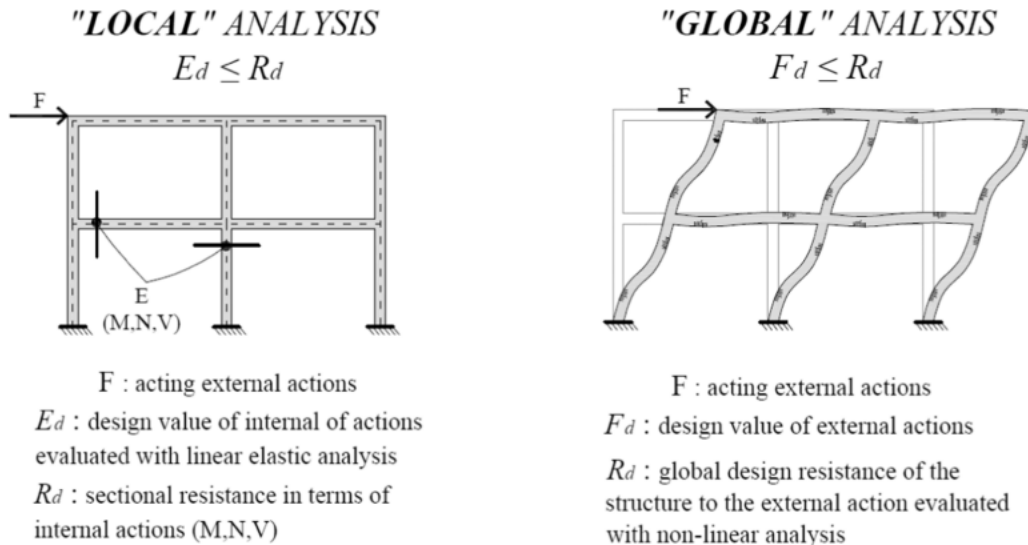


Figure 1.1: Local structural analysis VS Global structural analysis [8]

1.1.2 NLNA procedure

Although the introduction of NLNA may offer several advantages already highlighted in detail previously, it would entail likewise some disadvantages, especially in terms of time, cost, and expertise required to fully interpret the outcomes. Gradually more engineers, designers, and modelers will opt to approach projects using non-linear numerical analysis, whether for new construction or just refurbishment. Despite the initial problems that there may be dealing with non-linear analysis, only through this consistent effort, it will become the standard in design practice. Moreover, the next generation of international codes is expected to integrate into the standard structural verification procedure, the option of using NLNA, further encouraging its adoption.

This diffusion process shares many points in common with the adoption of the Building Information Modeling (BIM) methodology. With the support of new regulations, it is increasingly becoming mandatory to participate in public works contracts above a certain amount of money. For the BIM, Europe has published a "Handbook for the Introduction of Building Information Modelling by the European Public Sector", which provides training, support, and guidance to the stakeholders. The handbook guarantees a harmonized and standardized procedure that allows them to manage information with BIM methodology throughout the entire lifecycle of a built asset [27].

Similarly, for NLNA, a well-defined procedure must be set up and declared. The process currently in use involves three stages:

- i. Characterization of input variables and model definition (i.e., parameters, constitutive laws used)
- ii. NLFE simulations with software like ATENA, and DIANA
- iii. Post-processing of the results

These steps ensure a non-misleading and systematic approach to non-linear analysis, facilitating its effective application in structural design. The final step, iii, should be seen as a critical phase: if the results don't fulfill the initial expectations that an engineer must have before tackling any problem, an iterative process between ii and iii has to be undertaken. This would allow for achieving final results that are critically investigated and only then accepted.

Analyzing each step in more detail, the first implies gathering all the necessary information and knowledge about the structure to be analyzed. This includes the modeler's choice, based on his experience, of the representative values for mechanical and geometrical properties, and the definition of the solution strategy. This latter encompasses making modeling assumptions about the iterative solution methods to be adopted, ensuring equilibrium and kinematic compatibility through appropriate constitutive models. This initial step has to be meticulously suited to the specific problem the designer is addressing and it's crucial for a well-done NLNA. The subsequent phases are intrinsically dependent on this one and even if in the future there may be guidelines and a handbook to help the designers, it will remain heavily based on their expertise. It's important to underline that there is not only a unique correct solution universally valid, but the different possible outcomes are shaped by the designer's skills and judgment. The second step involves the structural analysis itself, implementing within the software the choices selected in the previous phase. This part is strongly dependent on the used software, and with a deep knowledge of the system, the analyst can enhance the accuracy and precision of the solution. The last part entails a critical analysis of the NLNA outcomes. This investigation is even more crucial in a priori analyses, where the real structural behavior of the RC element is unknown, and no information about the real failure mode is available. The analyst has to be capable of differentiating between pure numerical failure and physical collapse. The number of iterations needed to reach the satisfaction of convergence criteria can provide important insights: a high number of iterations could indicate the development of important cracks but at the same time it may signal a numerical error. Therefore, in such cases, the results obtained by the software from that point onward can't be considered reliable [21].

According to Castaldo et al. [8], the failure mode identified through an NLNA is unequivocally characterized by achieving the ultimate strain of concrete and/or steel reinforcement in specific areas of the element under investigation, consequently leading to a global failure mechanism. For this reason, reaching the ultimate material strain simultaneously with the global failure can be assumed as an indicator that the analysis has successfully captured the real structural response. However, as mentioned in the previous subsection, the NLNA is sensitive to the values of material properties chosen to run the simulation. This sensitivity can result in different failure modes within, for instance, the probabilistic set of NLNAs as shown in [26].

In the following sections, the entire process will be explored step by step, with a post-processing phase dedicated to assessing the model uncertainty using the Bayesian approach. The entire path has been followed twice: once by running the simulations with

ATENA and then with DIANA, ending the journey by analyzing and comparing the statistical parameters.

1.1.3 Safety Formats within the Global Resistance Method (GRM)

The limit state condition within the Global Resistance Format can be reformulated, following the equation 1.1, as follows:

$$F_d \leq R_d \quad \text{where} \quad R_d = \frac{R_{\text{NLNA}}(f_{\text{rep}}; a_{\text{rep}})}{\gamma_R \cdot \gamma_{R_d}} \quad (1.3)$$

The $R_{\text{NLNA}}(f_{\text{rep}}; a_{\text{rep}})$ above mentioned is simply the explicit representation of R_{rep} in equation 1.1. Indeed, it indicates the global resistance of the structure estimated through the selected safety format. The f_{rep} and a_{rep} are, respectively, the representative values of materials and geometric properties used as input in the NLNAs. The uncertainties, placed in the denominator of equation 1.3, have been already divided earlier according to their sources:

- γ_{R_d} has been estimated in this thesis and other research papers, achieving a comprehensive characterization for 2D and 3D NLNAs of slender members, such as beams, and columns, subjected to quasi-static monotonic or cyclic loads. This safety coefficient remains constant and invariant across all the various safety formats presented and the next chapters are dedicated to its analysis and assessment [19].
- γ_R is evaluated starting from the hypothesis that the global structural resistance fits a log-normal probabilistic distribution, using the following equation:

$$\gamma_R = \frac{\exp(\alpha_R \beta_t \cdot V_R)}{\delta_R} \geq 1.00 \quad \text{with} \quad V_R \leq 0.3 \quad (1.4)$$

Equation 1.4 is not an exact expression but rather an approximation, which remains valid until the value of V_R equals 0.20. It shows minimal discrepancies compared to the actual equation for values up to 0.30. In equation 1.4, δ_R encompasses the influence related to the bias factors of geometrical properties deviations. Specifically, it's obtained by multiplying $\delta_{R,g}$ and $\delta_{R,m}$ as shown in equation 1.5:

$$\delta_R = \delta_{R,m} \cdot \delta_{R,g} \quad (1.5)$$

Where:

- $\delta_{R,m}$ is known as mean-to-mean deviation. It quantifies the ratio between the mean value of the global structural resistance obtained from a probabilistic analysis, $\mu_{R,m}$, and the value derived from performing an NLNA, setting as representative values for material properties the mean values, and for geometric characteristics the nominal values, $R_{\text{NLNA}}(f_m; a_n)$ [9]:

$$\delta_{R,m} = \frac{\mu_{R,m}}{R_{\text{NLNA}}(f_m; a_n)} \quad (1.6)$$

- $\delta_{R,g}$ can be set equal to 1 for most cases, excluding the cases involving strongly slender systems ($a/d \gg 1$).

In equation 1.4, the term V_R represents the coefficient of variation of the global structural resistance, accounting for uncertainties in both materials and geometrical properties [9]. The value is evaluated as follows:

$$V_R = \sqrt{V_{R,m}^2 + V_{R,g}^2} \quad (1.7)$$

Where:

- $V_{R,m}$ represents the portion of V_R related to the aleatory uncertainty of material properties.
- $V_{R,g}$ accounts for the percentage of V_R linked to the aleatory uncertainty of the geometric properties.

Starting from this point, the choice of a different safety format leads to a different value of V_R . According to Diego et al.[19], the $V_{R,g}$ value can be set equal to 0.05 for non-slender RC elements. Instead, $V_{R,m}$ has to be defined according to the specific safety format selected from those proposed within the GRMs or statistically derived through the PM. Below, the different safety formats are reported and analyzed:

- i. **Partial Factor Method (PFM) [5]:** enables safety verification by performing just one NLNA. It uses as representative values the design ones for both materials and geometrical properties, f_d and a_d , respectively. The design values f_d should be derived according to the Fib Model Code 2010 (Fib Model Code), depriving them of the model uncertainty contribution. This method applies the equation 1.3 and sets γ_R as a unit and γ_{Rd} as an appropriate value.
- ii. **Standard Estimation of Coefficient of Variation Method (ECoV) [5] [26]:** adopts the mean values of material properties, f_m , and the nominal values of geometrical ones, a_n , as representative. The value γ_R can be evaluated using the equations provided earlier in this subsection, while γ_{Rd} has to be assessed separately. Regarding $V_{R,m}$, 2 NLNAs need to be run: in the first, the mean values of material properties, f_m , and nominal values of geometrical properties, a_n , are used as representative values; in the second one, the characteristic and nominal values, f_k and a_n , are implemented.
- iii. **Global Safety Format (GSF) [8]:** In the initial phase, it uses the same approach as the ECoV method. The main difference lies in the evaluation of $V_{R,m}$. The GSF method assesses the coefficient of variation of the global structural resistance as the ratio between the standard deviation, σ_R , and the mean value, μ_R , considering the hypothesis of log-normal distribution as always valid. The two statistical parameters are estimated through several NLFEAs, run using the Latin Hypercube Sampling method, which accounts for the aleatory uncertainties related to material properties. Although the approach may recall the one used in the PM, the GSF method is based on mean values of material properties and involves performing a first-order approximation of the Taylor expansion function of the ultimate global resistance. On the other hand, the PM directly refers to a quantile of the appropriate probabilistic distribution. This is the procedure adopted in [5].
- iv. **Global Resistance Factor (GRF) [8]:** employs the global safety factor γ_{GL} set equal to 1.27, assuming a unitary value for γ_{Rd} . To estimate the representative

value of the global resistance, it uses the mean value of the reinforcement, f_{ym} , and the reduced compressive strength for concrete, f_{cmd} . The partial factors are equalized, and beyond this step, the method becomes essentially like the PFM.

- v. **Stain-Based Method (SBM) [26]:** is a recent methodology that aims to estimate the coefficient of variation $V_{R,m}$ that accounts for aleatory uncertainty associated with material properties within the GRM. This approach has been developed by Gino et al. [26] and starting from a benchmark that encompasses brittle and ductile failure modes, it offers an exhaustive probability analysis to accurately estimate R_d . If the initial sample is made of n RC structural elements, through this process the same number of NLFE models is implemented, each with different modeling assumptions that reduce the epistemic uncertainty. After that, a probabilistic analysis is carried out on the models, differentiating between relevant and basic assumptions. These latter regard statistical parameters of material properties such as concrete quality. Indeed, the coefficient of variation of the concrete cylinder compressive strength, V_c , usually is assumed to be equal to 0.15, considering all the uncertainties that involve the casting phase, and the construction procedure followed by the company. On the other hand, it does not consider factors like aging and degradation phenomena that may be present in existing structures. For this reason, the strain-based method assumes 3 different CV values: 0.15, 0.20, and 0.25. Therefore, the probabilistic analysis adopts for each of the 3 cases the Latin Hypercube Sampling (LHS) for each of the n specimens. The 30 samples generated from each different case describe the probability distribution of the global structural resistance through its key statistical parameters (i.e., $\mu_{R,m}$, $V_{R,m}$). These values are intrinsically related to the peak strain $\varepsilon_{s,max}$ observed in the primary reinforcement during the failure mechanism. Investigating 2 types of failure modes, the primary reinforcement involved within the global resistance mechanism changes as follows:

- In the bending failure, the primary tensile reinforcement can be considered the longitudinal bars placed in the bottom part of the cross-section.
- In the shear failure, the reinforcement that acts as a primary resistance mechanism is the stirrup.

The analysis in this safety format is performed using the mean values f_m for material properties and nominal values a_n for geometrical ones. The positive advantage of this method is that, at the end of the procedure, $V_{R,m}$ depends solely on $\varepsilon_{s,max}$ observed in the NLFEAs.

To understand if the GRMs can be applied to estimate the design's ultimate load instead of the more complicated PM, the analyst can implement 2 preliminary NLFEAs: the first uses the mean values for the concrete properties and the design values for the reinforcement properties, the second simulation vice-versa. If the failure modes from these two analyses are the same, the modeler can use one of the GRMs following the standard procedure, instead, if they are different, an additional safety factor is necessary.

The PM is considered the benchmark safety format, but from a computational point of view, the effort required from the GRMs is significantly lower than the PM. Therefore, to be able to implement them also when the 2 failure modes of the preliminary NLFEAs differ, an additional failure mode-based safety factor, denoted as γ_{FM} , is introduced. This factor has been calibrated to ensure a perfect correspondence between the R_d value assessed through the PM and that from one of the GRMs. For this reason, γ_{FM} can range

between 1.00 and 1.18. Under the hypotheses of $\beta = 3.8$, moderate consequences in the case of failure, a lifetime of 50 years, and $\alpha_R = 0.8$ the γ_{FM} is set equal to 1.15 [8]. This is shown in the image 1.2b that proposes the 2 alternatives to estimate the structural resistance R_d : with and without γ_{FM} [26].

Images 1.2 summarize the strain-based safety format, highlighting the procedure necessary to assess the design value R_d . It can be considered the complementary part of scheme 2 presented in the introduction section.

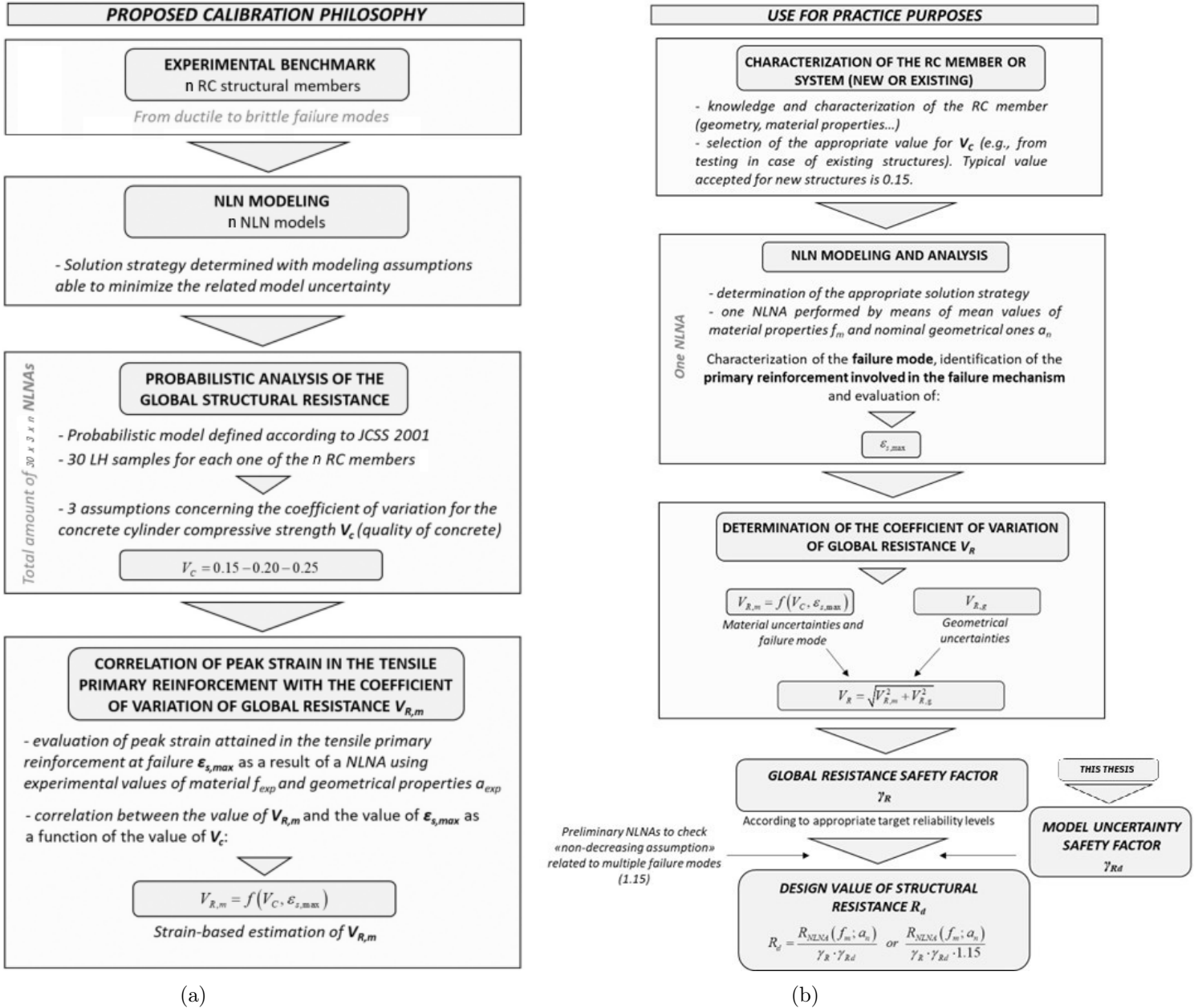


Figure 1.2: (a) Calibration methodology for the strain-based approach to estimate the $V_{R,m}$ and (b) Calibration procedure for the strain-based approach to estimate R_d

Chapter 2

2.1 Experimental benchmark

2.1.1 Selection Criteria

As previously mentioned, the Bayesian approach to work effectively needs as extensive as possible database. For this reason, 35 RC beams have been selected for the analyses. Even if the choice of the papers may seem a trivial phase, it requires an accurate selection of reliable information to ensure the success of the entire process. To guarantee this level of confidence, the main bibliographic databases used include:

- ScienceDirect
- ResearchGate
- Wiley
- Semantic Scholar
- Webthesis Polytechnic University of Turin

The thesis aims to evaluate the model uncertainty safety factor γ_{Rd} for standard RC beams. Therefore alterations, such as fiber reinforcement within the concrete, high-performance concrete, deep beams, and carbon fiber reinforced polymer (CFRP) tied with stirrups, have not been accounted for in the analysis. This decision was made to avoid the introduction of an excessive number of variables into the process with the risk of not being able to capture the fundamental mechanical aspects. When several parameters come into play, it becomes challenging to understand how each factor affects the result, leading to a possible loss of accuracy. On the other hand, within these boundaries, it's essential to analyze RC beams with scattered mechanical and geometrical properties, such as the a/d ratio, stirrup spacing s , reinforcement ratio ρ , and shear reinforcement ratio ρ_{sw} . This approach enables a more comprehensive analysis, ensuring the generality that the thesis is looking for, without the risk of finding conclusions only valid under restrictive assumptions.

Another important aspect is the completeness of the information: some papers, even if reliable and accurate in the experimental procedure, omit some values, such as the effective depth. Although these parameters can also be estimated through correlation or drawings of the beam scheme in AutoCAD, such estimates may introduce unknown uncertainties.

In some cases, experiments want to focus on specific failure mechanisms, like the shear one. To analyze this failure mode, it's essential to avoid the flexural one. To do this, the beams are heavily reinforced in the bottom part of the section, ensuring enough longitudinal reinforcement that the stirrups reach the yield point earlier and shear failure occurs. Eurocode 2 establishes a range within which the longitudinal tension reinforcement must fall [42]:

$$A_{s,\min} \geq 0.0013 \cdot b_t \cdot d \quad (\text{a})$$

$$A_{s,\max} \leq 0.04 \cdot A_c \quad (\text{b})$$

Where:

- b_t denotes the mean width of the tension zone.
- d is the effective depth.
- A_c refers to the gross cross-sectional area of concrete.

These are the extreme recommended parameters, but their values may vary according to each country's National Annex.

The selected beams align with these criteria and will be presented in the following subsections.

2.1.2 Test typologies

All the beams analyzed in this work have been tested with one of the following types of tests:

- 3-point bending test
- 4-point bending test

These tests are commonly used to evaluate the stiffness of materials. In both cases, the beams are simply supported, but the different setups in the load application induce within RC different stress distributions, as follows:

- The 3-point bending test, the beam is subjected to a triangular distribution of bending moment and the peak occurs under the applied load. Instead, the shear stress value is constant throughout the entire beam, changing the sign in the middle point. The central area has the highest bending moment and shear stress; therefore, it is the location where the failure likely may occur
- The 4-point bending test creates a constant bending moment and zero shear force between the 2 loading points, leading to a symmetrical combined bending and shear stress in the RC within the area between the support and the loading point. This latter region is where potentially the failure may occur

Both tests can be conducted using either load control or displacement control methods, depending on the objective of the investigation. This thesis aims to investigate the beam behavior, with a focus on the region between the yield point and the peak load, which can be investigated using both approaches. Regarding the load control method, the universal

testing machine (UTM) applies a load to the specimen, increasing it at a controlled rate. The strain gauges or linear variable differential transformers (LVDT) are placed along the beam to measure the resulting displacement. This method is optimal when the main interest of the analysis is the material's response to an increasing load. With a decreasing post-peak branch, the machine stops the loading phase when it reaches the maximum load that the RC beam can bear. On the other hand, the displacement control approach uses the UTM to impose an increase in the displacement at a controlled rate, while the load cells measure the force needed to do this. It's useful to conduct the test in this way when the material analyzed has a ductile behavior and large deformations occur after yielding. In an NLNA a good understanding of what happens in the post-yield branch and analyzing a complete load-displacement curve is crucial. This enables the assessment of the material's ductility and toughness: mechanical properties that reflect the ability of a material to provide a "buffer" before its failure.

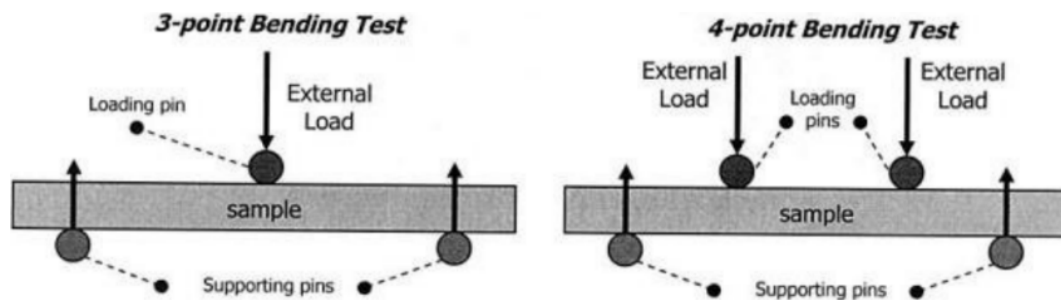


Figure 2.1: Three-point bending test and four-point bending test

2.1.3 Database

In this subsection, all the specimens are described. In line with the thesis' approach of analyzing the beams separately according to the failure mode, the beams have been divided into two groups:

- 15 beams subjected to flexural failure
- 20 beams subjected to shear failure

The following pages report only the information implemented in the NLFE models, such as geometry and mechanical properties. To get a more detailed view of the experimental procedure, the types of beams analyzed, and the comments on the experiment results of each specimen, please refer to the paper from which this information has been sourced. Even if the load-deformation curve it's important to have a comprehensive analysis of the beam, showing how it behaves during the loading phase, it will be presented later in Chapter 4 with the results of the NLNAs. This enables an easier comparison between the 6 modeling hypotheses and the experimental curve.

The last constraint to consider, which also depends on country by country, is the α angle of the stirrups. In the context of Italian legislation, the only α angle admitted is 90° . Italy is situated in a seismically active zone where the risk of an earthquake is significant, especially in some regions. If the stirrups had a different angle, they could potentially align with the direction of crack formation during seismic activity and be completely useless. For this reason, even if an α angle of 90° may not be the most efficient choice under normal conditions, it allows the stirrups to work effectively during an earthquake, preventing or at least delaying the failure of the structure.

Specimens experiencing flexural failure

Giuseppe Campione [4]

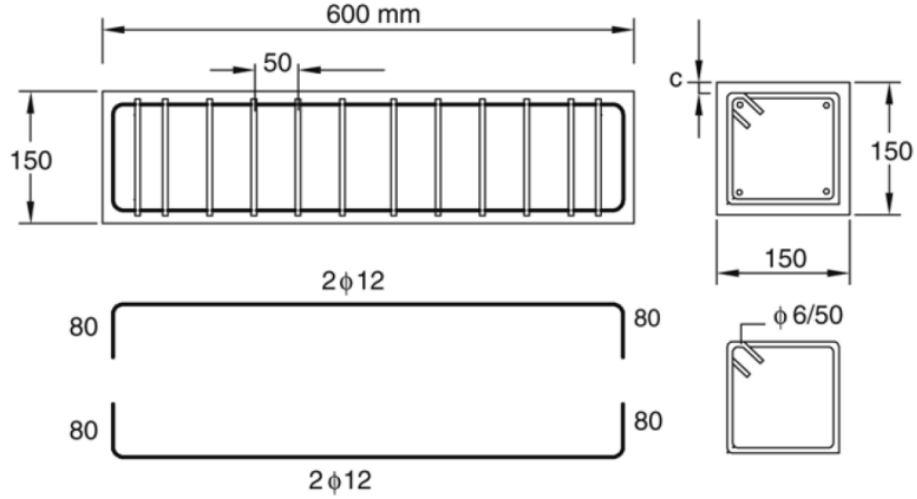


Figure 2.2: 5.0.1 geometry and rebar schedule

Specimen	A's [mm ²]	A _s [mm ²]	d [mm]	ρ [%]
5.0.1	2Φ12	2Φ12	133	1.13

Table 2.1: 5.0.1 longitudinal reinforcement

Specimen	A _{sw} [mm ²]	s [mm]	ρ _{sw} [%]
5.0.1	Φ6	50	0.76

Table 2.2: 5.0.1 shear reinforcement

Specimen	Compressive strength f_c [N/mm ²]	Yielding strength f_y [N/mm ²]	Ultimate strength f_u [N/mm ²]
5.0.1	32.50	467	546

Table 2.3: 5.0.1 mechanical properties

Specimen	P_y [kN]	δ_y [mm]	P_u [kN]	δ_u [mm]
5.0.1	115	3	133	1

Table 2.4: 5.0.1 ultimate load, yield point, and corresponding deformations

Qian Chunxiang [12]

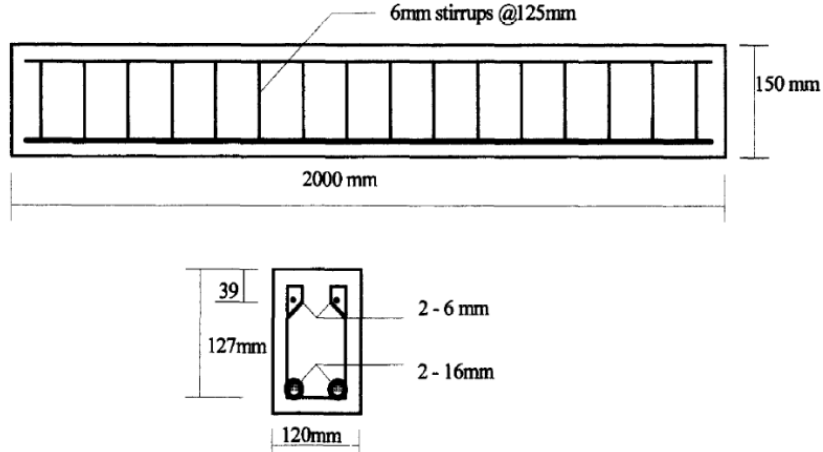


Figure 2.3: CF/CS/CT geometry and rebar schedule

Specimen	A's [mm ²]	As [mm ²]	d [mm]	ρ [%]
CF/CS/CT	2 Φ 6	2 Φ 16	127	2.64

Table 2.5: CF/CS/CT longitudinal reinforcement

Specimen	Asw [mm ²]	s [mm]	ρ_{sw} [%]
CF/CS/CT	Φ 6	125	0.38

Table 2.6: CF/CS/CT shear reinforcement

Specimen	Compressive strength f_c [N/mm ²]	Yielding strength f_y [N/mm ²]	Ultimate strength f_u [N/mm ²]
CF	58.32	390	448
CS	61.29	390	448
CT	58.14	390	448

Table 2.7: CF/CS/CT mechanical properties

Specimen	P_y [kN]	δ_y [mm]	P_u [kN]	δ_u [mm]
CF	53	15	56	31
CS	51	16	54	28
CT	53	17	54	28

Table 2.8: CF/CS/CT ultimate load, yield point, and corresponding deformations

Hussein M. Elsanadedy [17]

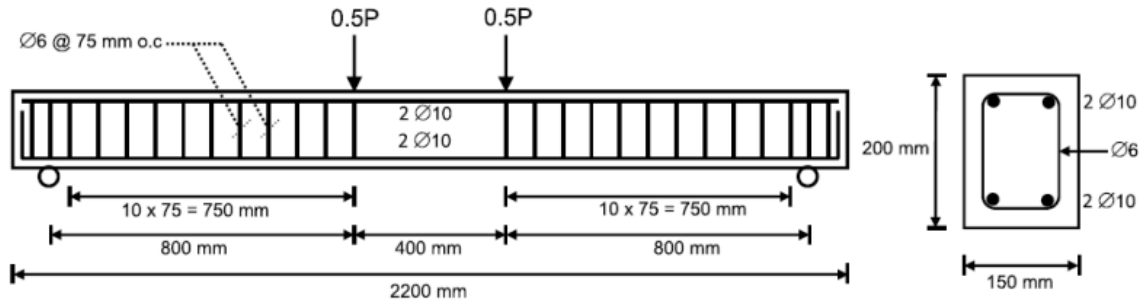


Figure 2.4: BF-1 geometry and rebar schedule

Specimen	$A's$ [mm ²]	A_s [mm ²]	d [mm]	ρ [%]
BF-1	2Ø10	2Ø10	175	0.60

Table 2.9: BF-1 longitudinal reinforcement

Specimen	A_{sw} [mm ²]	s [mm]	ρ_{sw} [%]
BF-1	Ø6	75	0.51

Table 2.10: BF-1 shear reinforcement

Specimen	Compressive strength f_c [N/mm ²]	Yielding strength f_y [N/mm ²]	Ultimate strength f_u [N/mm ²]
BF-1	20.00	578	684

Table 2.11: BF-1 mechanical properties (only longitudinal reinforcement)

Specimen	Yielding strength f_y [N/mm ²]	Ultimate strength f_u [N/mm ²]
BF-1	238	372

Table 2.12: BF-1 stirrup mechanical properties

Specimen	P_y [kN]	δ_y [mm]	P_u [kN]	δ_u [mm]
BF-1	41	12	43	86

Table 2.13: BF-1 ultimate load, yield point, and corresponding deformations

Alberto Meda [40]

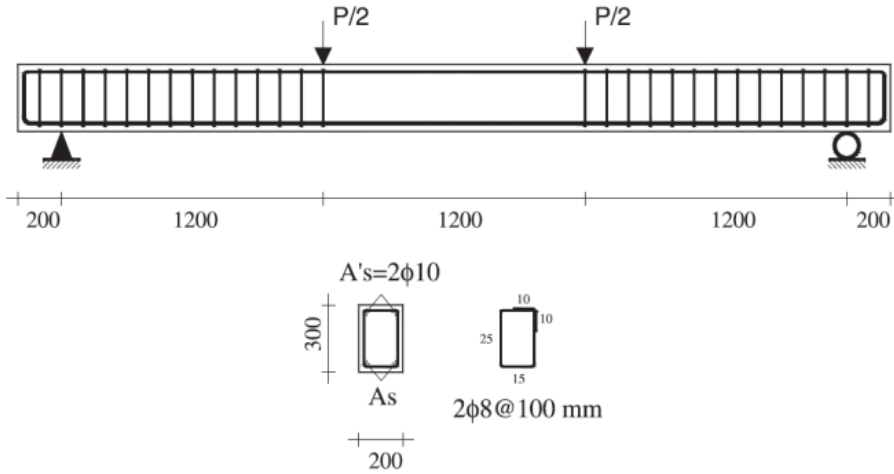


Figure 2.5: BP-C-2/BP-C-4 geometry and rebar schedule

Specimen	A's [mm ²]	As [mm ²]	d [mm]	ρ [%]
BP-C-2	2 Φ 10	2 Φ 16	260	0.77
BP-C-4	2 Φ 10	4 Φ 16	260	1.55

Table 2.14: BP-C-2/BP-C-4 longitudinal reinforcement

Specimen	Asw [mm ²]	s [mm]	ρ_{sw} [%]
BP-C-2	Φ 8	100	0.50
BP-C-4	Φ 8	100	0.50

Table 2.15: BP-C-2/BP-C-4 shear reinforcement

Specimen	Compressive strength f_c [N/mm ²]	Yielding strength f_y [N/mm ²]	Ultimate strength f_u [N/mm ²]
BP-C-2	33.50	534	630
BP-C-4	33.50	534	630

Table 2.16: BP-C-2/BP-C-4 mechanical properties

Specimen	P_y [kN]	δ_y [mm]	P_u [kN]	δ_u [mm]
BP-C-2	81	20	90	110
BP-C-4	160	23	168	67

Table 2.17: BP-C-2/BP-C-4 ultimate load, yield point, and corresponding deformations

Luis Evangelista [20]

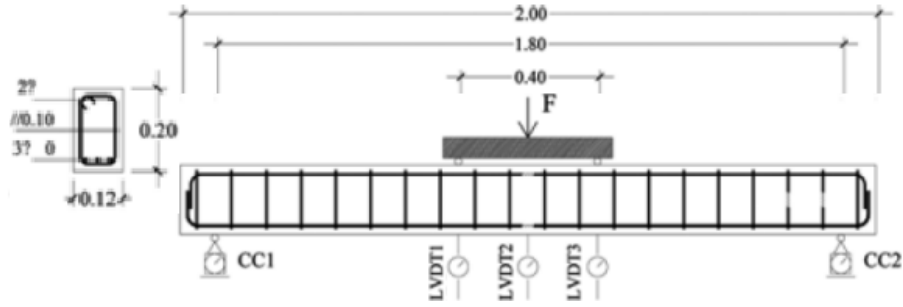


Figure 2.6: RC-1 geometry and rebar schedule

Specimen	$A's$ [mm ²]	A_s [mm ²]	d [mm]	ρ [%]
RC-1	2 Φ 6	3 Φ 10	185	1.06

Table 2.18: RC-1 longitudinal reinforcement

Specimen	A_{sw} [mm ²]	s [mm]	ρ_{sw} [%]
RC-1	Φ 6	100	0.48

Table 2.19: RC-1 shear reinforcement

Specimen	Compressive strength f_c [N/mm ²]	Yielding strength f_y [N/mm ²]	Ultimate strength f_u [N/mm ²]
RC-1	33.56	525	670

Table 2.20: RC-1 mechanical properties (only longitudinal reinforcement)

Specimen	Yielding strength f_y [N/mm ²]	Ultimate strength f_u [N/mm ²]
RC-1	597	746

Table 2.21: RC-1 stirrup mechanical properties

Specimen	P_y [kN]	δ_y [mm]	P_u [kN]	δ_u [mm]
RC-1	70	10	77	20

Table 2.22: RC-1 ultimate load, yield point, and corresponding deformations

M. A. Rashid and M. A. Mansur [45]

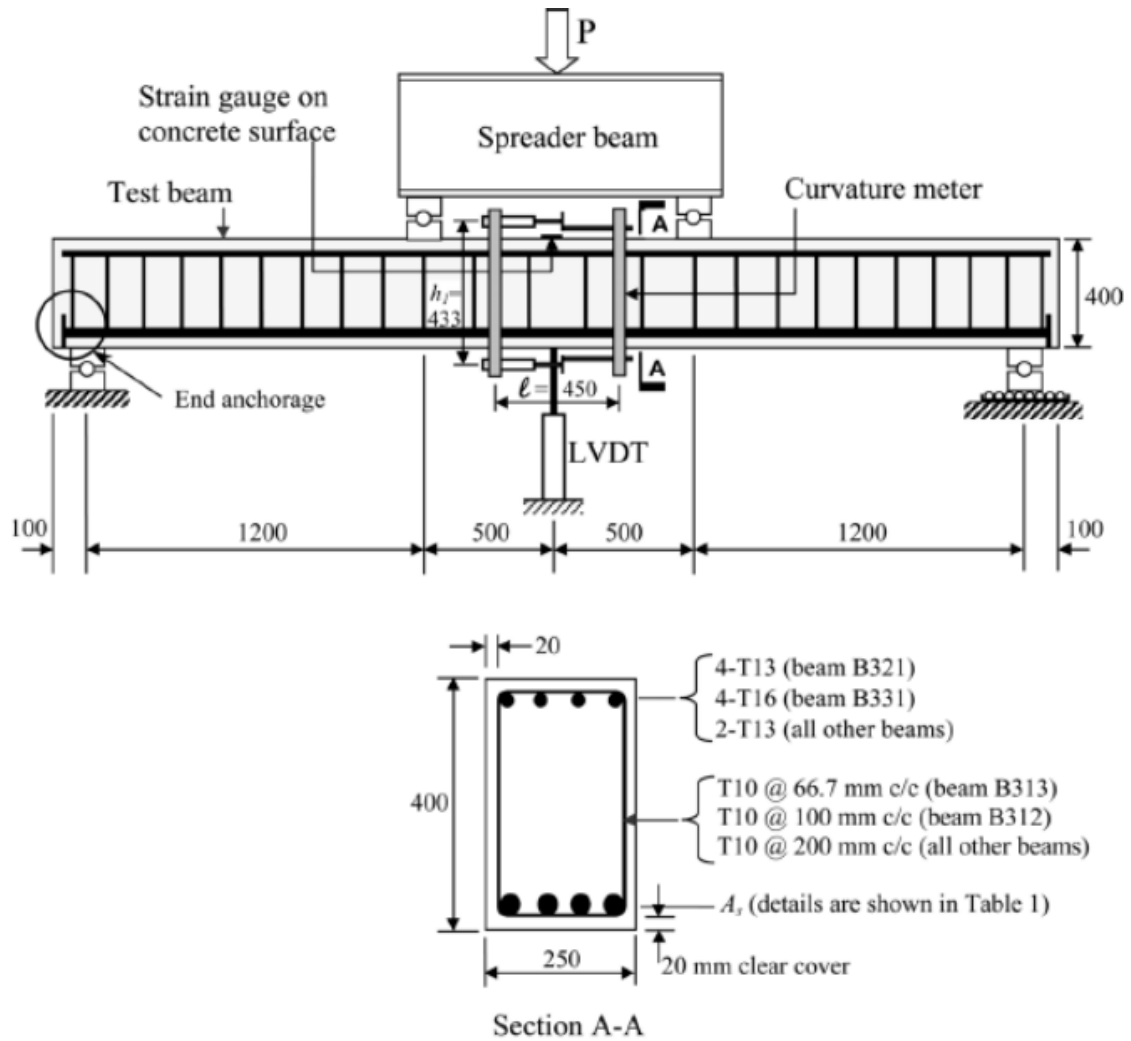


Figure 2.7: A211/B312/B313/B321/C211/C311/C411 geometry and rebar schedule

Specimen	A's [mm ²]	A _s [mm ²]	d [mm]	ρ [%]
A211	2Φ13	4Φ25	380	2.07
B312	2Φ13	6Φ25	380	3.10
B313	2Φ13	6Φ25	380	3.10
B321	4Φ13	6Φ25	380	3.10
C211	2Φ13	4Φ25 + 2Φ16	380	2.49
C311	2Φ13	4Φ25 + 4Φ16	380	2.91
C411	2Φ13	4Φ25 + 2Φ20	380	2.73

Table 2.23: A211/B312/B313/B321/C211/C311/C411 longitudinal reinforcement

Specimen	Asw [mm ²]	s [mm]	ρ_{sw} [%]
A211	Φ10	200	0.31
B312	Φ10	100	0.63
B313	Φ10	67	0.94
B321	Φ10	200	0.31
C211	Φ10	200	0.31
C311	Φ10	200	0.31
C411	Φ10	200	0.31

Table 2.24: A211/B312/B313/B321/C211/C311/C411 shear reinforcement

Specimen	Compressive strength f_c [N/mm ²]	Yielding strength f_y [N/mm ²]	Ultimate strength f_u [N/mm ²]
A211	42.80	460	575
B312	72.80	460	575
B313	72.80	460	575
B321	77.00	460	575
C211	85.60	460	575
C311	88.10	460	575
C411	85.60	460	575

Table 2.25: A211/B312/B313/B321/C211/C311/C411 mechanical properties

Specimen	P_y [kN]	δ_y [mm]	P_u [kN]	δ_u [mm]
A211	439	15	462	37
B312	712	22	732	24
B313	733	22	745	27
B321	732	24	767	34
C211	638	25	650	44
C311	722	22	731	28
C411	889	26	898	29

Table 2.26: A211/B312/B313/B321/C211/C311/C411 ultimate load, yield point, and corresponding deformations

Specimens experiencing shear failure

C.G Karayannis [33]

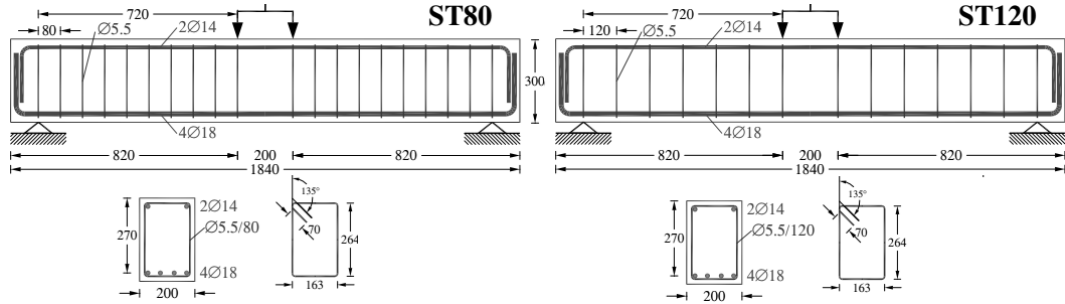


Figure 2.8: ST80/ST120 geometry and rebar schedule

Specimen	A's [mm ²]	As [mm ²]	d [mm]	ρ [%]
ST80/ST120	2Ø14	4Ø18	270	1.88

Table 2.27: ST80/ST120 longitudinal reinforcement

Specimen	Asw [mm ²]	s [mm]	ρ_{sw} [%]
ST80	Ø5.5	80	0.30
ST120	Ø5.5	120	0.20

Table 2.28: ST80/ST120 shear reinforcement

Specimen	Compressive strength f_c [N/mm ²]	Yielding strength f_y [N/mm ²]	Ultimate strength f_u [N/mm ²]
ST80/ST120	28.50	550	690

Table 2.29: ST80/ST120 mechanical properties (only longitudinal reinforcement)

Specimen	Yielding strength f_y [N/mm ²]	Ultimate strength f_u [N/mm ²]
ST80/ST120	310	430

Table 2.30: ST80/ST120 stirrup mechanical properties

Specimen	P_y [kN]	δ_y [mm]	P_u [kN]	δ_u [mm]
ST80	237	6.1	251	7.3
ST120	206	6.9	215	7.6

Table 2.31: ST80/ST120 ultimate load, yield point, and corresponding deformations

Liu Jin [37]

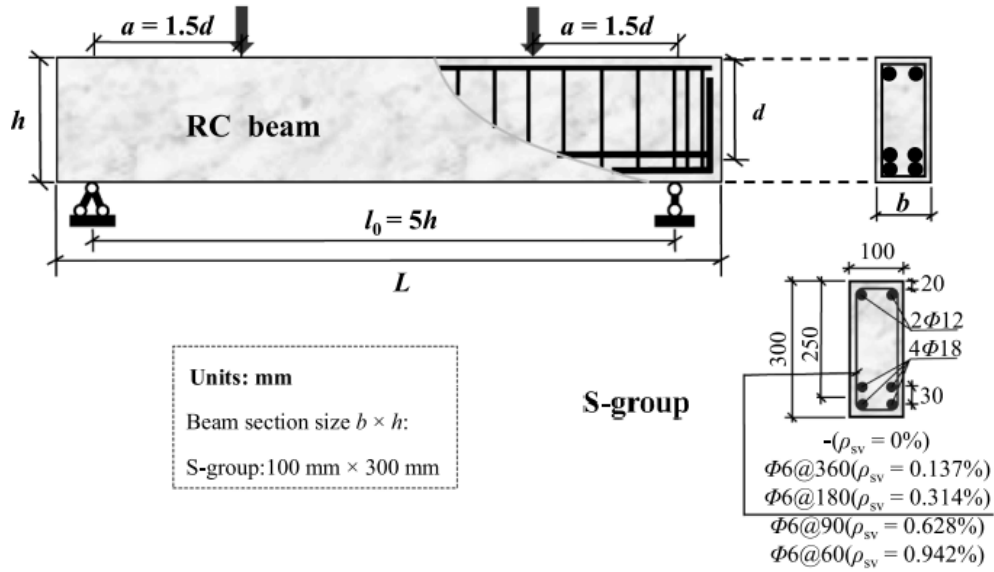


Figure 2.9: S-0.157/S-0.314/S-0.628/S-0.942 geometry and rebar schedule

Specimen	A's [mm ²]	As [mm ²]	d [mm]	ρ [%]
S-0.157/S-0.314/S-0.628/S-0.942	2Φ12	4Φ18	250	4.07

Table 2.32: S-0.157/S-0.314/S-0.628/S-0.942 longitudinal reinforcement

Specimen	Asw [mm ²]	s [mm]	ρ_{sw} [%]
S-0.157	Φ6	360	0.16
S-0.314	Φ6	180	0.32
S-0.628	Φ6	90	0.63
S-0.942	Φ6	60	0.95

Table 2.33: S-0.157/S-0.314/S-0.628/S-0.942 shear reinforcement

Specimen	Compressive strength f_c [N/mm ²]	Yielding strength f_y [N/mm ²]	Ultimate strength f_u [N/mm ²]
S-0.157/S-0.314/S-0.628/S-0.942	33.1	456	593

Table 2.34: S-0.157/S-0.314/S-0.628/S-0.942 mechanical properties of concrete and longitudinal reinforcement in tension

Specimen	Yielding strength f_y [N/mm ²]	Ultimate strength f_u [N/mm ²]
S-0.157/S-0.314/S-0.628/S-0.94	408	584

Table 2.35: S-0.157/S-0.314/S-0.628/S-0.942 mechanical properties of longitudinal reinforcement in compression

Specimen	Yielding strength f_y [N/mm ²]	Ultimate strength f_u [N/mm ²]
S-0.157/S-0.314/S-0.628/S-0.94	406	590

Table 2.36: S-0.157/S-0.314/S-0.628/S-0.942 stirrup mechanical properties

Specimen	P_y [kN]	δ_y [mm]	P_u [kN]	δ_u [mm]
S-0.157	299	4.7	311	4.9
S-0.314	309	5.0	340	5.8
S-0.628	399	6.4	409	6.6
S-0.942	412	6.5	422	6.9

Table 2.37: S-0.157/S-0.314/S-0.628/S-0.942 ultimate load, yield point, and corresponding deformations

Mostefa Hamrat [29]

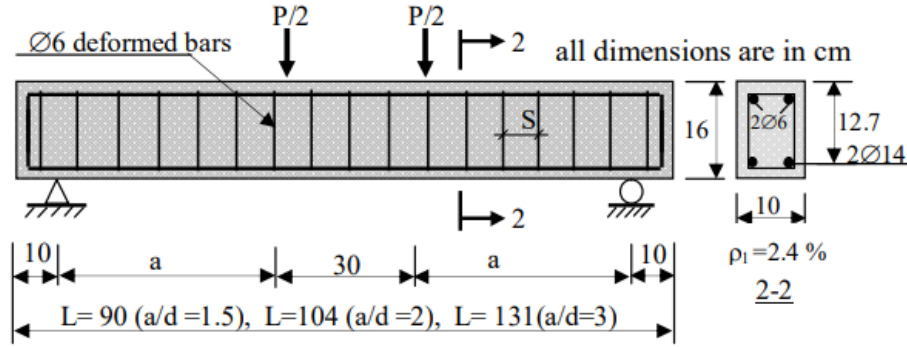


Figure 2.10: B44-1.5W/B44-2W geometry and rebar schedule

Specimen	A's [mm ²]	As [mm ²]	d [mm]	ρ [%]
B44-1.5W/B44-2W	2Φ6	2Φ14	127	243

Table 2.38: B44-1.5W/B44-2W longitudinal reinforcement

Specimen	Asw [mm ²]	s [mm]	ρ _{sw} [%]
B44-1.5W/B44-2W	Φ6	90	0.63

Table 2.39: B44-1.5W/B44-2W shear reinforcement

Specimen	Compressive strength f_c [N/mm ²]	Yielding strength f_y [N/mm ²]	Ultimate strength f_u [N/mm ²]
ST80/ST120	44.20	508	581

Table 2.40: B44-1.5W/B44-2W mechanical properties (only longitudinal reinforcement)

Specimen	Yielding strength f_y [N/mm ²]	Ultimate strength f_u [N/mm ²]
B44-1.5W/B44-2W	512	620

Table 2.41: B44-1.5W/B44-2W stirrup mechanical properties

Specimen	P_y [kN]	δ_y [mm]	P_u [kN]	δ_u [mm]
B44-1.5W	169	3.2	174	3.5
B44-2W	135	4.5	142	5.3

Table 2.42: B44-1.5W/B44-2W ultimate load, yield point, and corresponding deformations

Chadon Lee [34]

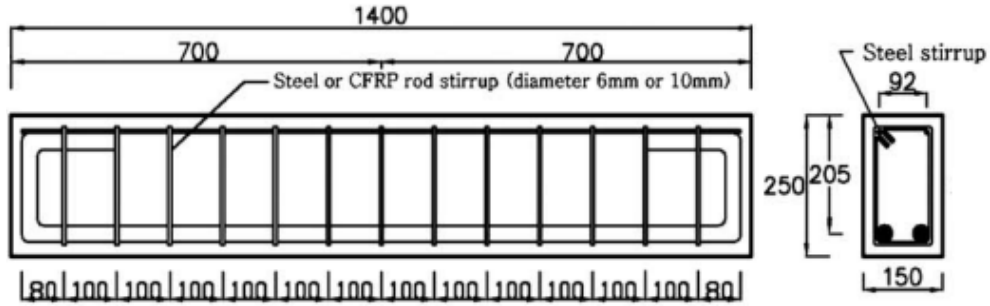


Figure 2.11: S06/S10 geometry and rebar schedule

Specimen	$A's$ [mm ²]	A_s [mm ²]	d [mm]	ρ [%]
S06/S10	2 Φ 6	2 Φ 22	205	2.47

Table 2.43: S06/S10 longitudinal reinforcement

Specimen	A_{sw} [mm ²]	s [mm]	ρ_{sw} [%]
S06	Φ 6	100	0.40
S10	Φ 10	100	0.50

Table 2.44: S06/S10 shear reinforcement

Specimen	Compressive strength f_c [N/mm ²]	Yielding strength f_y [N/mm ²]	Ultimate strength f_u [N/mm ²]
S06/S10	32.50	400	500

Table 2.45: S06/S10 mechanical properties

Specimen	P_y [kN]	δ_y [mm]	P_u [kN]	δ_u [mm]
S06	233	4.7	242	5.5
S10	284	5.0	301	6.6

Table 2.46: S06/S10 ultimate load, yield point, and corresponding deformations

Rui Guo [28]

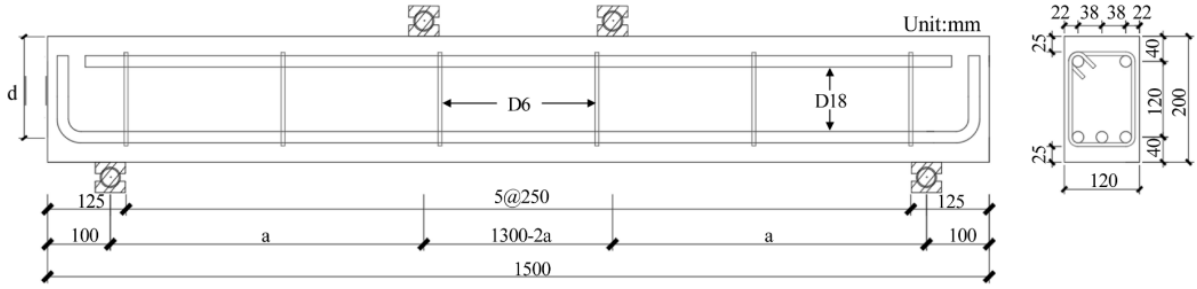


Figure 2.12: FOS0 geometry and rebar schedule

Specimen	$A's$ [mm ²]	A_s [mm ²]	d [mm]	ρ [%]
FOS0	2 Φ 18	3 Φ 18	160	3.18

Table 2.47: FOS0 longitudinal reinforcement

Specimen	A_{sw} [mm ²]	s [mm]	ρ_{sw} [%]
FOS0	Φ 6	250	0.19

Table 2.48: FOS0 shear reinforcement

Specimen	Compressive strength f_c [N/mm ²]	Yielding strength f_y [N/mm ²]	Ultimate strength f_u [N/mm ²]
FOS0	31.60	400	540

Table 2.49: FOS0 mechanical properties

Specimen	P_y [kN]	δ_y [mm]	P_u [kN]	δ_u [mm]
FOS0	99	2.0	115	5.0

Table 2.50: FOS0 ultimate load, yield point, and corresponding deformations

Calogero Cucchiara [14]

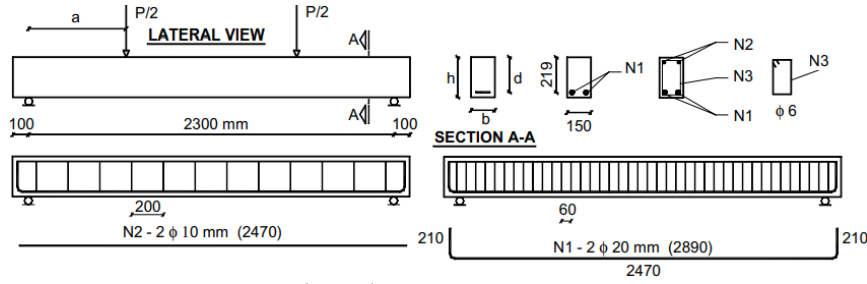


Figure 2.13: A01/A02/B02 geometry and rebar schedule

Specimen	$A's$ [mm ²]	A_s [mm ²]	d [mm]	ρ [%]
A01/A02/B02	2 Φ 10	2 Φ 20	219	1.67

Table 2.51: A01/A02/B02 longitudinal reinforcement

Specimen	A_{sw} [mm ²]	s [mm]	ρ_{sw} [%]
A01	Φ 6	200	0.19
A02/B02	Φ 6	60	0.63

Table 2.52: A01/A02/B02 shear reinforcement

Specimen	Compressive strength f_c [N/mm ²]	Yielding strength f_y [N/mm ²]	Ultimate strength f_u [N/mm ²]
A01/A02/B02	41.2	610	671

Table 2.53: A01/A02/B02 mechanical properties (only longitudinal reinforcement)

Specimen	Yielding strength f_y [N/mm ²]	Ultimate strength f_u [N/mm ²]
A01/A02/B02	510	561

Table 2.54: A01/A02/B02 stirrup mechanical properties

Specimen	P_y [kN]	δ_y [mm]	P_u [kN]	δ_u [mm]
A01	164	11.6	178	13.9
A02	199	14.1	228	19.2
B02	272	13.5	284	15.0

Table 2.55: A01/A02/B02 ultimate load, yield point, and corresponding deformations

Cha-Don Lee [36]

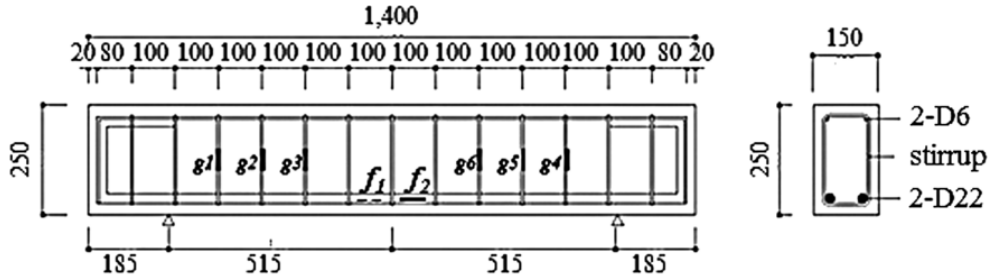


Figure 2.14: B1S06/B1S10/B2S06 geometry and rebar schedule

Specimen	A's [mm ²]	As [mm ²]	d [mm]	ρ [%]
B1S06/B1S10/B2S06	2 Φ 6	2 Φ 22	206	2.46

Table 2.56: B1S06/B1S10/B2S06 longitudinal reinforcement

Specimen	Asw [mm ²]	s [mm]	ρ_{sw} [%]
B1S06/B2S06	Φ 6	100	0.43
B1S10	Φ 10	100	0.95

Table 2.57: B1S06/B1S10/B2S06 shear reinforcement

Specimen	Compressive strength f_c [N/mm ²]	Yielding strength f_y [N/mm ²]	Ultimate strength f_u [N/mm ²]
B1S06/B1S10	24.0	420	500
B2S06	30.0	420	500

Table 2.58: B1S06/B1S10/B2S06 mechanical properties

Specimen	P_y [kN]	δ_y [mm]	P_u [kN]	δ_u [mm]
B1S06	192	3.7	203	4.6
B1S10	229	5.1	247	7.1
B2S06	225	6.3	223	7.0

Table 2.59: B1S06/B1S10/B2S06 ultimate load, yield point, and corresponding deformations

Muhammad Tahir [49]

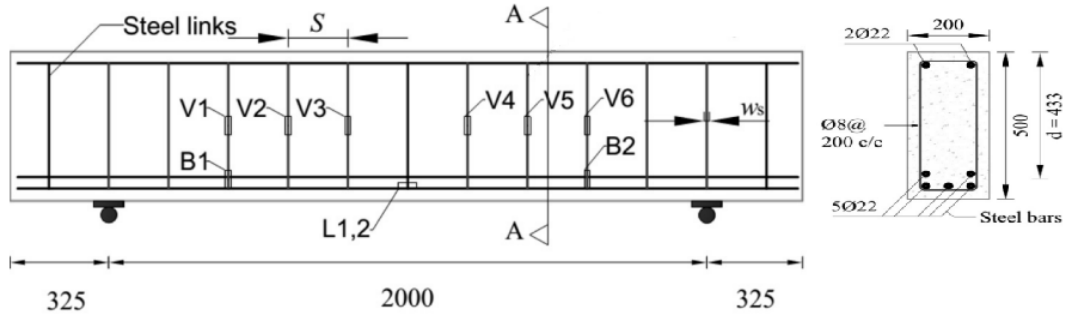


Figure 2.15: S8-90 geometry and rebar schedule

Specimen	$A's$ [mm ²]	A_s [mm ²]	d [mm]	ρ [%]
S8-90	2Φ22	5Φ22	433	2.19

Table 2.60: S8-90 longitudinal reinforcement

Specimen	A_{sw} [mm ²]	s [mm]	ρ_{sw} [%]
S8-90	Φ8	200	0.25

Table 2.61: S8-90 shear reinforcement

Specimen	Compressive strength f_c [N/mm ²]	Yielding strength f_y [N/mm ²]	Ultimate strength f_u [N/mm ²]
S8-90	40.0	460	570

Table 2.62: S8-90 mechanical properties (only longitudinal reinforcement)

Specimen	Yielding strength f_y [N/mm ²]	Ultimate strength f_u [N/mm ²]
S8-90	380	470

Table 2.63: S8-90 stirrup mechanical properties

Specimen	P_y [kN]	δ_y [mm]	P_u [kN]	δ_u [mm]
S8-90	438	5.8	470	6.41

Table 2.64: S8-90 ultimate load, yield point, and corresponding deformations

Hui Ma [38]

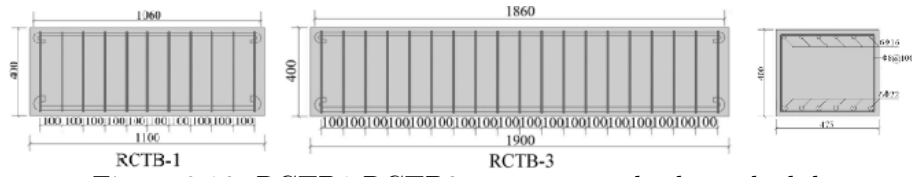


Figure 2.16: RCTB1-RCTB3 geometry and rebar schedule

Specimen	A's [mm ²]	As [mm ²]	d [mm]	ρ [%]
RCTB1-RCTB3	6Φ16	6Φ22	380	1.26

Table 2.65: RCTB1-RCTB3 longitudinal reinforcement

Specimen	Asw [mm ²]	s [mm]	ρ_{sw} [%]
RCTB1-RCTB3	Φ8	100	0.21

Table 2.66: RCTB1-RCTB3 shear reinforcement

Specimen	Compressive strength f_c [N/mm ²]	Yielding strength f_y [N/mm ²]	Ultimate strength f_u [N/mm ²]
RCTB1-RCTB3	46.8	458	648

Table 2.67: RCTB1-RCTB3 mechanical properties of concrete and longitudinal reinforcement in tension

Specimen	Yielding strength f_y [N/mm ²]	Ultimate strength f_u [N/mm ²]
RCTB1-RCTB3	464	662

Table 2.68: RCTB1-RCTB3 mechanical properties of longitudinal reinforcement in compression

Specimen	Yielding strength f_y [N/mm ²]	Ultimate strength f_u [N/mm ²]
RCTB1-RCTB3	347	517

Table 2.69: RCTB1-RCTB3 stirrup mechanical properties

Specimen	P_y [kN]	δ_y [mm]	P_u [kN]	δ_u [mm]
RCTB1	1857	5.0	2179	7.3
RCTB3	1015	6.3	1140	9.5

Table 2.70: RCTB1-RCTB3 ultimate load, yield point, and corresponding deformations

Chapter 3

3.1 ATENA and DIANA: Modeling Assumptions and General Framework

This thesis used two software programs to perform 2D plane stress NLFEMs on RC beams: Atena and Diana. All 35 beams were modeled using both programs to reproduce the experimental outcomes described in the previous section and to compare these computational results with the experimental ones. The following section presents and explains the assumptions taken in the modeling phase: the analyst must be fully aware of them and confident with the methodology investigated. For well-done work, it's essential to approach this problem with consistency in the method of all the RC beams. However, it's equally important to acknowledge that different software tools can require different precautions to minimize epistemic uncertainties, thus obtaining reliable and accurate outcomes. The modeling assumptions involve two main spheres:

- Material characterization
- Geometry definition

3.1.1 Material hypothesis

It implies the identification of the most appropriate equilibrium, kinematic, and constitutive laws. Each software integrates several parameters into its framework, which allows it to model different mechanical behaviors of a material with precision. In Atena and Diana, the numerical simulations employ four-node quadrilateral iso-parametric plane stress finite elements, `CCIsoQuad` and `Q8MEM`, obtained through a linear polynomial interpolation within a 2×2 Gauss point's integration scheme. The FE meshes have been carefully defined after a mesh-sensitivity analysis to avoid misleading results. While a finer mesh may appear more accurate and effectively capture the failure mechanism and crack propagation, if its outcomes can't be considered reliable if its dimension is smaller than the concrete's aggregates because the mechanical behavior of a single aggregate is completely different from the overall response of the beam. On the other hand, a coarser mesh enables the replication of the actual concrete behavior but, especially near the supports, it may lead to inaccurate predictions of the beam's response [23] and [16]. The non-linear system of equations is solved using the standard Newton-Raphson iterative method, which operates under the hypothesis of linear approximation. The loading

procedure is divided into a finite number of load stepping to the experimental procedure, minimizing the differences between the numerical simulation and the real procedure. The integration method moves on to the next step once it reaches a displacement error tolerance of 1% or after completing 500 iterations, whichever comes first [23].

Concerning the constitutive models used to reproduce the non-linear material behavior, the main characteristics are the following:

- For concrete, a linear-elastic model using the software material type `Sbeta Material` has been defined. The constitutive law, known as LCS, describes a non-linear behavior in compression until the peak, followed by a linear decreasing branch [16]. The linear compression softening law (LCS) implies that the resistance at the ϵ_u is reduced to half of the peak resistance. Each software package allows the analyst to account for the reduction in concrete's resistance due to cracking by fixing a minimum value as a percentage of the peak resistance. According to [16], this parameter ranges between 0.45 and 0.8 in Atena; instead, Diana adopts Vecchio and Collins' model [16], a diffusive crack model that attributes the reduction of resistance to lateral crack formation. The constitutive law for the tension concrete behavior is bilinear, with three possible different branches after the peak, corresponding to the three hypotheses outlined in the thesis:
 - Elastic-brittle
 - Elastic with post-peak linear tension softening (LTS)
 - Elastic with a perfectly plastic response

These hypotheses have been adopted to cover the possible choices made by an analyst in the modeling phase to account for the influence of the “tension stiffening effect” in structural mechanisms during numerical simulations. A comprehensive explanation of the implications of each assumption in the outcomes will be provided in Chapter 5; here, the focus is on explaining how the software can implement these hypotheses effectively. Atena controls the different tension-softening behaviors with the parameter `C3`, which represents the ultimate strain under tension; in contrast, Diana has built-in options for various concrete behaviors, so it's only necessary to change the setting to simulate the desired model. Regarding the concrete shear behavior, a fixed shear retention factor was selected with a value equal to 0.2 in Diana; in contrast in Atena, where a rotated crack model has been adopted, there was no need for defining a fixed shear retention factor. The first crack model allows the modeler to analyze in the post-processing phase the progressive development and rotation of the cracks because of the applied load. Instead, in the fixed crack model, once a crack forms in the beam, its orientation remains fixed throughout the entire load stage. Therefore, the material behavior is controlled by the crack orientation and the principal stress directions maintain a constant direction.

- For reinforcement rebars, a bilinear $\sigma - \epsilon$ curve with a hardening effect is used, assuming a perfect bond between the reinforcement and the surrounding concrete. To proceed with a standardized procedure, in cases where the papers don't provide the σ_u , it has been assumed to be equal to $1.15 \sigma_y$. Although the software offers options to model the reinforcement bars in a smeared or discrete manner, the latter has been adopted to minimize the discrepancy between the analytical model and the actual RC beam. In all cases, the ϵ_u was set to 9%. As a rule of thumb, when

certain information is missing, such as the yield strain, and the concrete's Young's modulus, these values are assessed starting from the available experimental data, such as the concrete compressive strength, by implementing the formula provided by EN1991-1-1 [41].

- For steel plates, the constitutive law is linear, with a Young's Modulus much higher than that used for the rebars (i.e., 200 GPa). This ensures that the force applied to the upper face of the plates is uniformly distributed across the contact surface with the beam, and the high value of stiffness prevents excessive deformation and failure of the plates during the loading steps.

3.1.2 Geometry characterization

The geometry of each RC beam aligns perfectly with the details provided in the literature: in most cases, the images attached in the papers have been reproduced to scale in AutoCAD to verify the correctness of the reported measurements. The greatest uncertainty is given by the steel plates used for support and load application, as none of the papers contains precise information about their dimensions and shape. Especially in the case of shear failure, where the steel plates are often placed close to the beam section subjected to the highest stress and where the failure mechanism is triggered, therefore they must be modeled with accuracy.

The rebars are modeled as lines, whose coordinates correspond to the central axis of the actual rebars. Being a 2D plane, each stirrup is represented as a double element that encircles the longitudinal reinforcement.

One of the last steps in the pre-processing phase involves the definition of the various types of load cases. For this work, only 3 of them come into play: external forces, supports, and body forces. The first 2 cases have already been discussed; instead, it's important to highlight the third one. In the experimental procedure, the UTM is calibrated after the beam is placed, meaning that the self-weight of the beam is already accounted for in the experiment. In contrast, the software doesn't automatically recognize the self-weight of the beam. Therefore, before running the analysis, the first load step has to be set as only self-weight. During the post-processing phase, the deformations provided by the software have to be adjusted to exclude those induced by the self-weight, to be coherent with the experimental outcomes. Regarding the constraints, a statically determinate scheme has been implemented with a roller and a hinge, placed directly in the middle point of the steel supports. Even if technically just 2 rollers would have been enough to create an isostatic scheme from an equilibrium point of view because the axial force doesn't come into play and there is the orthogonality of constraints.

The next subsection contains tables 3.1 and 3.2, which summarize the main modeling assumptions made in Atena and Diana. These tables help analysts to compare the two software's approaches, highlighting the differences and similarities. It's essential to acknowledge the 2 different approaches in the NLFEA to properly interpret the results and the discrepancy between the experimental and the analytical outcomes presented in the following chapters.

From this chapter onwards, the 2 software will not be mentioned anymore with their name to avoid any type of advertising. The names will be replaced by software A and software B to maintain objectivity, avoiding any positive or negative involuntary promotion. This decision aligns perfectly with the master thesis's objective, which focuses on the technical aspects rather than commercial considerations.

3.1.3 Overview of the Proposed Hypotheses

	Software: ATENA 2D 5.9.0
<i>Equilibrium</i>	<ul style="list-style-type: none"> • Standard Newton-Raphson based on the hypothesis of linear approximation • Convergence criteria based on displacements (with tolerance set equal to 1%); • Load step sizes defined in compliance with the experimental procedure
<i>Compatibility</i>	<p><i>FINITE ELEMENTS</i></p> <ul style="list-style-type: none"> • CCIsoQuad iso-parametric plane stress 4 nodes (2x2 Gauss points integration scheme with linear interpolation) • Discrete reinforcements • Element size defined through an iterative process of numerical accuracy (2.5-7.5 cm)
<i>Constitutive laws</i>	<p><i>CONCRETE</i></p> <ul style="list-style-type: none"> • Rotated crack model, smeared cracking • Mono-dimensional model extended to the biaxial stress state • Compression: non-linear with post-peak linear softening branch • Tensile response of concrete reproduced through 3 different hypotheses: <ul style="list-style-type: none"> – Brittle ($C_3 \approx \varepsilon_{ct}$) – LTS ($C_3 = [2 - 14] \cdot \varepsilon_{ct}$) – Plastic ($C_3 \gg \varepsilon_{ct}$) <p><i>REINFORCEMENT STEEL</i></p> <ul style="list-style-type: none"> • Bi-linear constitutive law for the reinforcement in tension and compression <p><i>STEEL PLATE</i></p> <ul style="list-style-type: none"> • Linear constitutive law in tension and compression, with $E \approx 2 \times 10^6$

Table 3.1: Modeling hypotheses for the non-linear simulations of the 35 RC columns in Atena

	Software: DIANA 10.8
<i>Equilibrium</i>	<ul style="list-style-type: none"> • Standard Newton-Raphson based on the hypothesis of linear approximation • Convergence criteria based on displacements (with tolerance set ranging between 1% and 2%); • Load step sizes defined in compliance with the experimental procedure
<i>Compatibility</i>	<p><i>FINITE ELEMENTS</i></p> <ul style="list-style-type: none"> • Q8MEM iso-parametric plane stress 4 nodes (2x2 Gauss points integration scheme with linear interpolation) • Discrete reinforcements • Element size defined through an iterative process of numerical accuracy (2.5-9.5 cm)
<i>Constitutive laws</i>	<p><i>CONCRETE</i></p> <ul style="list-style-type: none"> • Fixed crack model, smeared cracking, constant shear retention factor = 0.2 • Mono-dimensional model extended to the biaxial stress state • Compression: non-linear with post-peak linear softening branch • Tensile response of concrete reproduced through three different hypotheses: <ul style="list-style-type: none"> – Brittle ($\varepsilon_{ctu} \approx \varepsilon_{ct}$) – LTS ($\varepsilon_{ctu} = [2 - 14] \cdot \varepsilon_{ct}$) – Plastic ($\varepsilon_{ctu} \gg \varepsilon_{ct}$) <p><i>REINFORCEMENT STEEL</i></p> <ul style="list-style-type: none"> • Bi-linear constitutive law for the reinforcement in tension and compression <p><i>STEEL PLATE</i></p> <ul style="list-style-type: none"> • Linear constitutive law in tension and compression, with $E \approx 2 \times 10^6$

Table 3.2: Modeling hypotheses for the non-linear simulations of the 35 RC columns in Diana

3.1.4 General framework for modeling a beam in Atena and Diana

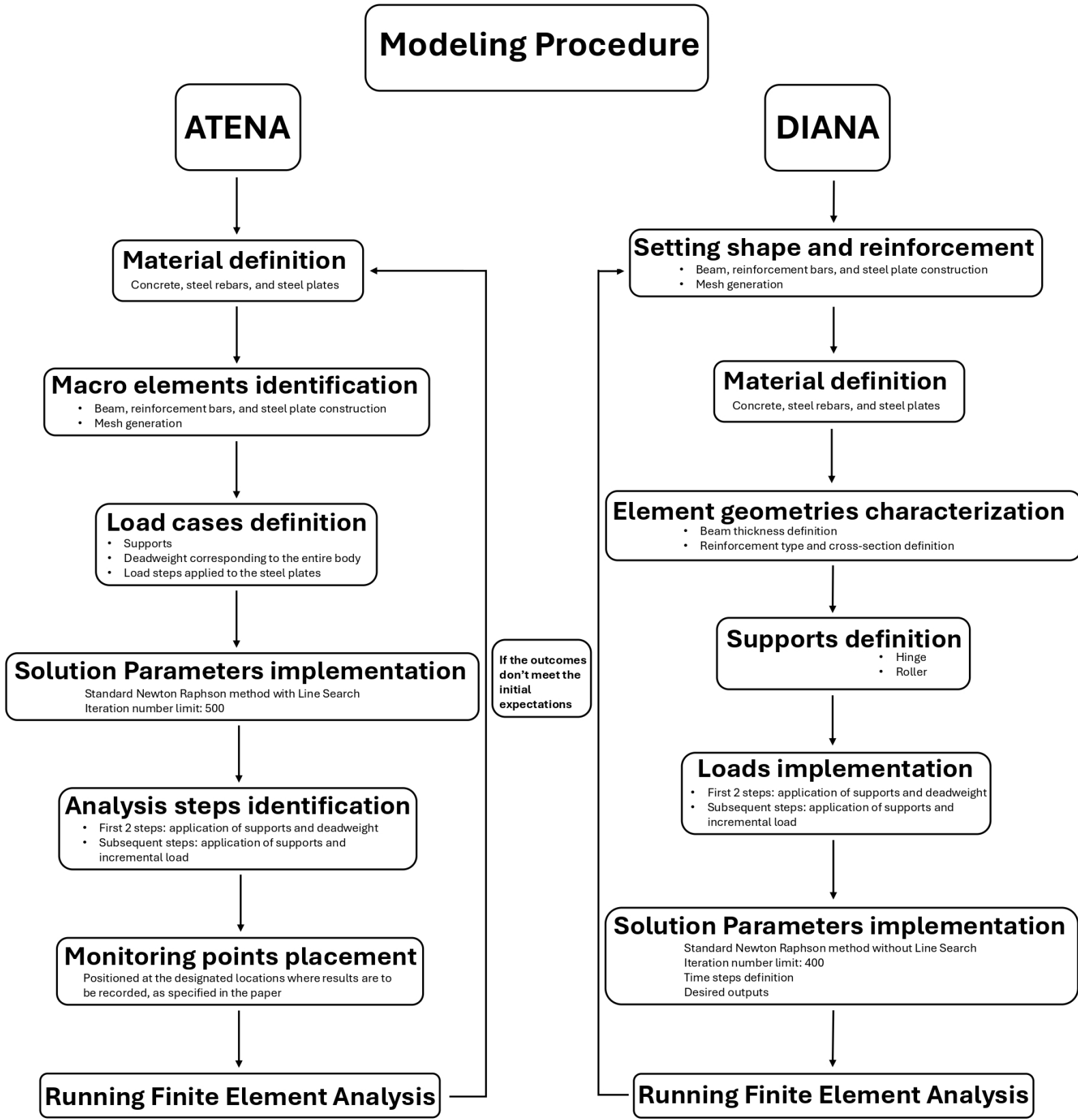


Figure 3.1: Comprehensive framework for modeling 2D structures in ATENA and DIANA

Chapter 4

4.1 NLFE Models

4.1.1 Identification of failure mechanism in RC beams

During experiments of RC beams approaching their ultimate limit state, various failure modes can occur. Making choices in a solution strategy requires understanding which phenomena need to be modeled, and in the post-processing phase, it is necessary to verify that the failure mechanisms observed in the analytical model correspond to those described in the experimental results.

In this thesis, 2 main collapse mechanisms have been investigated:

- Bending failure
- Shear failure

Bending failure

It arises when the cross-section is no longer able to withstand the bending moment. Initially, flexural cracks take place in the middle of the beam, where the bending moment is at its maximum. When the cracking stage reaches a stalemate and the load progressively increases, the reinforcement begins to yield at one or more of these cracks. This leads to large deformations while the load is still sustained. Consequently, 2 phenomena may occur: in over-reinforced beams, the compression zone crushes, or the bottom reinforcement fails in tension and in these cases, the beam is under-reinforced. The first case is a clear example to debunk the myth that the “more steel there is, the better it is”. In an over-reinforced beam, there is more tensile reinforcement than what is needed to balance the compressive strength of the concrete. Therefore, the failure mechanism is brittle, with the cracking of the concrete and the rebars that are unstressed. From a design point of view, this is not the optimal choice because it’s not a safe solution for the users, due to the sudden failure that doesn’t allow for the implementation of preventive measures. Moreover, it doesn’t exploit completely the mechanical properties of the steel, which is the most expensive material in an RC beam. Regarding the second case, the beam fails in a ductile manner, and a well-done design procedure should prefer this option to guarantee time for implementing containment measures when the structure shows clear signs of upcoming failure. During the loading steps, the tensile reinforcement yields, and the concrete in the compression zone doesn’t crush because the amount of steel under tension

is less than what is needed to balance the compressive strength of the concrete [15]. A clear example of an under-reinforced beam is the BF-1. Image 4.1 illustrates its failure mode in the experiment, image 4.1a, where the concrete is crushed in the upper part of the beam. On the right side instead, the image 4.1b shows the results from the NLFEA in software A. It's quite evident how the same region highlighted in 4.1a is subjected to higher stress values, represented by a darker grey shade. The problem emphasized in the previous chapter regarding the steel plates, which are often surrounded by areas with important stresses, is also visible.

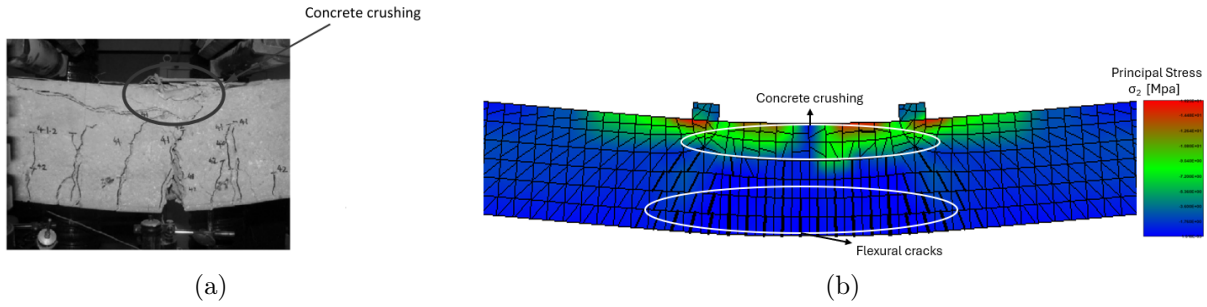


Figure 4.1: (a) BF-1 experimental failure (b) BF-1 failure in NLFE model

Specimen	Failure mode	
	EXP	FEM
BF-1	CC	CC

CC: concrete crushing

Table 4.1: BF-1 mode of failure

Shear failure

Shear failure of RC beams remains challenging to predict accurately and for this reason over the years, extensive experimental research has been conducted and despite the help of the newest sophisticated computational modeling tools, it is still not fully clear. In the case of a beam not properly designed for shear reinforcement, a brittle collapse due to the shear mechanisms is likely once it reaches its peak load. The shear analysis in RC structural elements is much more complex than the investigation for axial load and flexure. For those, the analysis is based on the 3 fundamental mechanical principles that must be fulfilled simultaneously to guarantee the stability, strength, and serviceability of structural elements:

- i. Equilibrium between internal and external forces
- ii. Compatibility of strains in both concrete and steel
- iii. Constitutive relationships of materials

The conventional analysis for shear instead, is just based on simple equilibrium equations of forces; on the other hand, the second and third principles don't come into play during this type of analysis. The strength of concrete under shear is primarily based on test results, rather than assessed through mechanical relationships. In beams, shear stresses

are triggered by bending or twisting and these two types of shear stress are called respectively flexural and torsional shear stresses. However, in this thesis, performing 2D plane stress NLFEAs, only the first case has been investigated (type of shear failure).

Diagonal tension failure

The entire process of shear failure in an RC beam can be divided into three main stages: in the initial one, the oblique cracks have not formed yet and there is a linear relationship between applied force and displacement equal to the concrete's young modulus. It indicates that, before the oblique cracks appear, the beam shear bearing capacity is primarily governed by the concrete's mechanical properties. Indeed, the empirical observations clearly show that the cracking loads of various RC beams, with the same concrete but different shear reinforcement ratios, are roughly the same because the stirrup ratios have little influence on them. This phase finishes when the cracking load is achieved. During the loading phase, the tensile stress increases, and when the tensile strength of concrete is overcome, the cracks start to occur in the direction perpendicular to the direction of principal tensile stress. They are vertical flexural cracks, and they arise first in the mid-span area, followed by the shear ones. Increasing the load, a few more diagonal cracks arise and one of them may grow into a dominant diagonal crack, going from the support to the loading point [37].

The second stage starts with the crack formation, leading to a slight decrease in the shear force, and a sudden increase in the corresponding displacement. These oblique cracks cause an internal force redistribution, which helps maintain the linear relation between force and displacement but with a reduction of beam stiffness. The experimental observations demonstrate that if the stirrup ratio is greater, the stirrups guarantee a better restraint effect on RC beams, also demonstrated by a weaker degradation of their stiffness. After oblique cracks appeared, stirrups began to play a shear role due to limiting the development of oblique cracks. The high stirrup ratio improves the shear bearing capacity of RC beams, and the displacement corresponding to peak-load is improved. This indicates that stirrups can effectively inhibit the development of cracks inside beams, thus enhancing the bite force between aggregates and improving the shear-bearing capacity of RC beams [37]. When the stirrup ratio is higher, it means that more stirrups are involved in shear resistance, enhancing the restraint effect on RC beams, and at the same time each of them must support a smaller shear force. The literature has demonstrated during the experiments that with the increase of beam height, the strain of stirrups increases significantly, which indicates that the shear contribution of stirrups in large-size RC beams is more considerable. This is probably due to the formation of more and larger oblique cracks in this type of beam, which makes the stirrup contribution to shear resistance significant [32].

The third stage involves the descending branch after the peak load. After reaching the peak load, the supported load decreases suddenly, and so does the stiffness. The shear failure occurs, and the beam loses its entire bearing capacity. With the increase in stirrup ratio, the descending section exhibits a relatively soft behavior, indicating that the presence of stirrups also affects the beam's behavior after the peak, improving its ductility and deformation capacity [37].

A good example of this phenomenon can be observed in specimen S8-90, previously described. After a certain level of load, roughly 300 kN, the beam's stiffness dropped, likely due to the yielding of stirrups. The deformations of the beam have a high dependency on the diameter, type of shear reinforcement, and its inclination α . In this specific case, the beam was reinforced only with steel stirrups, reaching the ultimate load of 470 kN. Image

4.2a shows the beam at the end of the experiment, characterized by an evident shear failure mechanism with its characteristic diagonal development of the crack pattern. On the right instead, image 4.2b illustrates the FEM, which replicates quite accurately what happens in the test. While the load on the beam increases, the cracks grow both in width and length, turning diagonally and propagating to the upper part of the beam toward the loading point. Immediately after reaching the peak load, the stage of shear tension failure occurs with a characteristic sudden failure. This mechanism is typical in beams with low shear reinforcement or when the shear-span-to-depth ratio (a/d) is greater than 2, as in this case.

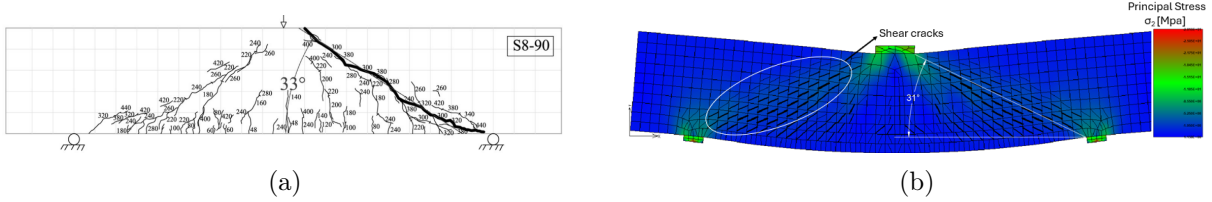


Figure 4.2: (a) S8-90 experimental failure (b) S8-90 failure in NLFE model

Specimen	Failure mode	
	EXP	FEM
S8-90	DT	DT

DT: diagonal tension failure

Table 4.2: S8-90 mode of failure

Shear compression failure

As mentioned earlier, after the flexural cracks form, the concrete stops contributing to the bearing capacity in the cracked area, and the structural element can no longer be considered an elastic body. At this point, the tensile forces are carried by longitudinal reinforcement, and therefore the state of stress remains elastic but with a different stiffness. By increasing the load, the flexural crack propagates into the compression zone of the beam. In both side spans, the inclined cracks begin to develop and when these appear, the tensile force carried by concrete is released [37]. After this stage, two possible resistance mechanisms can emerge:

- If the reinforcement in the direction of principal tensile stress is absent or insufficient, the beam will fail suddenly due to a diagonal tension failure, and it will fall in the case of previously analyzed specimen S8-90.
- If the element can withstand the increasing load after the development of diagonal cracks, the stress state evolves into a compression arch formed by diagonal cracks. In this scenario, the load is transferred through the arch system and the beam fails when it crushes under an excessive diagonal compression. This failure mode is known as shear compression failure.

Both mechanisms strongly depend on the (a/d) ratio, and the shear compression failure usually happens when it ranges between 1 and 2. For instance, specimen B44-1.5W failed exactly in this way and the image 4.6a shows the beam after the experiment. On the right side instead, the image 4.6b displays the results obtained with the FEM, which faithfully reproduces what happened in the experiment.

Indeed, beam B44-1.5W has a shorter shear span and a smaller stirrup spacing compared to the S8-90, leading to the formation of diagonal cracks extending almost the full beam depth, from the support to the loading point. However, thanks to the relatively high shear reinforcement which acts as a tie, these diagonal cracks remained narrow and did not widen so much during the loading stage. Other diagonal cracks arose alongside the first one as the load was increased, resulting in a series of inclined concrete struts. This behavior closely follows the principles of the Strut-and-Tie Model (STM) and the transverse steel, working effectively in restraining diagonal shear cracking, enables the shift from a diagonal tension failure to shear compression failure. The model mentioned above describes how the forces are transferred from the point of load application to the supports: through the inclined compression struts and the transverse steel ties. This highlights the importance of a well-designed shear reinforcement, which allows the beam to fail with a more gradual mechanism when the concrete's compressive capacity in the nodal zones is exceeded.

The empirical observations demonstrate that in the case of RC beams with shear reinforcement, the number of cracks increases as the compressive strengths of concrete rise, indicating a better redistribution of internal forces in the beams made of high-strength concrete. A possible explanation of this phenomenon may be the stronger bond between concrete and steel rebars, which translates to a relatively better efficiency in the use of reinforcing steel. Consequently, the beam can maintain its serviceability conditions and resist cracking more effectively up to the ultimate state [37].

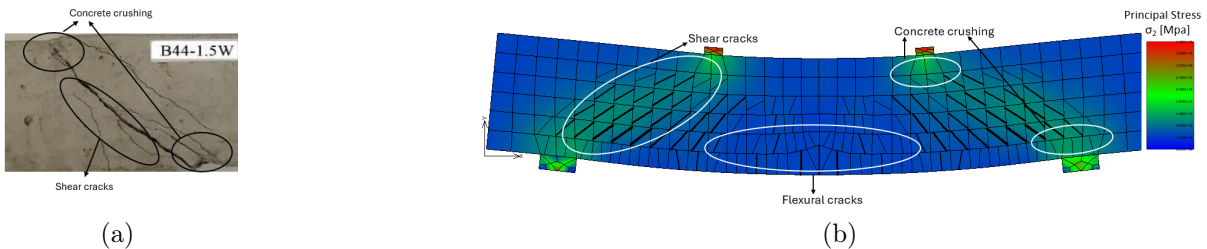


Figure 4.3: (a) B44-1.5W experimental failure (b) B44-1.5W failure in NLFE model

Specimen	Failure mode	
	EXP	FEM
B44-1.5W	SC	SC

SC: Shear-compression failure

Table 4.3: B44-1.5W mode of failure

To have a comprehensive understanding of all possible failure modes that happened during the modeling phase of this work, several representative examples are shown below. In each case, the experimental failure mode coincides with the one observed in the NLFE model, including key characteristics like crack pattern.

In the next subsection, each beam will be analyzed through its load-deformation curve and categorized according to its failure mode. Therefore, for each of the 35 beams, after the NLFEA with both software, the resulting crack pattern, deformation, and stress zones can be attributed to one of three distinct failure modes just mentioned above.

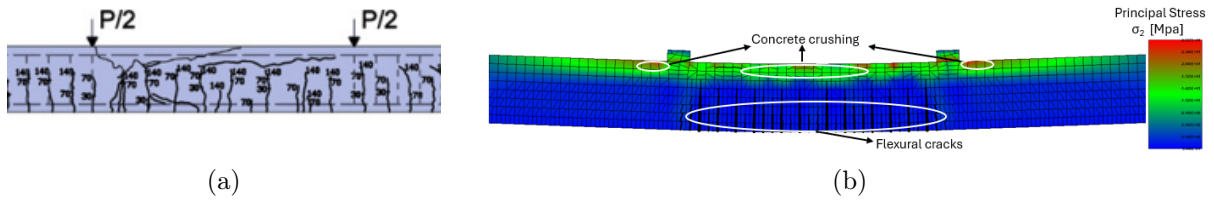


Figure 4.4: (a) BP-C-4 experimental failure (b) BP-C-4 failure in NLFE model

Specimen	Failure mode	
	EXP	FEM
BP-C-4	CC	CC

CC: concrete crushing

Table 4.4: BP-C-4 mode of failure

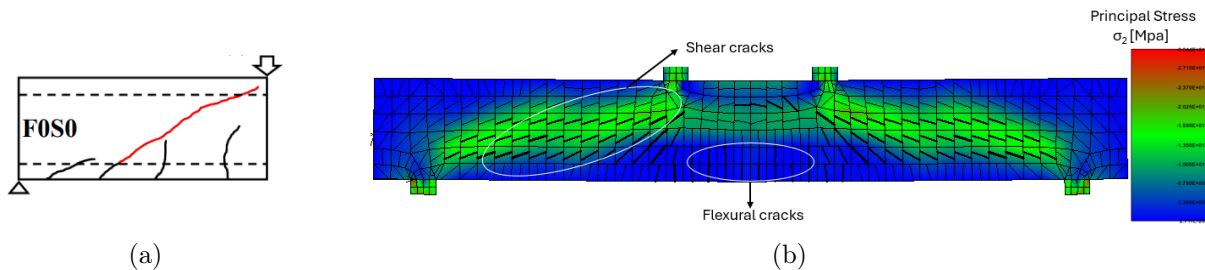


Figure 4.5: (a) FOS0 experimental failure (b) FOS0 failure in NLFE model

Specimen	Failure mode	
	EXP	FEM
FOS0	DT	DT

DT: diagonal tension failure

Table 4.5: FOS0 mode of failure

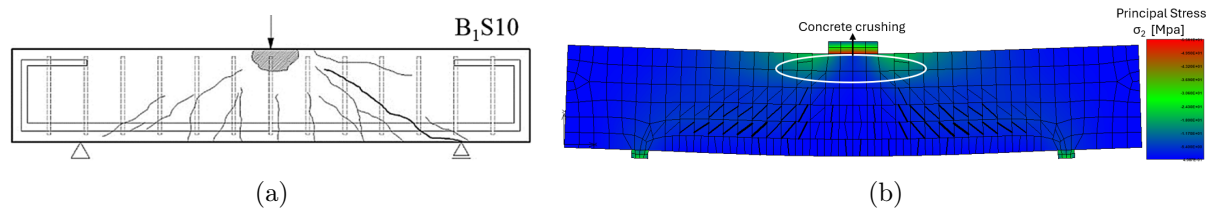


Figure 4.6: (a) B1S10 experimental failure (b) B1S10 failure in NLFE model

Specimen	Failure mode	
	EXP	FEM
B1S10	SC	SC

SC: Shear-compression failure

Table 4.6: B1S10 mode of failure

4.1.2 Finite Elements Models: NLNAs results

Specimens experiencing flexural failure

Specimen [-]	Experiment [kN]	Software A			Software B		
		Brittle [kN]	LTS [kN]	Plastic [kN]	Brittle [kN]	LTS [kN]	Plastic [kN]
S-501	127	109	110	130	110	115	140
CF	56	60	62	78	57	57	65
CS	54.2	56	56	64	45	58	66
CT	53.8	56	58	64	45	58	61
BF1-1	43	48	48	54	36	37	48
B-PC-2	89	98	98	112	96	97	141
B-PC-4	168	174	174	178	179	184	215
RC-1	76	74	74	82	63	64	77
A211	462	490	500	540	445	468	530
B312	732	710	710	820	710	718	798
B313	745	740	740	820	720	723	803
B321	767	760	760	850	730	735	823
C211	650	640	640	770	605	610	710
C311	731	710	720	840	681	703	795
C411	898	890	890	960	620	875	955

Table 4.7: Comparison of experimental and software results

Table 4.7 summarizes the results in terms of the maximum load sustained by the beams, comparing the experimental results shown in the second column and the outcomes from the software A and B, both implementing the 3 modeling hypotheses. This table allows for a visual evaluation of how well the NLFE models can reproduce the behavior of each beam and the following load-deformation curves provide an insight into their structural response and failure mechanisms, underlying not just the final number of failure loads but the entire loading process. As expected, the 2 software are not able to accurately predict the behavior of each RC structure, and the reason behind these discrepancies can be explained by looking at both structures:

- The experimental element may present particularly high-performance thanks to many aspects, such as severe intergranular interactions and strong bonding between steel reinforcement and concrete, which lead to performance levels beyond what might be typical for another RC structure with equal mechanical properties. Even employing the most sophisticated tools, like the NLNA, it's never easy to capture the endless aspects and complexity of each structure that result in being unique.
- In some cases, the NLFE model doesn't accurately catch the exact resistance mechanism and/or the resulting failure mode, therefore the analysts have to interpret and evaluate the results according to their knowledge, establishing if they are reliable. This highlights the key concept of the right approach to this advanced method: while there will be more and more sophisticated simulations that faithfully replicate the mechanical behavior of structures, the analyst's role remains crucial, and it will probably be even more essential. Through his knowledge, he can interpret

and select the right safety formats to ensure optimal design choices, suited to that specific project. No software can't substitute this fundamental judgment phase.

It's reasonable to expect that these discrepancies enlarge when the RC structures are made with particular concrete and reinforcement, like high-performance concrete and FRP rebar because many factors come into play and the actual resistance mechanisms become more difficult to predict by an NLN software. At the same time, it may happen with a more complex failure mechanism, as shown in table 4.8, for the shear failure mode.

Load-deformation curves

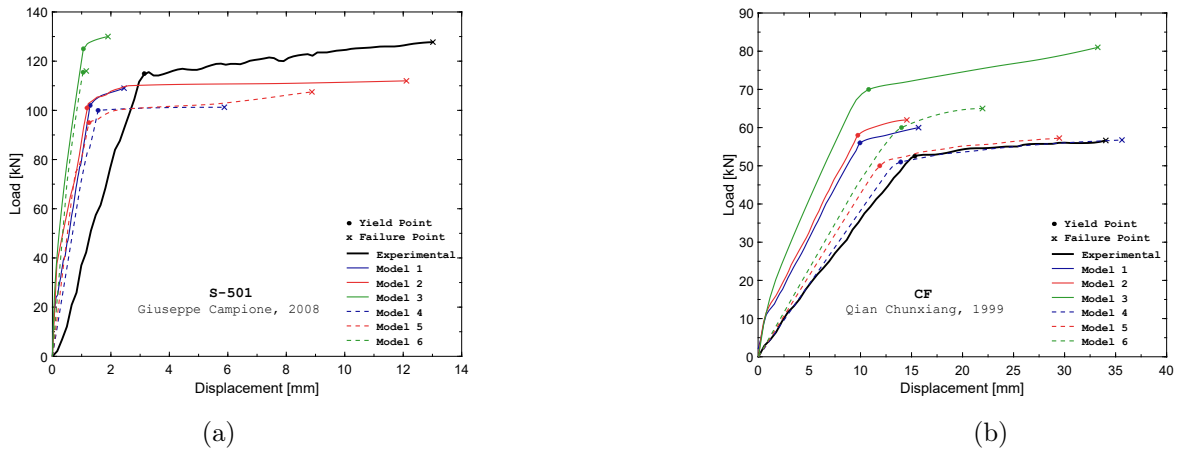


Figure 4.7: (a) Specimen S-501: Load vs. Displacement Curve (b) Specimen CF: Load vs. Displacement Curve

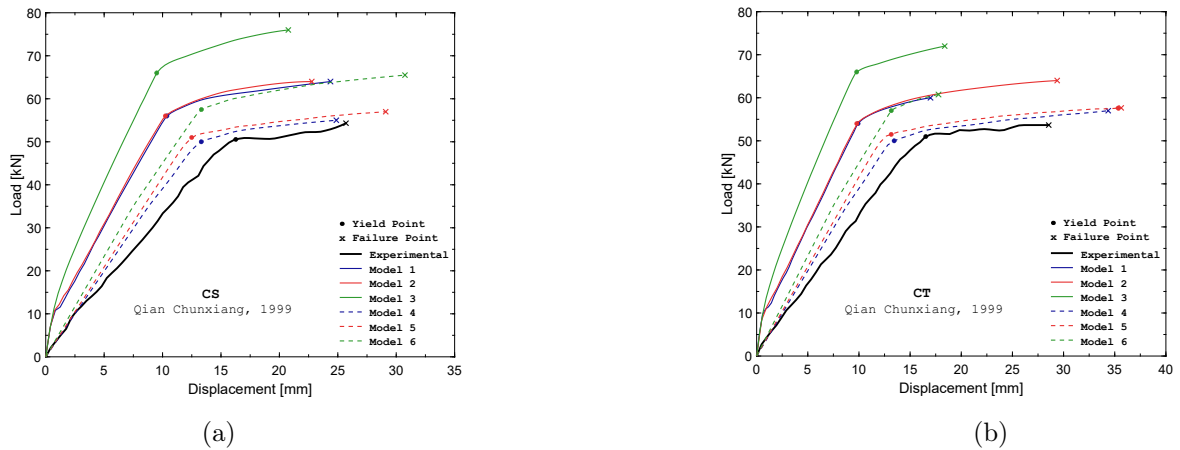
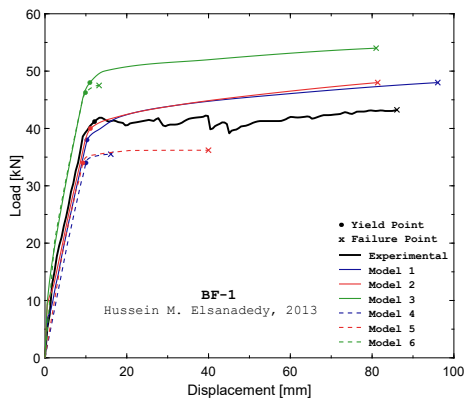
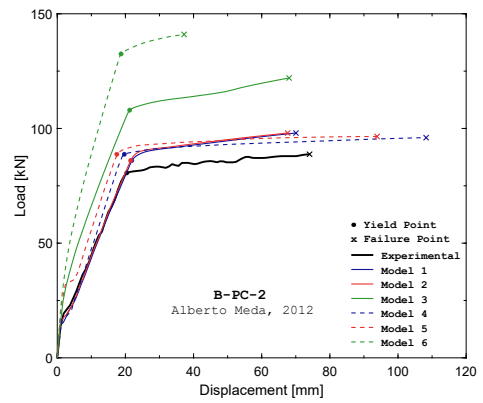


Figure 4.8: (a) Specimen CS: Load vs. Displacement Curve (b) Specimen CT: Load vs. Displacement Curve

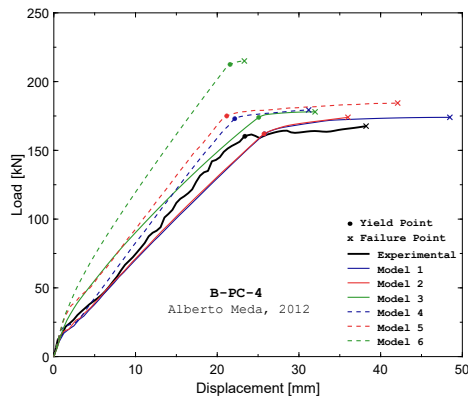


(a)

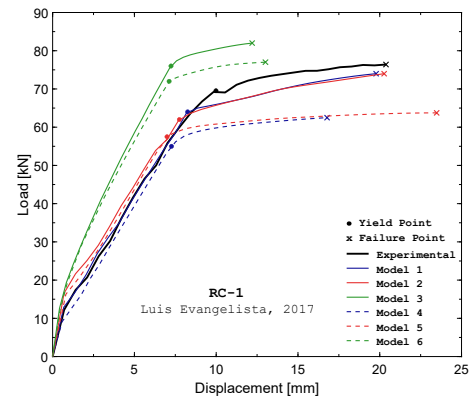


(b)

Figure 4.9: (a) Specimen BF-1: Load vs. Displacement Curve (b) Specimen B-PC-2: Load vs. Displacement Curve

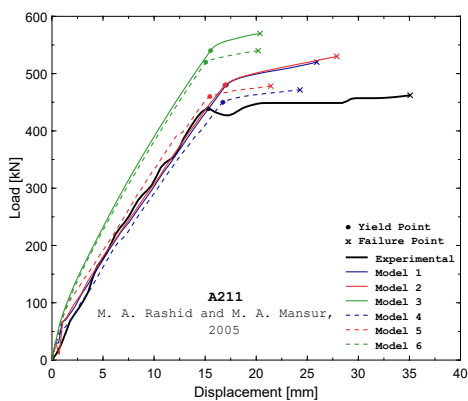


(a)

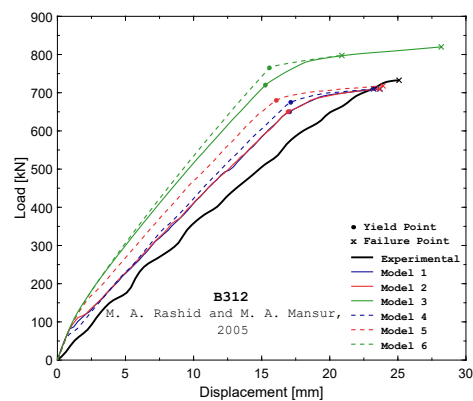


(b)

Figure 4.10: (a) Specimen B-PC-4: Load vs. Displacement Curve (b) Specimen B-PC-2: Load vs. Displacement Curve

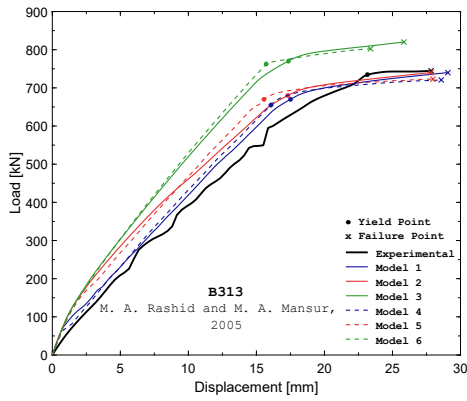


(a)

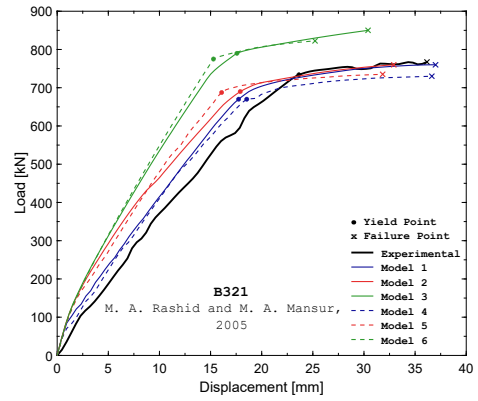


(b)

Figure 4.11: (a) Specimen A211: Load vs. Displacement Curve (b) Specimen B312: Load vs. Displacement Curve

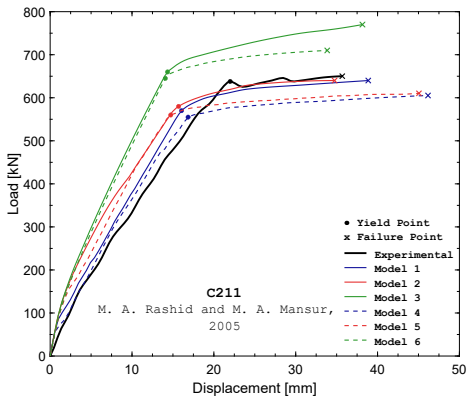


(a)

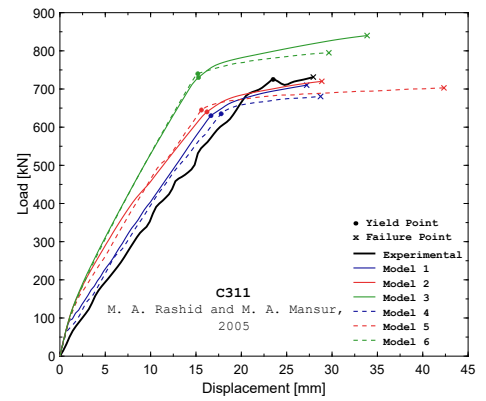


(b)

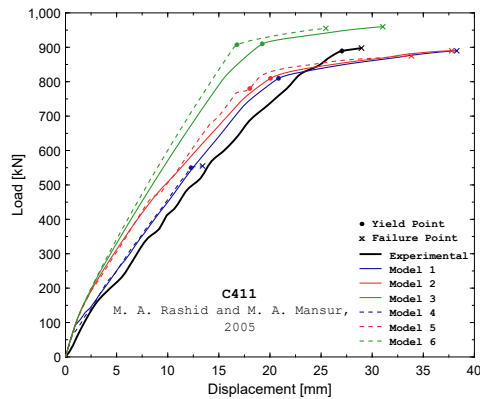
Figure 4.12: (a) Specimen B313: Load vs. Displacement Curve (b) Specimen B321: Load vs. Displacement Curve



(a)



(b)



(c)

Figure 4.13: (a) Specimen C211: Load vs. Displacement Curve (b) Specimen C311: Load vs. Displacement Curve (c) Specimen C411: Load vs. Displacement Curve

Specimens experiencing shear failure

Specimen [-]	Experiment [kN]	Software A			Software B		
		Brittle [kN]	LTS [kN]	Plastic [kN]	Brittle [kN]	LTS [kN]	Plastic [kN]
S-0.157	311	333	333	382	186	200	256
S-0.314	340	361	361	378	265	275	365
S-0.628	409	428	428	450	306	333	351
S-0.942	422	430	430	450	297	378	414
B1S06	203	204	210	228	180	192	192
B1S10	247	216	222	222	209	230	223
B2S06	236	246	246	252	210	222	216
S06	242	220	220	260	177	197	182
S10	296	260	260	275	180	207	216
S8-90	470	450	450	510	364	420	519
F0S0	115	122	122	152	84	112	136
ST80	251	280	280	302	206	230	234
ST120	215	160	225	300	148	190	222
B44W2	142	130	132	142	100	100	92
B44W1.5	174	172	174	184	195	213	222.5
A01	178	224	224	260	162	162	186
A02	228	264	264	272	198	228	186
B02	284	302	302	302	234	258	252
RCTB1	2179	2460	2480	2880	2200	2280	2360
RCTB3	1140	1160	1200	1440	1020	1040	1060

Table 4.8: Comparison of experimental and software results

Table 4.8, as already mentioned earlier, compares the experimental results (second column) with the outcomes from the software A and B, both implementing the 3 modeling hypotheses, in terms of maximum load sustained by the beams. The possible reasons behind the discrepancies are the same as in the previous case, but most likely the NLFE models are affected by higher uncertainties than the flexural case. This is proven by a larger discrepancy between results obtained through experimental tests and NLFEA. This is in line with the previous sections where it's emphasized the unknowns regarding the shear failure mode on both sides, in literature and, as a direct consequence, also in the modeling process.

In analyzing beams that fail with a shear mode, the primary reinforcement that comes into play as a resistance mechanism is the stirrup. Therefore, it's fundamental to identify which stirrups undergo plastic deformations or fail, considering their pivotal role in the beam's overall shear resistance. After the creation of the first crack, concrete's contribution to load bearing starts decreasing hand in hand with the development of subsequent cracks, and in this area, the steel reinforcement starts working. Immediately after the formation of the first crack, the steel entirely bears the force in the cracked area and the stress in the concrete falls to 0. In the region adjacent to the crack, an intermediate region known as the transfer length exists, and it's characterized by partial bond breakdown. There, the concrete and steel stresses vary significantly due to the released stress in concrete and, if the axial load overcomes the threshold that causes the first crack, new primary cracks continue to form. This process continues until the final crack pattern is

fully developed. Table 4.9 shows which stirrup was the first to experience plastic deformation: the numbering can start from both sides, left or right being symmetric structures. In most cases, the numbers are the same in software A and software B, proving that both tools' resistance mechanisms are the same.

Specimen [-]	First reinforcement yielding point	
	Software A	Software B
S-0.157	4	4
S-0.314	4	4
S-0.628	5	4
S-0.942	6	6
B1S06	5	7
B1S10	5	4
B2S06	5	5
S06	5	4
S10	6	6
S8-90	4	4
F0S0	2	2
ST80	4	4
ST120	3	4
B44W2	3	3
B44W1.5	3	3
A01	2	2
A02	2	2
B02	4	4
RCTB1	4	4
RCTB3	4	5

Table 4.9: First yielding stirrup for different specimens using Software A and Software B

Load-deformation curves

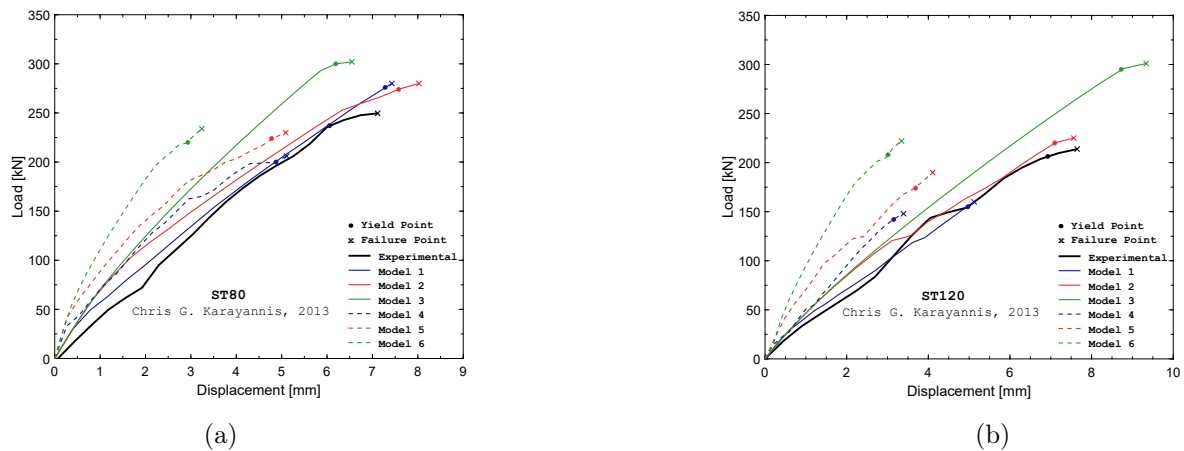
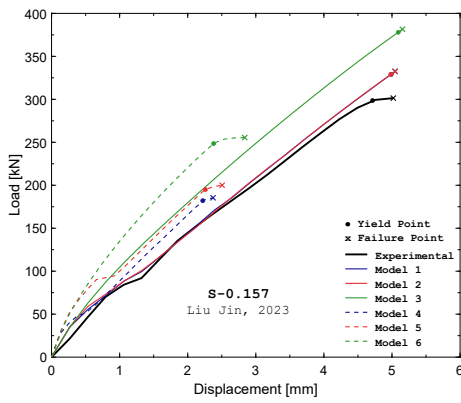
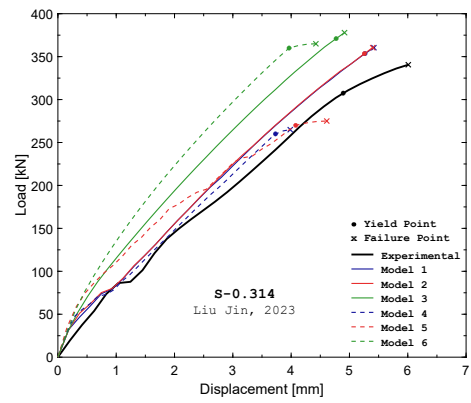


Figure 4.14: (a) Specimen ST80: Load vs. Displacement Curve (b) Specimen ST120: Load vs. Displacement Curve

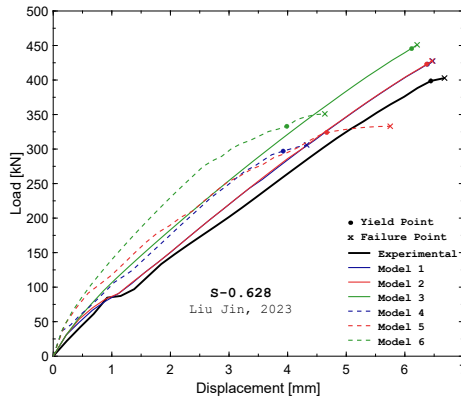


(a)

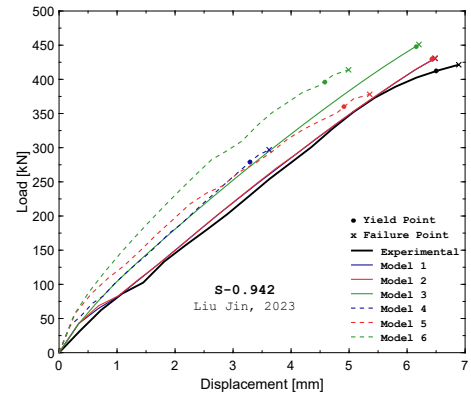


(b)

Figure 4.15: (a) Specimen S-0.157: Load vs. Displacement Curve (b) Specimen S-0.314: Load vs. Displacement Curve

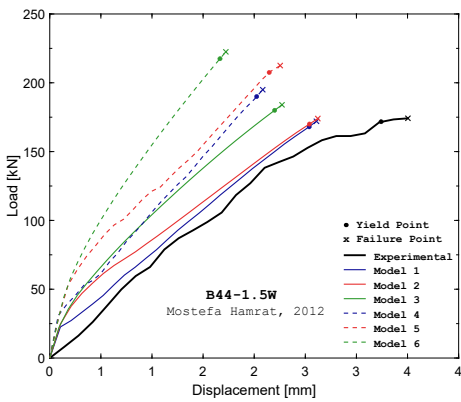


(a)

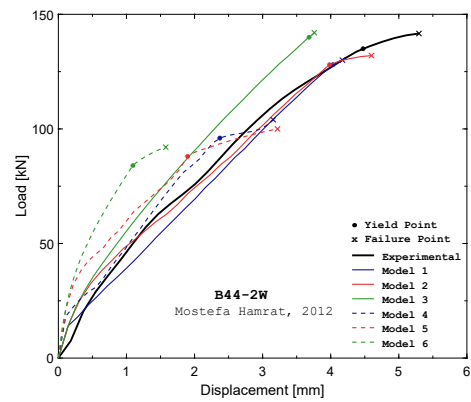


(b)

Figure 4.16: (a) Specimen S-0.628: Load vs. Displacement Curve (b) Specimen S-0.942: Load vs. Displacement Curve

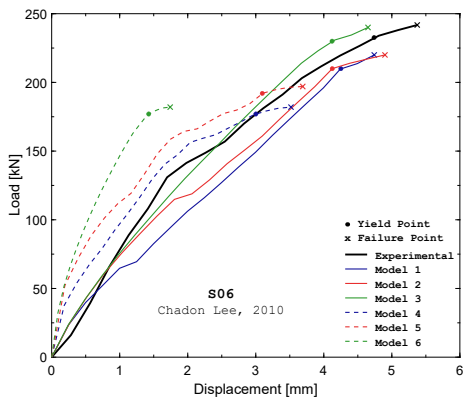


(a)

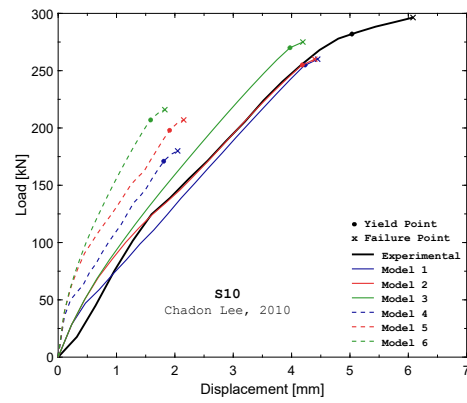


(b)

Figure 4.17: (a) Specimen B44-1.5W: Load vs. Displacement Curve (b) Specimen B44-2W: Load vs. Displacement Curve

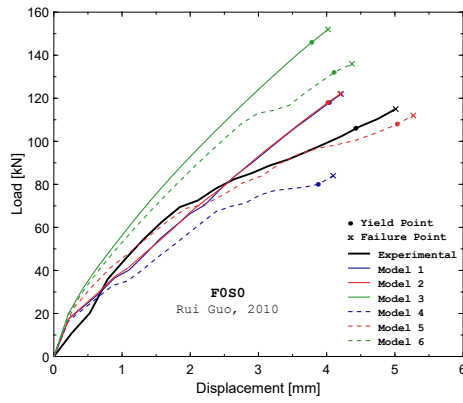


(a)

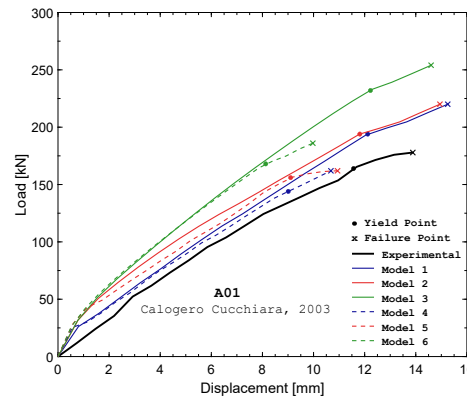


(b)

Figure 4.18: (a) Specimen S06: Load vs. Displacement Curve (b) Specimen S10: Load vs. Displacement Curve

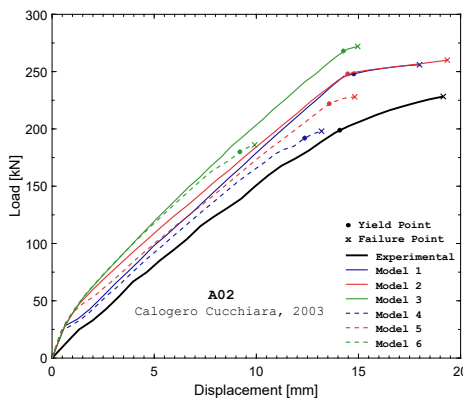


(a)

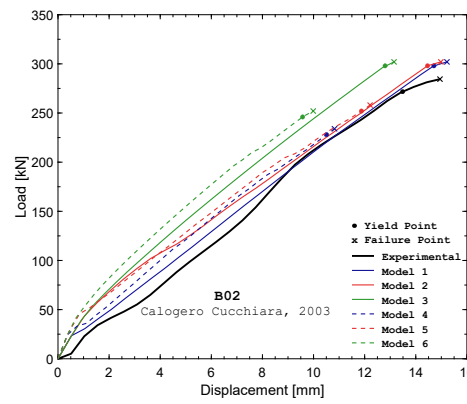


(b)

Figure 4.19: (a) Specimen F0S0: Load vs. Displacement Curve (b) Specimen A01: Load vs. Displacement Curve



(a)



(b)

Figure 4.20: (a) Specimen A02: Load vs. Displacement Curve (b) Specimen B02: Load vs. Displacement Curve

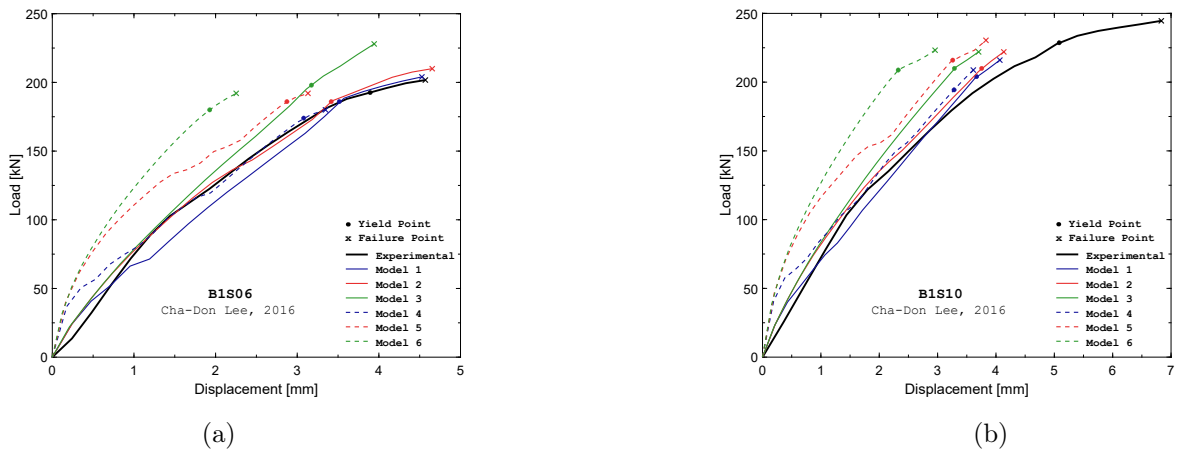


Figure 4.21: (a) Specimen B1S06: Load vs. Displacement Curve (b) Specimen B1S10: Load vs. Displacement Curve

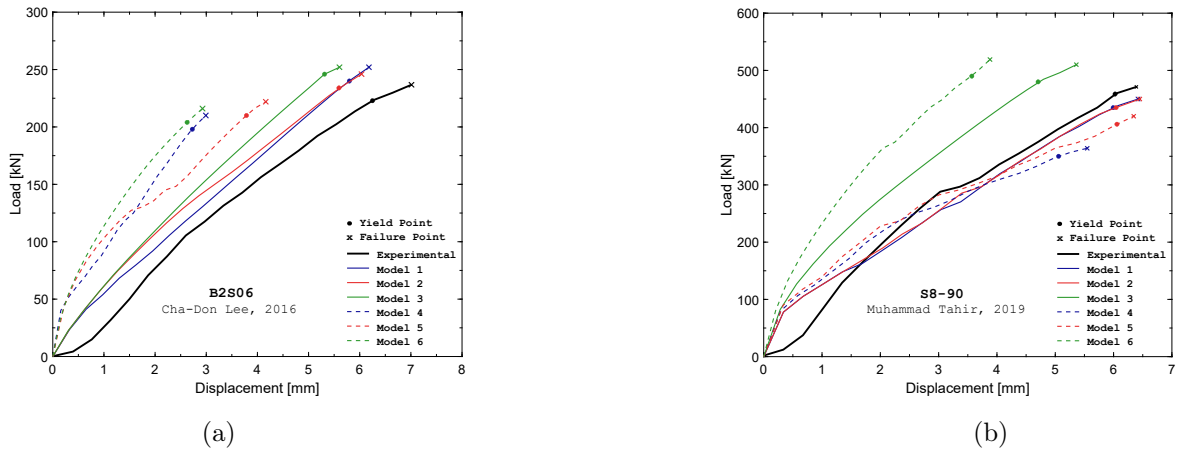


Figure 4.22: (a) Specimen B2S06: Load vs. Displacement Curve (b) Specimen S8-90: Load vs. Displacement Curve

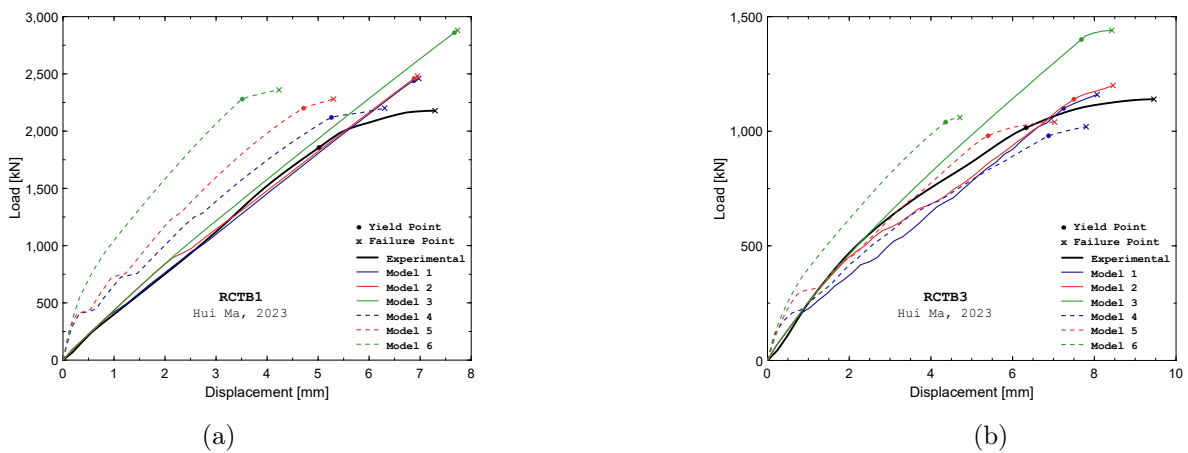


Figure 4.23: (a) Specimen RCTB1: Load vs. Displacement Curve (b) Specimen RCTB3: Load vs. Displacement Curve

Chapter 5

5.1 Uncertainty in NLNA Models of RC Beams

5.1.1 Model uncertainty safety factor

Real behavior prediction of an RC structure is the primary goal of the NLNA, considering its components' nonlinear effects. However, numerical models inherently contain uncertainties, making them just an accurate idealization of physical reality. This happens due to neglected aspects or informed choices in the model's resolution. These uncertainties are known as epistemic.

The thesis focuses on a comprehensive and accurate assessment of the model uncertainty safety factor, γ_{Rd} . It comes into play in the Global Resistance Format (GRF) for evaluating the global design structural resistance R_d , as shown earlier in the equations 1.1 and 1.3. This coefficient considers all the uncertainties related to the model: numerical approximations in solving nonlinear equations, incomplete knowledge that leads to assumptions, and simplifications throughout defining the structural model and software's limitations.

In this phase, the analysis concentrates solely on epistemic uncertainties. In contrast, aleatory ones are not being considered in this work. Still, they are explored by my colleague Stefano in his thesis and the references 16, and 17 (Model uncertainty in non-linear numerical).

Quantifying the epistemic uncertainties in the model involves introducing a new variable: the resistance model uncertainty θ . This variable represents the ratio between the resistance given by the experimental tests, $R_{exp,i}(X, Y)$, and the one obtained from the nonlinear analysis, $R_{NLFEA,i}(X)$. X and Y are vectors where the first contains variables considered in the models, while Y gathers variables that, though influencing resistance mechanisms, are neglected. For example, the confinement in beams, achieved through stirrups encircling the longitudinal reinforcement and enhancing in that way the overall beam performance, has not been explicitly incorporated into numerical models. However, the vector θ , statistically characterized by a mean μ_θ and variance σ_θ^2 , is influenced by both X and Y , indirectly accounting for the contribution of unknowns [6].

$$\theta_i \approx \frac{R_{exp,i}(X, Y)}{R_{NLFEA,i}(X)} \quad (5.1)$$

With knowledge of both the first and second-order central moments of the distribution, it's possible to determine the model uncertainty safety factor:

$$\gamma_{R_d} = \frac{1}{\mu_\theta \cdot \exp(-\alpha_R \beta V_\theta)} \quad (5.2)$$

5.1.2 Assessing model uncertainty

For this analysis, two groups of beams are examined:

- 15 beams subjected to flexural failure
- 20 beams subjected to shear failure

The experimental results, $R_{\text{exp},i}$, were obtained through three-point or four-point bending tests. The ultimate load capacities of the beams, as determined experimentally, were compared with the results from Nonlinear Finite Element Analyses (NLFEMs) conducted using software A and B, $R_{\text{NLFEA},i}$. To achieve a more robust and comprehensive calibration of the model uncertainty safety factor, and to align with the approach outlined in references [6], it is essential to differentiate between different modeling hypotheses. In this way, the thesis encompasses the wholeness of possibilities that an analyst can explore during the modeling process. It's worth noting that model uncertainty is related to the solution strategy adopted, therefore choices that involve physical, geometrical, or other uncertainties are integrated with different uncertainty factors, such as the Global Resistance Safety Factor γ_R .

Typically, concrete shows quasi-brittle compressive responses and brittle behavior under tensile forces. The steel bars, indeed, are always integrated within the concrete structure to compensate for its lack of tensile strength. These elements work well because they can create heavy bonds with concrete, promoted by the rib on their surface, ensuring the tension-stiffening effect. Like the dowel effect, where cracked concrete allows rebars to transfer load across the cracks, enhancing the overall shear resistance; tension stiffening arises from the strong interaction between steel and concrete. It improves significantly the beam's stiffness and only modestly its tensile resistance, reducing crack widths and spacing. To incorporate this effect in numerical simulations, the constitutive tensile model can be modified by adopting different tension-softening laws, which simulate the post-peak behavior of concrete in tension [11]. Therefore, 3 distinct hypotheses regarding the concrete behavior in tension have been discussed:

- elastic-brittle
- elastic with post-peak linear tension softening (LTS)
- elastic with a perfectly plastic response

The first and third hypotheses embody the two extreme possibilities of concrete's tensile performance. Although they can't be considered real physical representations of possible failure mechanisms of RC beams, they are necessary for outlining boundary limits, encompassing the epistemic uncertainty associated with material modeling. Instead, the LTS case has been calibrated to closely match the experimental load-displacement curve for each beam. The calibration assumes that Young's modulus of concrete in tension is equal to that in compression, using the elastic modulus and the concrete tensile strength

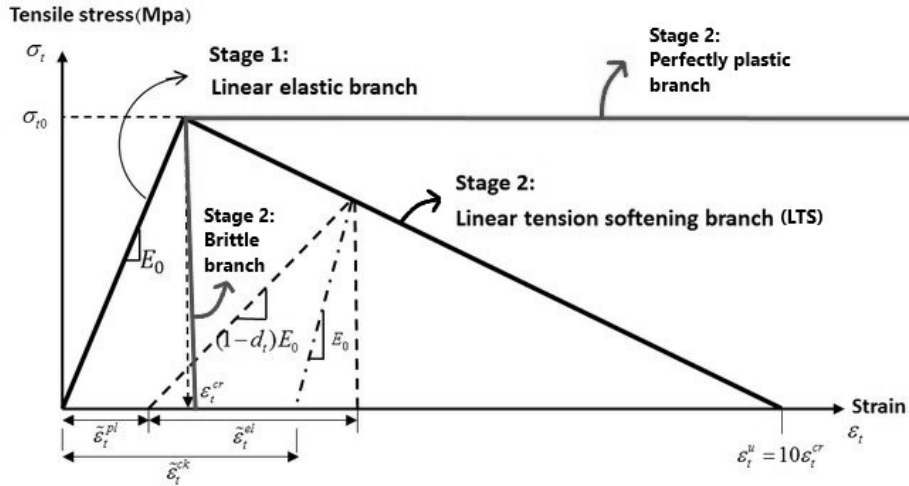


Figure 5.1: Uniaxial tensile stress-strain behavior for concrete and its softening branch assumptions.

as per EN1992-1-1:36 when no specific information is provided in the literature [42]. It's worth noting that different assumptions made during the modeling phase to describe the material's actual behavior impacts the constitutive models, kinematic laws, and equilibrium equations.

Beams experiencing flexural failure

In this case, therefore, 6 different structural models, M_j , have been defined for each beam, with j ranging from 1 to 6. Specifically, 3 models were created using software A, and three with software B. The result is a matrix $[15 \times 6]$ as shown in table 5.1.

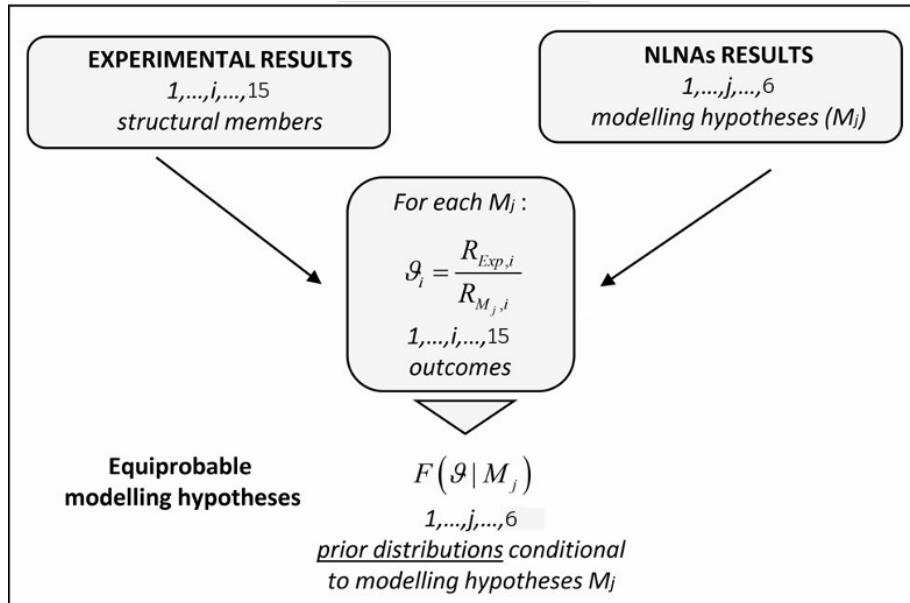


Figure 5.2: Prior information scheme

Table 5.1 shows that even when considering the theoretical extreme hypotheses about concrete's tensile behavior, they are not completely sufficient to encompass the experimental peak load, especially regarding the lower limit. In both software analyses, as predicted, θ never exceeds 1 for the plastic case but it overcomes the predicted bound,

Table 5.1: Resistance model uncertainty random variables

Software	A			B		
	Brittle	LTS	Plastic	Brittle	LTS	Plastic
Model	1	2	3	4	5	6
S-501	1.165	1.155	0.977	1.155	1.104	0.907
CF	0.933	0.903	0.718	0.982	0.982	0.862
CS	0.968	0.968	0.847	1.200	0.931	0.818
CT	0.961	0.928	0.841	1.200	0.931	0.885
BF1-1	0.896	0.896	0.796	1.194	1.162	0.896
B-PC-2	0.908	0.908	0.795	0.927	0.918	0.631
B-PC-4	0.966	0.966	0.944	0.939	0.913	0.781
RC-1	1.027	1.027	0.927	1.222	1.203	1.000
A211	0.943	0.924	0.856	1.038	0.987	0.872
B312	1.031	1.031	0.893	1.031	1.019	0.917
B313	1.007	1.007	0.909	1.035	1.030	0.928
B321	1.009	1.009	0.902	1.051	1.044	0.932
C211	1.016	1.016	0.844	1.074	1.066	0.915
C311	1.030	1.015	0.870	1.073	1.040	0.919
C411	1.009	1.009	0.935	1.448	1.026	0.940

falling below 1, when the elastic-brittle tension-softening law is implemented, as indicated in the first and third columns of table 5.1. The anomalies in the results and the challenge in capturing entirely the beam’s failure mode may derive from the necessity of further boundary conditions and multiple NLNAs to explore the combined influence of various parameters. The approach carried on in this thesis will establish a background for future NLN analyses, ensuring that the outcomes will reflect accurately the experimental results.

The obtained discrepancies observed in the peak load estimation when comparing numerical simulation with experimental results vary according to the solution strategy and the software considered. It’s worth highlighting some possible outliers like θ equal to 0.718 and 1.448 in the third and fourth models, respectively. This difference clearly shows that finite element models may not always accurately replicate experimental behavior and only a post-processing investigation can reveal the reason behind it. On the other hand, it is reasonable to expect that not all the beams, and more in general, RC structures, can be faithfully replicated with NLF software. Therefore, it’s essential to work with as large a sample as possible to draw conclusions that behave as general rules, rather than a simple description of a limited number of cases. The bias becomes potentially harmful when it derives from overestimations of concrete beam peak resistances, leading to potentially unsafe design choices. The only solution to prevent this risk is a meticulous calibration of the software, followed by applying at the final stage an appropriate conservative value for the resistance modeling uncertainty partial safety factor in NLFs. This approach proves effective: in the second and fifth columns in table 5.1, which correspond to the LTS models, most of the θ values are nearly equal to the unity, meaning a strong alignment between reality and the numerical model.

Except for just one case, both software, A and B behave similarly: in the LTS column, they consistently either overestimate or underestimate the peak load. Hence, any further adjustment subsequently implemented to achieve a θ equal to unity could work effectively

for both.



Figure 5.3: Modelling hypotheses and benchmark NLNAs

5.1.3 Statistic Inference

The choice to consider the 2 extreme tension-softening laws, elastic-brittle and elastic with perfectly plastic response, derives from the need to encompass engineers' choices during the modeling phase. As shown in figure 5.13, the process results in 90 non-linear simulations. The outcomes of these analyses are the R_{NLNA} values, which are then used as input data for the subsequent phase. The resistance model uncertainty random variable θ can be assessed by taking the ratio between the experimental resistance, R_{exp} , already known from the experiments, and the R_{NLNA} results. According to the literature and as suggested in the JCSS model code [31], a log-normal distribution is commonly assumed to describe its variability. However, the statistic inference procedure includes a series of sequential tests to ensure that our sample follows the general trend and avoids making assumptions. They confirm or reject the hypothesis that the log-normal distribution can appropriately fit the random variable θ before proceeding with the probabilistic analysis [35].

The statistical inference procedure aims to suit the probabilistic model to the data sample. To accomplish this, an optimization process is pursued, fitting the distribution through a correct assessment of its parameters. Before doing so, which is computationally intensive, it's preferable to first draw probability plots for each distribution under consideration. This type of graphical tool visually allows the analyst to realize how well a probabilistic model fits the data sample. It's a quantile-quantile (Q-Q) plot, that compares empirical and theoretical distributions. If the differences between them are only due to location and scale, governed by the parameters, the plot represents approximately a straight line [35].

The generic log-normal equations are:

$$P(\theta) = \frac{1}{\lambda_2 \sqrt{2\pi}} \int_{-\infty}^{\theta} \frac{1}{\theta} e^{-\frac{1}{2} \left(\frac{\ln(\theta) - \lambda_1}{\lambda_2} \right)^2} d\theta, \quad (5.3)$$

$$p(\theta) = \frac{1}{\theta \lambda_2 \sqrt{2\pi}} e^{-\frac{1}{2} \left(\frac{\ln(\theta) - \lambda_1}{\lambda_2} \right)^2}, \quad \theta > 0 \quad (5.4)$$

$$\theta(F) = e^{\lambda_1 + \lambda_2 \Phi^{-1}(F)}, \quad \lambda_2 > 0 \quad (5.5)$$

The graphical check of the random variable theta, depicted in images 5.4 and 5.5, suggests that the log-normal distribution may provide an appropriate description of its variability. Only after this step, it's worth proceeding with the optimization process. Specifically, figures 5.4a and 5.5a juxtapose the frequency histogram derived from the data with the log-normal probability density function. Meanwhile, the probability plots, in figures 5.4b and 5.5b, confirm the alignment of points. Similar behavior has been detected in the remaining sets of modeling hypotheses, which collectively constitute the prior information

set. A consistency test was also implemented: the six models were analyzed together, treating them as a unique sample of 90 random variables. Any misalignment in these graphs would lead to a change in the probabilistic model and restart the entire statistical inference process. However, even if the probability plots 5.4b and 5.5b show an alignment, it doesn't guarantee success in the tests.

For this procedure, 4 tests of adaptation have been selected:

- Chi-squared
- Anderson-Darling
- Jarque-Bera
- Lilliefors

For each test, the null hypothesis H0 assumes that the sample is drawn from a log-normal distribution.

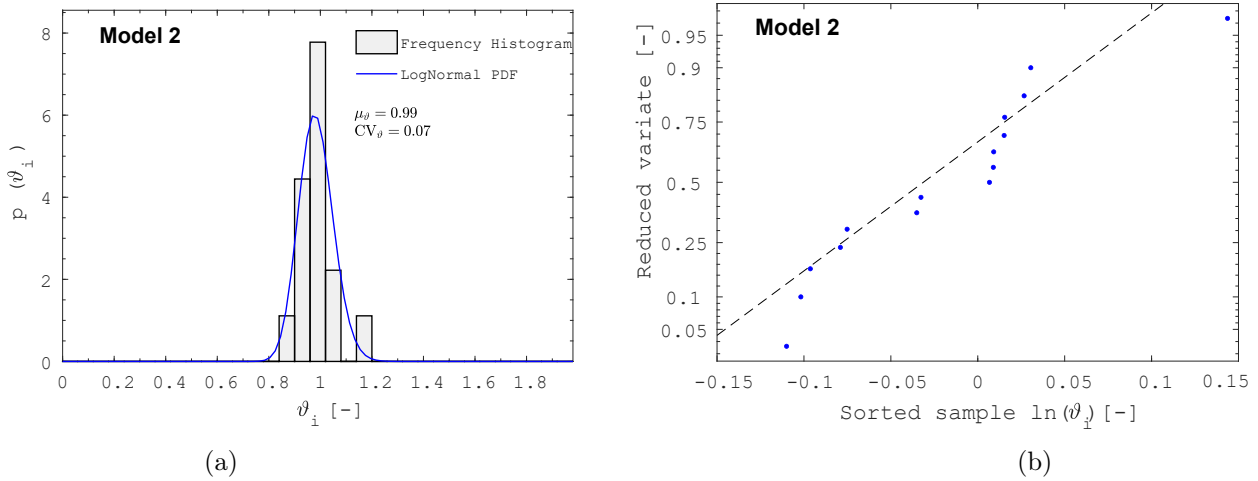


Figure 5.4: (a) Frequency Histogram vs. Lognormal PDF of θ for prior information in Model 2, and (b) Probability Plot of θ for prior information in Model 2

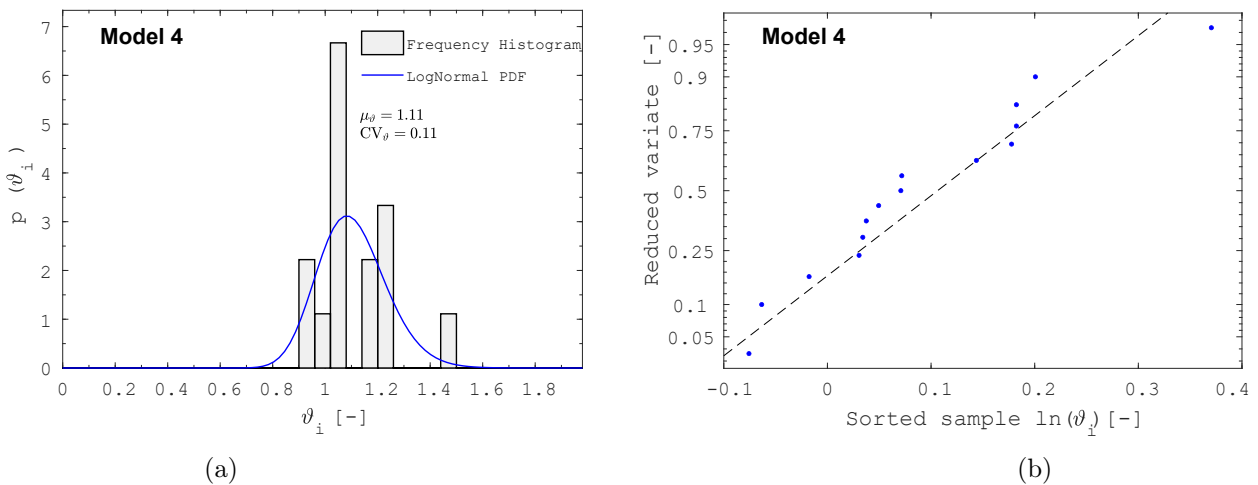


Figure 5.5: (a) Frequency Histogram vs. Lognormal PDF of θ for prior information in Model 4, and (b) Probability Plot of θ for prior information in Model 4

Chi-Squared (Pearson) Test

This test is based on subdividing the sample into k classes, with the optimal number of classes rounded to the closest integer [35]:

$$k = 2 \cdot n^{0.4} \quad (5.6)$$

To proceed with the test, the classes need to be defined. Equiprobable classes are used, where E_i is the expected frequency in the i -th class and q_i is the probability associated with the i -th class:

$$E_i = n \cdot q_i \quad (5.7)$$

$$q_i = \frac{1}{k} \quad (5.8)$$

After determining the expected frequencies, E_i , when H_0 is true and the number of sample elements falling into the i -th class (O_i), the weighted sum (X^2) can be estimated with the following formula:

$$X^2 = \sum_{i=1}^k \frac{(O_i - E_i)^2}{E_i} \quad (5.9)$$

X^2 follows a χ^2 distribution, which is a sum of squares of a normal variable. The degrees of freedom of the test are represented by the distribution parameter $k - np - 1$, where np is the number of estimated parameters. To evaluate the acceptance of the hypothesis, it is necessary to identify the limit of acceptance:

$$\chi_{\text{lim}}^2 = \chi^2(k - np - 1, \alpha) \quad (5.10)$$

with the level of significance (α), which quantifies the probability of rejecting a true hypothesis, set at 5%.

After identifying it:

- if $\chi^2 \leq \chi_{\text{lim}}^2$, we accept the hypothesis H_0 that the sample is drawn from the distribution, and the distribution is suitable to describe the sample.
- otherwise, we reject the hypothesis H_0 , and the distribution is not suitable to describe the sample.

Passing this type of test is relatively straightforward, and multiple distributions can pass it for the same sample; hence, additional tests are necessary, such as the Anderson-Darling, Jarque-Bera test, and Lilliefors test.

Anderson-Darling Test

Based on the cumulative distribution function, the Anderson-Darling test is applied to distributions that pass the Chi-Squared test to analyze the distance between the curves further. Unlike the Chi-Squared test, it is not subdivided into classes to avoid the loss of information [35]. The test statistic is defined as:

$$A^2 = n \int_{-\infty}^{\infty} \frac{[P(x) - F(x)]^2}{P(x) \cdot [1 - P(x)]} \cdot p(x) dx \quad (5.11)$$

This integral is numerically approximated by substituting the plotting position for the frequency F in the analytical expression:

$$A^2 = -n - \frac{1}{n} \sum_{i=1}^n \left\{ (2i - 1) \cdot \ln[P(x_{(i)})] + (2n + 1 - 2i) \cdot \ln[1 - P(x_{(i)})] \right\} \quad (5.12)$$

Where:

- $x_{(i)}$ are the elements of the sorted sample in increasing order.
- $P(x_{(i)})$ is the cumulative probability at $x_{(i)}$ from the distribution being tested.

To accept the hypothesis H_0 , it is necessary to compare the test statistic A^2 with a critical value A_{lim}^2 , which can be found in statistical tables because it depends on the distribution. Otherwise, the calculation of the variable ω , whose limit depends only on the level of significance, can provide further insight into the test results.

Jarque-Bera Test

The Jarque-Bera test evaluates whether sample data exhibit skewness and kurtosis similar to a normal distribution. To conduct this test, it is necessary first to transform the data into the logarithm of the θ values. From these converted numbers it's possible to compute the third standardized moment (skewness) and the fourth standardized moment (kurtosis) using the following formulas:

$$\gamma_1 = \frac{\frac{1}{n} \sum_{i=1}^n (X_i - \bar{X})^3}{\left(\frac{1}{n} \sum_{i=1}^n (X_i - \bar{X})^2 \right)^{3/2}} \quad (5.13)$$

$$\gamma_2 = \frac{\frac{1}{n} \sum_{i=1}^n (X_i - \bar{X})^4}{\left(\frac{1}{n} \sum_{i=1}^n (X_i - \bar{X})^2 \right)^2} - 3 \quad (5.14)$$

Where:

- X_i are the sample data points
- \bar{X} is the sample mean
- n is the sample size

These standardized moments are dimensionless measures that enable assessment of the Jarque-Bera statistic value JB as:

$$JB = \frac{n}{6} \left(\gamma_1^2 + \frac{1}{4} \gamma_2^2 \right) \quad (5.15)$$

Comparing it to a critical value JB_{lim} :

$$JB_{\text{lim}} = \chi^2(2, \alpha) \quad (5.16)$$

The value approximately follows a chi-squared distribution with 2 degrees of freedom and fixing a significance level of 5%, 2 scenarios can occur:

- If $JB \leq JB_{\text{lim}}$, accept the null hypothesis H_0 that the data are normally distributed.
- If $JB > JB_{\text{lim}}$, reject H_0 and conclude that the data are not normally distributed.

Lilliefors Test

The Lilliefors test is a goodness-of-fit test based on subdividing the sample into classes, similar to the Chi-squared test. However, in this case, the comparison between the observed frequencies O_i with the expected frequencies E_i is conducted using the Kolmogorov-Smirnov (KS) test statistic:

$$D = \max_i \left| F_n(X_{(i)}) - \frac{i}{n} \right| \quad (5.17)$$

Where:

- $F_n(X_{(i)})$ is the Empirical Cumulative Distribution Function (ECDF) of the sample
- $X_{(i)}$ is the i -th ordered observation in the sample
- $\frac{i}{n}$ is the expected cumulative probability

The critical value of the test D_{lim} is determined from tables of the Lilliefors distribution and it is associated with different sample sizes and significance levels (always assumed equal to 5%). In line with all the previous tests, the scenarios can be:

- if D exceeds the critical value, the hypothesis H_0 that the sample follows the hypothesized distribution is rejected
- if D is less than or equal to the critical value, H_0 is accepted and according to the test the sample is drawn by the tested distribution.

The analysis of the prior information involves these four statistical tests, applying them separately to each structural model and collectively to all models combined. The probability distribution has to pass all tests in sequence, starting from the least to the most restrictive. Additionally, the tests were repeated on posterior information using Bayesian updating, as detailed in the following subsection. Similarly to the case explained earlier of possible misalignment in the probability plot, if no distribution passes all the tests, the analyst should first try to change the parameter estimation method (i.e. moments, L-moments, Maximum Likelihood methods). If also after this adjustment, there is no distribution accepted by all, the entire statistical inference procedure must be restarted [35].

Fortunately, all the tests have been successfully passed as shown in table 5.2, and the p-value, for each case, has been estimated. This latter is a standardized measure that indicates the probability that the observed data would occur if the null hypothesis H_0 were true, quantifying how well the sample fits the chosen distribution. In a certain way, it complements the level of significance α : while α is chosen by the analyst before conducting the tests to set a threshold for the maximum acceptable probability of incorrectly rejecting the null hypothesis, the p-value is derived from the test results and is strongly influenced by the assumptions made previously. It quantifies the strength of the evidence against H_0 .

In practical terms, if the p-value is less than or equal to the chosen α level, for this analysis assumed equal to 0.05, it indicates that the sample offers sufficient information to reject the hypothesis whereby it has been drawn from a log-normal distribution. It's important to emphasize this last concept: it doesn't mean that the H_0 hypothesis is not necessarily true, rather, it indicates only that there is not sufficient information to accept

it, not allowing the procedure to proceed forward. On the other hand, if the p-value is greater than the α level, there is not enough information to reject the null hypothesis. As shown in Table 5.2, the p-value for each model is always greater than the α . This aligns with the literature, as reported in reference [11], which indicates that a log-normal probabilistic distribution can effectively capture the statistical variability of the realizations of the variable θ . Following the procedure suggested in Reference [11], when prior information already exists but needs to be updated with new information to strengthen the model, a Bayesian updating approach can be implemented. The method yields to the analyst the average distribution of θ and its statistical parameters like mean value μ_θ and standard deviation σ_θ . After that, the model uncertainty safety factor γ_{Rd} can be determined [7].

Models	Name Tests			
	Chi-Squared	Anderson-Darling	Jarque-Bera	Lilliefors
M1	Passed	Passed	Passed	Passed
P-value	0.243	0.348	0.148	0.340
M2	Passed	Passed	Passed	Passed
P-value	0.214	0.192	0.500	0.270
M3	Passed	Passed	Passed	Passed
P-value	0.084	0.608	0.230	0.500
M4	Passed	Passed	Passed	Passed
P-value	0.151	0.365	0.330	0.267
M5	Passed	Passed	Passed	Passed
P-value	0.645	0.540	0.505	0.500
M6	Passed	Passed	Passed	Passed
P-value	0.050	0.052	0.051	0.090
Mtot	Passed	Passed	Passed	Passed
P-value	0.057	0.098	0.364	0.055

Table 5.2: Test results

5.1.4 Calibration of model uncertainty safety factor

Bayes approach A

The Bayesian approach offers the analyst a comprehensive and robust probabilistic understanding of the random variable θ , as mentioned previously [7]. It involves several steps, each of which is strongly dependent on the previous one. Indeed, the idea behind the process is to evaluate the probability of A occurring, given that event B has been observed, as described by Engen et al. [43].

Initially, 6 log-normal probability distributions are defined, each corresponding to a different model hypothesis, denoted as $F(\theta | M_j)$ for $j = 1, \dots, 6$. All these models are assumed equally probable, meaning that there is not a favorite single model over another. The second step involves the assessment of the updating information: for each model M_j , it is derived from the data of all other models, excluding M_j itself. This is achieved using the average statistical parameters, grouped in vector z_j , from the probabilistic distributions of the other models through a leave-one-out approach. This method,

by enlarging the data sample from which information is drawn, enhances the robustness of the M_j models by validating them against external data. The result is a probability function $F_{M_j}(\theta | z_j)$ for $j = 1, \dots, 6$, each representing the updating information for the corresponding M_j model. The parameters of the lognormal distributions for the prior distributions and the new information were assessed using the maximum likelihood method, ML, thereby representing the maximum likelihood estimators, MLEs.

The Bayesian updating process leads, therefore, to the definition of a posterior log-normal probability function $F(\theta | M_j, z_j)$, which reflects both the prior information and the new data. On the other hand, its parameters were obtained in closed form using a preliminary joint distribution of the same form as the likelihood. This is called a conjugate prior distribution [16]. A new vector Z was defined, which collects the key statistical characteristics from the six posterior models, such as mean value and standard deviation. It allows the analyst to finally estimate the average log-normal posterior probability distribution $F(\theta | Z)$ that is adopted to represent the resistance modeling uncertainty random variable θ .

Indeed, by averaging the parameters of the posterior log-normal distributions, the parameters of the final distribution $F(\theta | Z)$ are derived:

$$\mu_{\text{LN,POST}} = \frac{1}{6} \sum_{i=1}^6 \mu_{\text{LN,post},i} \quad (5.18)$$

$$\sigma_{\text{LN,POST}} = \frac{1}{6} \sum_{i=1}^6 \sigma_{\text{LN,post},i} \quad (5.19)$$

Table 5.3: Statistical parameters of the prior information distribution functions and statistical uncertainty

Models	Prior distributions $F(\vartheta M_j)$			Statistical uncertainty	
	μ_ϑ [-]	σ_ϑ [-]	CV_ϑ [-]	$C(1,1)$	$C(2,2)$
1	0.99	0.06	0.07	2.8E-04	5.6E-04
2	0.99	0.07	0.07	3.1E-04	6.2E-04
3	0.87	0.07	0.08	4.3E-04	8.7E-04
4	1.11	0.13	0.11	9.2E-04	1.8E-03
5	1.02	0.09	0.08	4.6E-04	9.2E-04
6	0.88	0.10	0.11	7.8E-04	1.6E-03

Tables 5.3, 5.4, and 5.5 summarize the information and respectively present the prior, updating, and posterior statistical parameters of the related probabilistic distributions. Generally, the posterior mean values tend to fall between the prior and updating values, demonstrating the Bayesian updating approach's ability to merge prior and new information. As a rule of thumb, prior values tend to be more dispersed, with mean values ranging from 0.87 to 1.11. In contrast, the posterior distributions are more concentrated, with mean values ranging from 0.93 to 1.02. The lower σ_θ in the posterior log-normal distributions indicate a significant reduction in uncertainty compared to the updating information. The posterior coefficients of variation tend to be slightly higher than the prior ones but lower than the updating values, indicating a balanced integration of uncertainty. Looking at the results, one can question the need to apply the Bayesian method, given that the posterior CV theta is slightly higher than the prior ones. However, this is not the

Table 5.4: Statistical parameters of the updating information distribution functions and statistical uncertainty

Models	Updating information $F_{M_j}(\theta z_j)$			Statistical uncertainty	
	μ_ϑ [-]	σ_ϑ [-]	CV_ϑ [-]	$C(1,1)$	$C(2,2)$
1	0.97	0.13	0.13	2.2E-04	4.4E-04
2	0.97	0.13	0.13	2.2E-04	4.4E-04
3	1.00	0.11	0.12	1.8E-04	3.5E-04
4	0.95	0.10	0.11	1.5E-04	2.9E-04
5	0.97	0.12	0.12	2.1E-04	4.1E-04
6	1.00	0.11	0.11	1.7E-04	3.4E-04

Table 5.5: Statistical parameters of the posterior information distribution functions and statistical uncertainty

Models	Posterior distributions $F(\vartheta M_j, z_j)$			Statistical uncertainty	
	μ_ϑ [-]	σ_ϑ [-]	CV_ϑ [-]	$C(1,1)$	$C(2,2)$
1	0.98	0.10	0.10	1.1E-05	2.4E-06
2	0.98	0.10	0.10	1.1E-05	2.4E-06
3	0.93	0.11	0.12	1.4E-05	4.4E-06
4	1.02	0.14	0.13	1.8E-05	7.0E-06
5	1.00	0.11	0.11	1.2E-05	3.2E-06
6	0.94	0.12	0.13	1.6E-05	5.4E-06

primary goal of the approach: going from a data sample of 15 elements for each model to 75 strengthens the reliability and accuracy of the model even if the results may appear less precise. The values $C(1,1)$ and $C(2,2)$, derived from the inverse of Fischer’s matrix C , represent the variance of the statistical parameters μ_θ and σ_θ , respectively. The tables 5.3, 5.4, and 5.5 clearly show that the posterior values are generally smaller than both the prior and updating values, demonstrating that the Bayesian updating method enhances the precision and confidence in set estimates. They clearly show the power of this approach, which can seamlessly integrate diverse sources of information.

It is noteworthy that both software A and software B have effectively captured the real behavior of the beams: the posterior mean is very close to unity, indicating a nearly perfect correspondence between R_{exp} and R_{nlfea} . The low CV_θ also signifies minimal data dispersion, even though the posterior analysis incorporates significantly more data than the prior step. However, software A demonstrates lower standard deviations and mean values closer to 1, with consequently lower coefficients of variation, indicating more precise estimates. The lower accuracy in software B’s results is emphasized by the statistical uncertainty values, $C(1,1)$ and $C(2,2)$ which in a few cases are nearly an order of magnitude greater than those obtained by software A. The observed differences between the two software programs may likely be attributed to the numerical methods and algorithms used by software A, which may be better suited to the specific characteristics of the beams being analyzed. Additionally, the choices adopted for the mesh, including the dimensions and shapes of the elements, play a crucial role in the modeling phase. Software A uses advanced material models and meshing techniques, incorporating three types of meshes with three types of finite elements, contributing to its more accurate and

Table 5.6: Average statistical parameters $F_Z(\theta |)$

	Posterior distribution $F_Z(\theta Z)$	
	μ_θ [-]	CV_θ [-]
Average statistical parameters	0.98	0.12

consistent results.

The prior distribution for model 1 has a mean value μ_θ lower than unity, indicating an unsafe bias. The NLFEA overestimates the global structural resistance, even when considering tensile concrete behavior as elastic-brittle. Conversely, for model 4, despite the mean being even farther from 1 and the CV_θ being larger, it causes less risk. This is because software B underestimates the beam's resistance, thereby providing engineers with a safe margin. Regarding model 1, the updating information does not correct this bias, which has a mean value even farther from 1, resulting in a posterior distribution mean equal to 0.98. In contrast, models 4 and 6, assuming elastic-brittle and elastic-perfectly plastic behavior for concrete tension respectively, behave as expected. They underestimate global resistance in prior information since concrete contributes to tensile resistance, making post-peak behavior not entirely brittle. However, concrete is never completely elastoplastic, and thus, this tension-softening assumption tends to overestimate beam performance in the NLNA. The Bayesian method balances these initial biases, resulting in posterior mean values much closer to unity. Like the results obtained with model 6, in case 3 where the prior value was much lower than 1, 0.87, the entire process led to an unsafe bias reduction, bringing it up to 0.93.

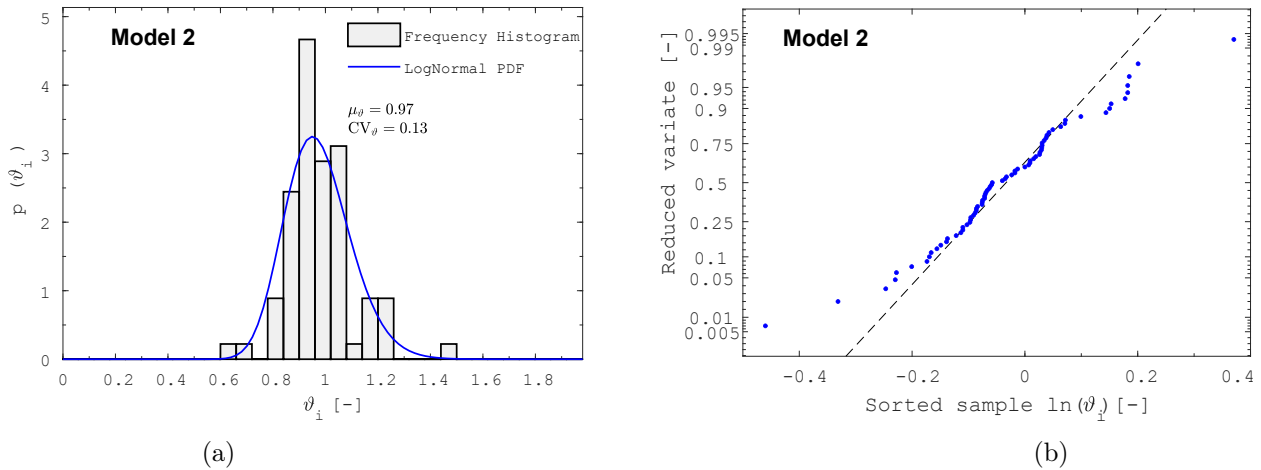


Figure 5.6: (a) Frequency Histogram vs. Lognormal PDF of θ for updating information in Model 2, and (b) Probability Plot of θ for updating information in Model 2

As demonstrated by the PDF and CDF of Models 2 and 4 in images 5.6 and 5.7, the log-normal distribution fits the larger samples of the updating information quite well. This is particularly evident in images 5.6b and 5.7b, where most points align closely with the line, except for a few outliers. These misaligned values may be attributed to the limited amount of prior data, which complicates the fitting process and can create a cascade effect, resulting in outliers in subsequent steps. This effect may diminish with a larger initial dataset or by incorporating prior information from literature sources, as demonstrated in the following subsection using Approach B.

The entire process, from the initial prior probability distributions to the updating and

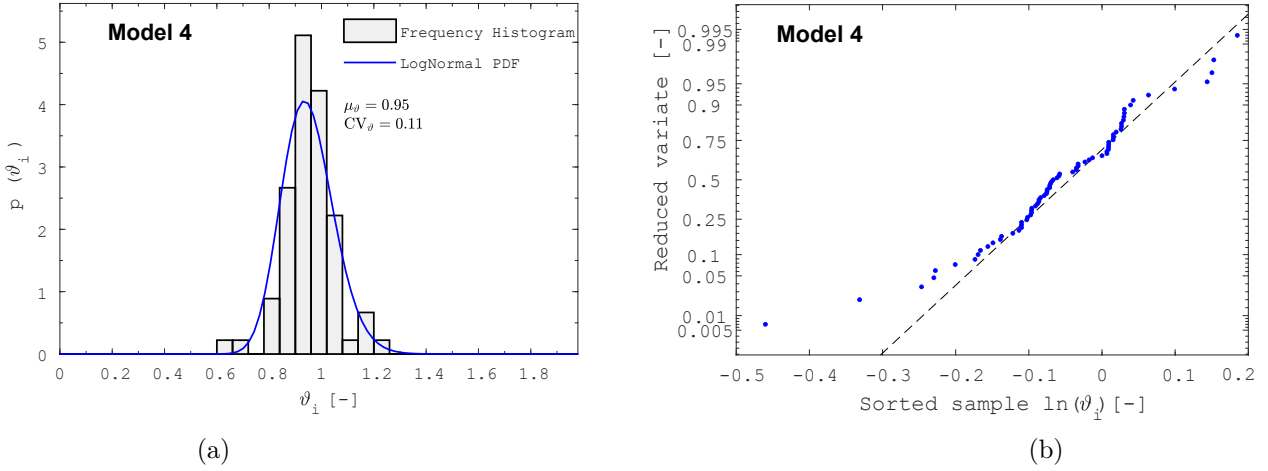


Figure 5.7: (a) Frequency Histogram vs. Lognormal PDF of θ for updating information in Model 4, and (b) Probability Plot of θ for updating information in Model 4

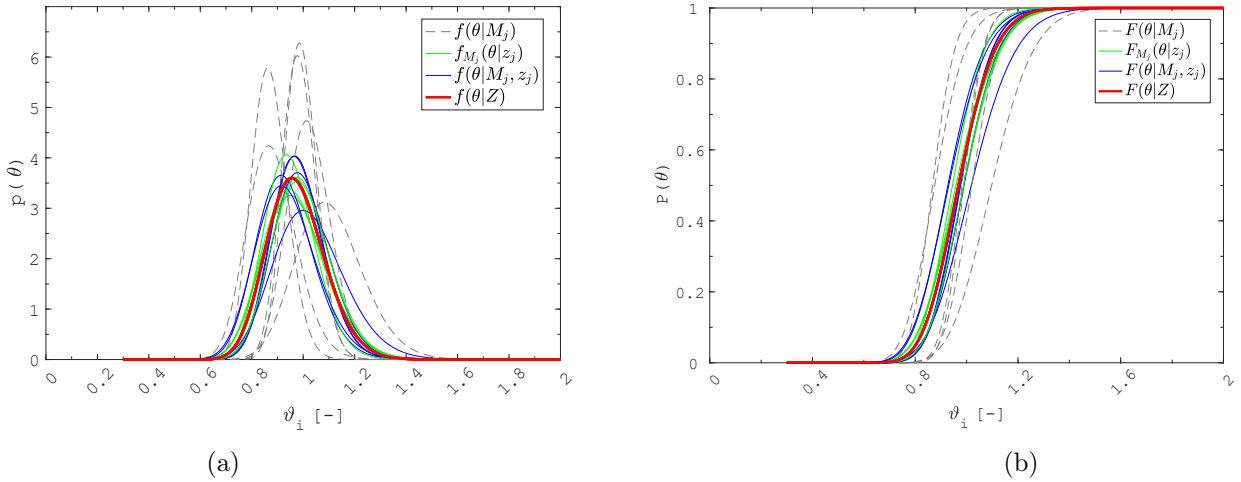


Figure 5.8: Probabilistic distributions related to prior, posterior, and updating information: Probability Density Functions (PDFs) (a) and Cumulative Distribution Functions (CDFs) (b)

posterior distributions, is illustrated in figure 5.8. These figures highlight the final log-normal probability distribution in red and table 5.12 its key statistical parameters. These values will be used in the next section to assess the model uncertainty safety factor γ_{Rd} . The posterior distributions, illustrated in blue in charts 5.8, fall between the more dispersed prior distributions (shown in gray) and the concentrated updating distributions (depicted in green). This behavior was predictable, as the posterior distributions are essentially the weighted average of the prior information and the new data.

The log-normal distribution is the most suitable probabilistic model to represent the θ sample, with a mean, μ_θ , of 0.98 and a coefficient of variation, CV_θ , of 0.12, as shown in table 5.12. These values will be used to calibrate the resistance model uncertainty safety factor γ_{Rd} in the next section. But before using them, as explained later, the results obtained at the end of the Bayesian approach must be purified by the effect of the experimental uncertainty. The mean value below 1 indicates that the nonlinear finite element analyses (NLFEAs) tend to slightly overestimate the beam's resistance. The low CV_θ signifies that the data points are closely clustered around this mean value. However, using these tools does not necessarily imply a risk of overestimating the performance of structural elements. This is because certain positive effects, such as confinement, are

completely neglected in the analysis.

Bayes approach B

To create a more comprehensive assessment of the random variable θ , 2 ways can be implemented:

- Expand the prior information
- Incorporate results from existing scientific literature

Regarding the first approach, it would take a considerable amount of time and be less general. It would encompass a larger sample but all of them would be modeled by the same analyst, with consistent choices and therefore, limiting the diversity that can be generated by different approaches. The aim of this work is not to create a procedure, and results specifically tailored to these selected beams, but rather to develop a universal method completely unrelated to the original sample, that can be always used within the sphere of beams subjected to flexural failure. This approach broadens the initial sample size and enhances the degree of confidence in the prior information. Known as Approach B, this methodology is like the previous Approach A but includes the Bayesian updating process based on the information assessed in the reference [15]. Table 5.7 summarizes all key properties, drawn from the reference. In A. de Putter's thesis, 101 beams were analyzed, and approximately 2000 nonlinear finite element analyses were conducted to determine the sensitivity of nonlinear models to specific aspects of solution strategies.

Table 5.7: Statistical parameters

	F9 - (101 Beams)	
	μ_{ϑ} [-]	CV_{ϑ} [-]
Statistical parameters	1.075	0.098

While the prior information remains the same as previously used, this approach differs in the initial step of updating information. Instead of using the average statistical parameters from the probabilistic distributions of the other models through a leave-one-out approach, here, all six modeling hypotheses M_j have been updated using a unique log-normal probabilistic distribution $F'(\vartheta)$, which has the key statistical parameters presented in table 5.7, according to [15]. In this way, the 6 initial phase-conditional posterior log-normal distributions $F'(\vartheta_j|M_j)$ are evaluated using the updating procedure outlined in the previous subsection. They are derived from a combination between the conjugate prior distributions with the new information, as summarized in tables 5.3, 5.8, and 5.9.

During the initial phase, the update shifts the mean values closer to 1, thereby reducing potential unsafe bias and uncertainty. This is evidenced by the lower values of $C(1,1)$ and $C(2,2)$ in the probability distributions $F'(\vartheta_j|M_j)$. The rightward shift of the curves with the increase in mean values is clearly shown in graph 5.9, where the prior, A. de Putter, and updating PDFs and CDFs are plotted.

In the second phase, the entire process mirrors the one applied in Approach A. However, instead of the initial prior information, it uses the updated results from the end of the previous phase, $F'(\vartheta_j|M_j)$, as the new prior information. Tables 5.10 and 5.11 summarize the results obtained from Approach B.

Table 5.8: Statistical parameter of the updating information distribution function and statistical uncertainty in the First Phase

Models	Updating information $F'(\theta)$			Statistical uncertainty	
	μ_{ϑ} [-]	σ_{ϑ} [-]	CV_{ϑ} [-]	$C(1,1)$	$C(2,2)$
1	1.075	0.10	0.097	-	-
2	1.075	0.10	0.097	-	-
3	1.075	0.10	0.097	-	-
4	1.075	0.10	0.097	-	-
5	1.075	0.10	0.097	-	-
6	1.075	0.10	0.097	-	-

Table 5.9: Statistical parameters of the posterior information distribution functions and statistical uncertainty in the First Phase and statistical parameters of the updated prior information distribution functions and statistical uncertainty in the Second Phase

Models	Posterior distributions $F'(\vartheta M_j)$			Statistical uncertainty	
	μ_{ϑ} [-]	σ_{ϑ} [-]	CV_{ϑ} [-]	$C(1,1)$	$C(2,2)$
1	1.06	0.10	0.10	8.2E-05	1.6E-04
2	1.06	0.10	0.10	8.4E-05	1.7E-04
3	1.01	0.12	0.12	1.2E-04	3.6E-04
4	1.08	0.11	0.10	8.7E-05	1.8E-04
5	1.06	0.10	0.10	8.1E-05	1.6E-04
6	1.00	0.12	0.12	1.2E-04	3.7E-04

As shown in the tables, in the second phase the updating information is almost identical to that of the previous approach. However, the posterior distributions have changed significantly. For instance, models 3, 4, and 6 initially have mean values quite far from unity. During the second phase, the Bayesian method improves the precision of the data, bringing the mean values closer to 1, reaching 1.01, 1.06, and 1.00, respectively. This is reflected in the average posterior log-normal distribution, which has a mean value of 1.04 and a coefficient of variation of 0.11. Compared to Approach A, this method eliminates unsafe bias, achieving a good correspondence between the R_{exp} and $R_{\text{nlнас}}$. Even if the mean value is not exactly 1, the analysis falls into the safe region. Regarding the CV θ , it is slightly lower, decreasing from 0.12 to 0.11, but in both cases it remains relatively low. Similarly to Approach A, also in this case before using these results, they must be purified by the effect of the experimental uncertainty. These results are fully consistent with AdePutter’s thesis, which also examines the impact of the constitutive model, specifically regarding crack orientation. As illustrated in image 5.10, A. de Putter’s probability model exhibits a safer bias, demonstrated by the rightward shift of the PDF. This contributes to the increased robustness and reliability of our model, especially given the larger number of RC beams analyzed. Examining the graphs, it’s possible to observe that A. de Putter’s information heavily affects the mean values of the models, which is graphically expressed in a shift of the PDF curves. This is caused by the large number of prior information that he has, which during the Bayesian procedure weights much more than the 15 models of this thesis. This is exactly the aim of the approach B: to create a new sample, even larger than the original datasets, that can be exploited for further

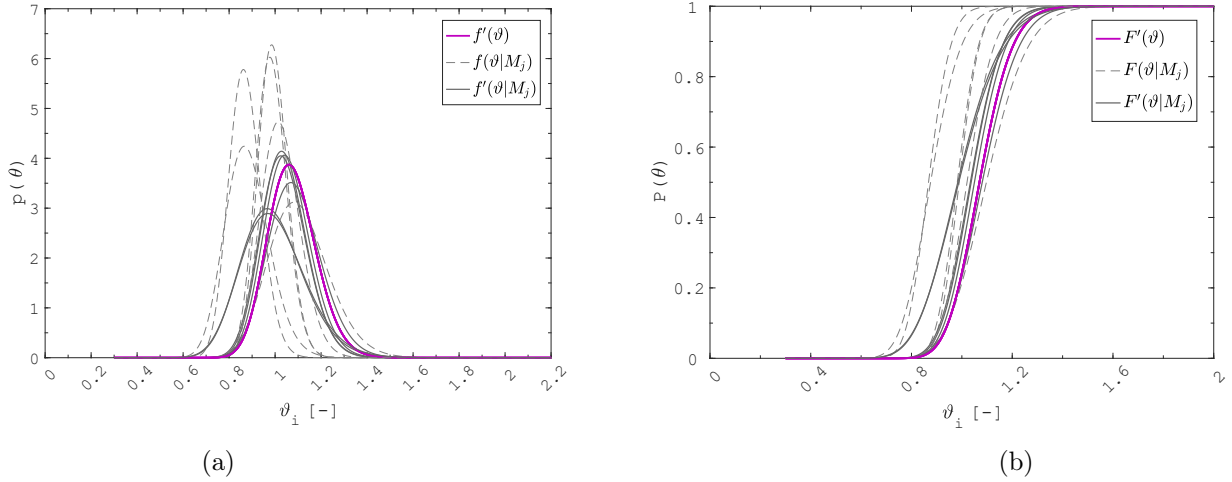


Figure 5.9: Probabilistic distributions related to prior, AdePutter's model, and posterior information: Probability Density Functions (PDFs) (a) and Cumulative Distribution Functions (CDFs) (b)

Table 5.10: Statistical parameters of the updating information distribution functions and statistical uncertainty in the Second Phase

Models	Updating information $F'_{M_j}(\theta z_j)$			Statistical uncertainty	
	μ_ϑ [-]	σ_ϑ [-]	CV_ϑ [-]	$C(1,1)$	$C(2,2)$
1	0.97	0.13	0.13	2.2E-04	4.4E-05
2	0.97	0.13	0.13	2.2E-04	4.4E-05
3	1.00	0.12	0.12	1.8E-04	3.5E-05
4	0.95	0.10	0.11	1.5E-04	2.9E-05
5	0.97	0.12	0.12	2.1E-04	4.1E-05
6	1.00	0.11	0.11	1.7E-04	3.4E-05

analysis. In this way, the procedure becomes increasingly reliable.

5.1.5 Influence of Experimental Uncertainty

The thesis aims to estimate and minimize the impact of model uncertainty, also known as epistemic uncertainty, in global resistance assessment. By exploring the effects of various modeling options that are available to engineers during the modeling phase, this work seeks to identify a partial safety factor. This value appears from the need to mitigate the effects of subjectivity in the modeling process. However, it is important to acknowledge that the starting data collected during several experiments are subject to uncertainties, including those arising from experimental inaccuracies [43].

One of the key positive aspects of approaching the analysis with the Global Resistance Format is the ability to study each type of uncertainty independently and refine the results only at the end deleting all of them through a specific safety factor. This is the case of the experimental uncertainty ε , which encompasses all uncertainties related to the test, such as procedural variations, accuracy of test methods and conduction, measurement errors, and geometrical deviations of the specimens. These factors may contribute to eccentricities in the applied loads and variations in the actual support configuration, collectively

Table 5.11: Statistical parameters of the posterior information distribution functions and statistical uncertainty in the Second Phase

Models	Posterior distributions $F'(\vartheta M_j, z_j)$			Statistical uncertainty	
	μ_ϑ [-]	σ_ϑ [-]	CV_ϑ [-]	$C(1,1)$	$C(2,2)$
1	1.05	0.11	0.10	8.4E-05	1.9E-06
2	1.05	0.12	0.11	8.5E-05	2.0E-06
3	1.01	0.12	0.12	1.2E-04	3.7E-06
4	1.06	0.11	0.11	9.1E-05	2.3E-06
5	1.04	0.10	0.10	8.4E-05	1.9E-0
6	1.00	0.12	0.12	1.2E-04	3.8E-06

 Table 5.12: Average statistical parameters $F_Z(\theta |)$

	Posterior distribution $F'_Z(\theta Z)$	
	μ_ϑ [-]	CV_ϑ [-]
Average statistical parameters	1.04	0.11

affecting the reliability of the test results. To accurately assess the impact of experimental uncertainty and evaluate the actual values of the resistance model uncertainty θ , it is essential to separate the experimental uncertainty component from the evaluated mean values μ_θ and the coefficient of variation CV_θ . If the experimental uncertainty ε follows a log-normal probability distribution with a mean value μ_ε , and a coefficient of variation CV_ε , the detachment of this component can be assessed. At the end of the process, the partial safety factor γ_{Rd} precisely reflects the model's intrinsic uncertainty, without being affected by any other components. It represents, therefore, a standardized way to present the outcomes, allowing a comparison with other results available in the literature. Even if it may seem obvious, one of the most common and easily overlooked mistakes that one can make is to compare similar results without acknowledging all the components that contributed to them. It would harm completely the work done experiments are subject to uncertainties, including those arising from experimental inaccuracies [43].

Regarding the mean of the experimental uncertainty, μ_ε , is assumed conventionally equal to 1.00: the actual mean value $\mu_{\theta,act}$ corresponds exactly with the one assessed through the process, μ_θ . Evaluating the coefficient of variation for ε , instead, is more challenging, and the literature suggests a likely range from 0.05 to 0.15 [43]. With both statistical metrics known, the resistance model uncertainty random variable θ can be decoupled from the influence of experimental uncertainty. The actual values of the key statistical metrics can then be determined using equations through the following equations:

$$\mu_{\vartheta,act} \approx \frac{\mu_\vartheta}{\mu_\varepsilon} \quad (5a)$$

$$CV_{\vartheta,act} \approx \sqrt{CV_\vartheta^2 - CV_\varepsilon^2} \quad (5b)$$

With μ_ε equal to 1, the μ_θ assessed during approaches A and B coincides with the actual μ_θ . Instead, to ensure precision, it is necessary to consider both extremes of the range for the coefficient of variation. For example, in Alberto Meda's study of 4-meter-long beams with a cross-section of just 200 x 300 mm, the influence of geometric imperfections, such as asymmetry in concrete properties due to imperfect casting procedures, misplacement

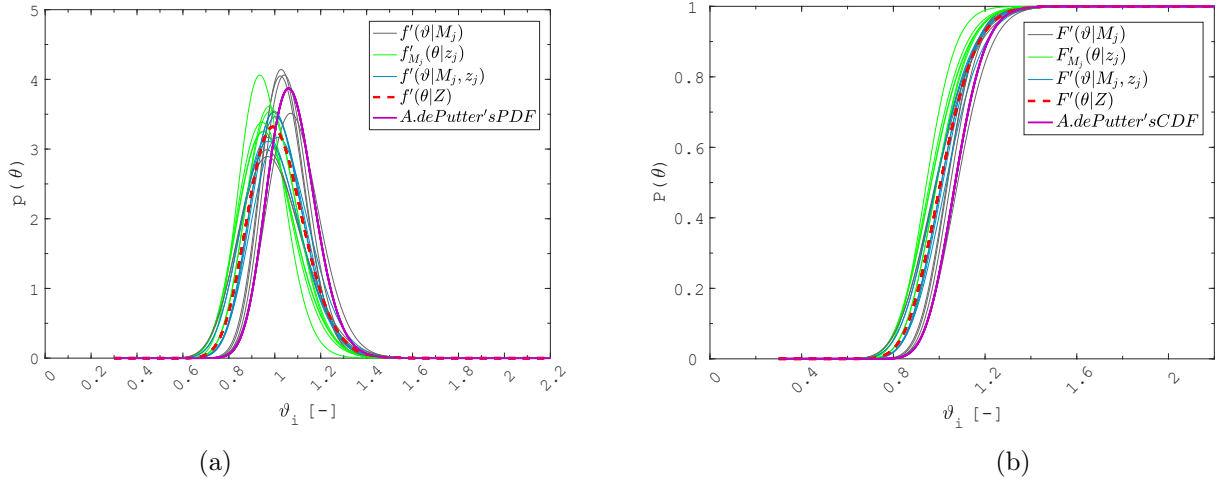


Figure 5.10: Probabilistic distributions related to updated prior, updating, posterior and averaged posterior information: Probability Density Functions (PDFs) (a) and Cumulative Distribution Functions (CDFs) (b)

of reinforcement and imperfections related to load application, can be significantly higher compared to beams with a lower a/d value, like those analyzed by Giuseppe Campione. The impact of a well-conduction of the experiment becomes even more significant when the ultimate load is low as in the case of Alberto Meda's study.

In this thesis, only the so-called limited experimental uncertainty has been considered, opting not to address scenarios with significant experimental uncertainty, where CV_ε is set equal to 0.10. This choice derives from the results obtained through the Bayesian process. Given that the CV theta is already low, giving a coefficient of variation of the experimental uncertainty too high wouldn't be coherent. This approach may lead to an underestimation of the actual uncertainty, making it incoherent with the modeling results. Moreover, the limited assumption aligns with the idea of taking the data from prestigious papers, where procedures are executed meticulously. This ensures complete confidence in the conduction of experiments. In any case, any uncertainty arising from the experimental procedure provides an additional safety margin, further reducing the CV_θ .

In the case of a limited experimental uncertainty, CV_ε is considered to be 0.05. Therefore, by applying equation 5b, the $CV_{\theta,act}$ becomes a bit lower than the observed one. This enables the analyst to completely neglect the influence of experimental uncertainty on both key parameters when it's much lower than the assessed values, as demonstrated in the case study [25]. This approach aligns with reference [24], which states that experimental uncertainty can be ignored when the observed coefficient of variation of the averaged posterior distributions, CV_θ , exceeds 0.10. This is because the variability from modeling assumptions and methodology is significantly greater than that from experimental errors. In such cases, modeling uncertainties dominate the overall uncertainty in the system, justifying the exclusion of other uncertainties. In our case, the CV_θ slightly exceeds this threshold, but since it's immediately above, it's still excluded from the observed values. Table 5.13 summarizes the key metrics for the log-normal probabilistic distributions obtained by applying the 2 approaches. These metrics represent the resistance model uncertainty random variable ϑ , not accounting for the influence of experimental uncertainty ε . These are the results that will be used in the next subsection to assess the partial safety factor for resistance model uncertainty.

Approach	Experimental uncertainty ε	Actual statistical parameters for resistance model uncertainty random variable ϑ	
		$\mu_{\vartheta,act}$	$CV_{\vartheta,act}$
A	Limited $V_\varepsilon \leq 0.05$	0.98	0.104
B	Limited $V_\varepsilon \leq 0.05$	1.04	0.098

Table 5.13: Actual statistical parameters for resistance model uncertainty random variable ϑ

5.1.6 Assessment of the partial safety factor for resistance model uncertainty

The value of the resistance model uncertainty partial safety factor, γ_{Rd} , for RC beams, is determined based on the target reliability index (β) set by design codes. This value varies depending on whether the analysis involves, as referenced in sources [7] and [25], existing or new structures. In the first case, it represents the design working life, in the latter instead the remaining working life. Design codes establish specific probabilities of failure that structures must not exceed to ensure they meet acceptable safety and performance standards. These probabilities are influenced by the consequences of potential failure, which include the impact on human life, economic losses, environmental damage, and the intended service life of the structure, as highlighted in sources [7] and [22].

Based on the results obtained in the previous section and summarized in table 5.13, γ_{Rd} can be evaluated using equation 5.2 by adopting different target reliability values. A crucial parameter in its evaluation process is the FORM sensitivity factor α_R , which measures the influence of the structure's resistance on the reliability index β . In this specific case, α_R is set to 0.32, as derived from Hasofer and Lind [1]. This value is chosen because modeling uncertainties are assumed to be non-dominant variables. They have less influence on the overall probability of failure compared to aleatory uncertainties, which are related to the random variability of material properties and actions. This non-dominant hypothesis is supported by a $CV_{\vartheta,act}$ value in both cases lower than the CV value of 0.15 associated with the upper limits in the aleatory uncertainties, as noted in [23]. This indicates that the overall uncertainty in global resistance is primarily influenced by aleatory uncertainties.

The choice of adopting fixed values for the FORM sensitivity factors, with α_R set at 0.8 for dominant variables and α'_R at 0.32 for non-dominant variables, is aimed at achieving an extra level of safety. However, this approach may not always be the optimal solution, particularly when economic considerations are extremely important in the design process. Engineers must always balance the need for safety with economic feasibility, ensuring that the design is both safe and cost-effective. The adoption of a too-conservative design approach might be the safest option but could be at the same time unfeasible because it's too expensive, on the other hand, economical designs might compromise safety [1].

The fib Model Code 2010 outlines three distinct approaches to determine the global safety factor, γ_{RGL} , and the procedure discussed previously is known as Approach 1. Approach 2, on the other hand, utilizes the same input data as Approach 1 but does not distinguish between dominant and non-dominant variables. Consequently, Approach 2 typically results in a global safety factor that is, on average, 2% higher than that obtained using

Approach 3. This comparison underscores that Approach 2 incorporates an additional safety margin compared to the purely probabilistic Approach 3. However, this margin is slightly less than the extra safety provided by Approach 1. These different approaches help engineers choose the appropriate level of safety and conservatism based on specific project requirements and constraints. For critical infrastructures, the probability of failure must be much lower, which implies the use of a more conservative design approach. This is reflected in the calculation using higher partial safety factors [1].

Tables 5.14 and 5.16 present the various values of γ_{Rd} applicable to different design scenarios under Approach A and Approach B, respectively. For a more detailed analysis, Tables 5.15 and 5.17 provide γ_{Rd} values based on the assumption that model uncertainties dominate over aleatory uncertainties, with a FORM sensitivity factor of 0.8. This assumption results in a 22% increase in γ_{Rd} for both new and existing structural systems: this approach would increase the amount of steel and/or concrete, leading to unbalancing the previously balanced trade-off between safety and economic feasibility. If the designer chooses to adopt this assumption, the partial factors for aleatory uncertainties related to material strengths (i.e., γ_c , and γ_s) would be significantly reduced.

As discussed in the previous section, A. de Putter's research has notably reduced uncertainty while enhancing both robustness and reliability. This progress is evident in the γ_{Rd} values, with Approach B yielding slightly lower values than Approach A. For new structural systems with moderate failure consequences, a 50-year design lifetime, and $\beta = 3.8$, γ_{Rd} values proposed are 1.16 for Approach A and 1.08 for Approach B. For existing structural systems, γ_{Rd} ranges from 1.14 to 1.16 for Approach A and from 1.06 to 1.08 for Approach B. As shown in the tables, the partial safety factor for existing structures is expressed as a range due to the inherent uncertainties and variabilities in assessing their reliability. For instance, evaluating the extent of degradation in a structure can be challenging. Aging, along with environmental factors such as corrosion, weathering, and mechanical components like fatigue, can cause significant variations in the condition of different parts of the structure.

A γ_{Rd} value of 1.08 for RC beams in NLNAs can be reputed as a satisfactory and consistent result, especially when comparing it with outcomes from other studies on RC structural elements, such as those in [25] and [16]. These values reflect a moderately conservative approach that effectively addresses model uncertainties, ensuring safety and reliability in the design process. However, the Bayesian method is based on a robust framework, and it gains strength and accuracy by gathering more and more literature data, particularly with Approach B. Therefore, these results should be viewed as a preliminary benchmark, and likely future analyses will further refine them.

Flow chart 5.11 provides a comprehensive overview of the process used to assess the model uncertainty factor γ_{Rd} , illustrating both approaches in a schematic format. To avoid redundancy in the use of images, this scheme will not attach in the subsequent subsection, even if it is still valid. The beams with a shear failure have been investigated, but only approach A will be implemented, due to the difficulty of finding in literature papers that analyze this kind of collapse. The only difference is the following:

- Experimental results: $i = 1 \dots 20$

Regarding the modeling hypotheses, there will always be 6, with $j = 1 \dots 6$.

Table 5.14: Partial safety factors γ_{Rd} for RC beams in the hypothesis of non-dominant resistance variable depending on the target reliability level - Approach A

New structures	Service life	Consequences of failure	Reliability index β	FORM factor	Partial safety factor
	[Years]	[-]	[-]	α_R [-]	γ_{Rd} [-]
	50	Low	3.1	Non-dominant 0.32	1.14
	50	Moderate	3.8	Non-dominant 0.32	1.16
	50	High	4.3	Non-dominant 0.32	1.18
Existing structures	Service life		Reliability index β	FORM factor	Partial safety factor
	[Years]		[-]	α_R [-]	γ_{Rd} [-]
	50		3.1–3.8	Non-dominant 0.32	1.14–1.16
	15		3.4–4.1	Non-dominant 0.32	1.15–1.18
	1		4.1–4.7	Non-dominant 0.32	1.18–1.20

Table 5.15: Partial safety factors γ_{Rd} for RC beams in the hypothesis of dominant resistance variable depending on the target reliability level - Approach A

New structures	Service life	Consequences of failure	Reliability index β	FORM factor	Partial safety factor
	[Years]	[-]	[-]	α_R [-]	γ_{Rd} [-]
	50	Low	3.1	Dominant 0.8	1.33
	50	Moderate	3.8	Dominant 0.8	1.41
	50	High	4.3	Dominant 0.8	1.47
Existing structures	Service life		Reliability index β	FORM factor	Partial safety factor
	[Years]		[-]	α_R [-]	γ_{Rd} [-]
	50		3.1–3.8	Dominant 0.8	1.33–1.41
	15		3.4–4.1	Dominant 0.8	1.36–1.44
	1		4.1–4.7	Dominant 0.8	1.44–1.52

Table 5.16: Partial safety factors γ_{Rd} for RC beams in the hypothesis of non-dominant resistance variable depending on the target reliability level - Approach B

New structures	Service life	Consequences of failure	Reliability index β	FORM factor	Partial safety factor
	[Years]	[-]	[-]	α_R [-]	γ_{Rd} [-]
	50	Low	3.1	Non-dominant 0.32	1.06
	50	Moderate	3.8	Non-dominant 0.32	1.08
	50	High	4.3	Non-dominant 0.32	1.10
Existing structures	Service life		Reliability index β	FORM factor	Partial safety factor
	[Years]		[-]	α_R [-]	γ_{Rd} [-]
	50		3.1–3.8	Non-dominant 0.32	1.06–1.08
	15		3.4–4.1	Non-dominant 0.32	1.07–1.09
	1		4.1–4.7	Non-dominant 0.32	1.09–1.11

Table 5.17: Partial safety factors γ_{Rd} for RC beams in the hypothesis of dominant resistance variable depending on the target reliability level - Approach B

New structures	Service life	Consequences of failure	Reliability index β	FORM factor	Partial safety factor
	[Years]	[-]	[-]	α_R [-]	γ_{Rd} [-]
	50	Low	3.1	Dominant 0.8	1.23
	50	Moderate	3.8	Dominant 0.8	1.30
	50	High	4.3	Dominant 0.8	1.35
Existing structures	Service life		Reliability index β	FORM factor	Partial safety factor
	[Years]		[-]	α_R [-]	γ_{Rd} [-]
	50		3.1–3.8	Dominant 0.8	1.23–1.30
	15		3.4–4.1	Dominant 0.8	1.26–1.33
	1		4.1–4.7	Dominant 0.8	1.33–1.39

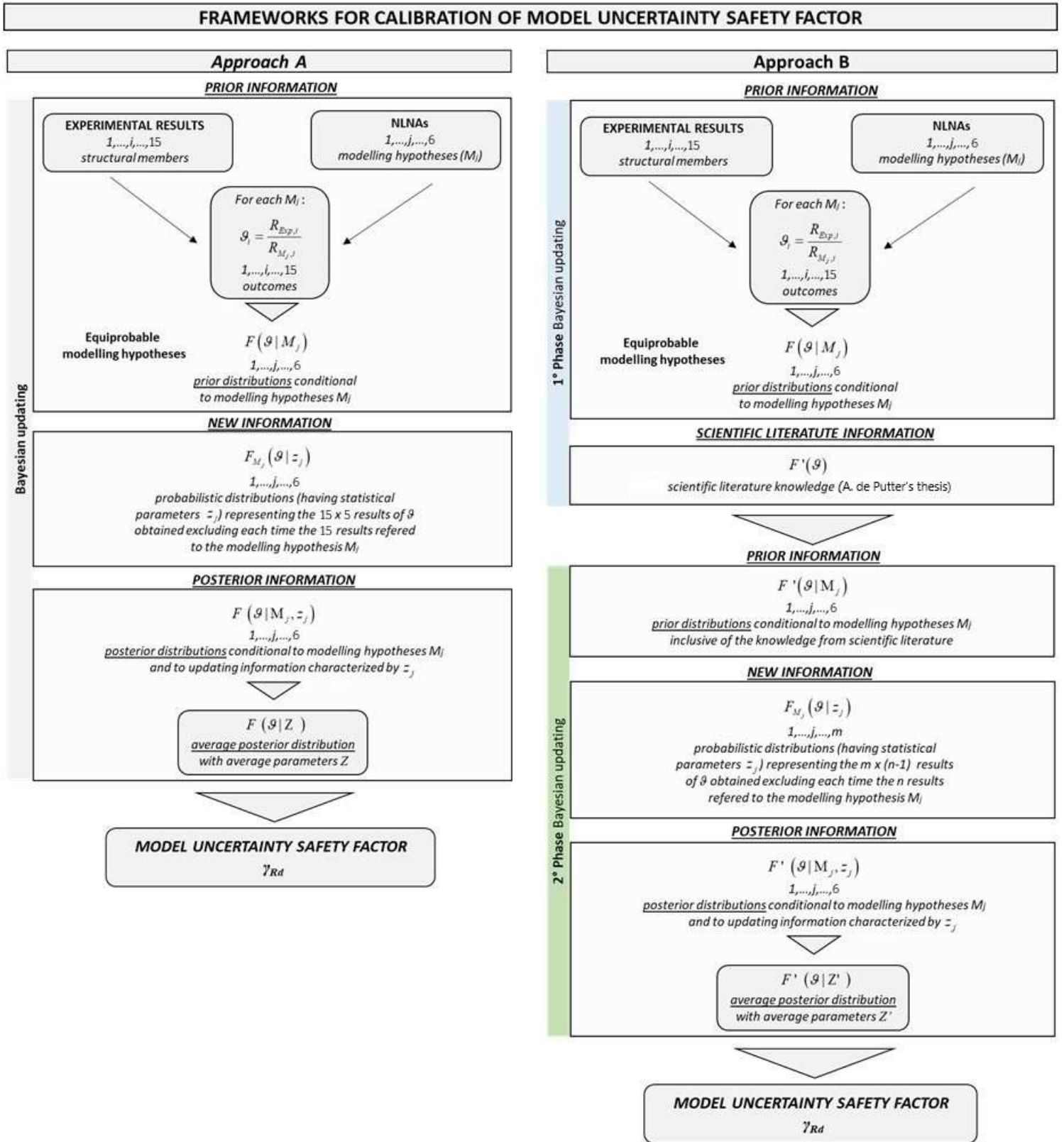


Figure 5.11: Flow-chart representing the Approach A and Approach B for the estimation of the model uncertainty safety factor [25]

5.2 Beams experiencing shear failure

In this case, 20 beams were analyzed, resulting in a [20 x 6] matrix, as presented in table 5.18.

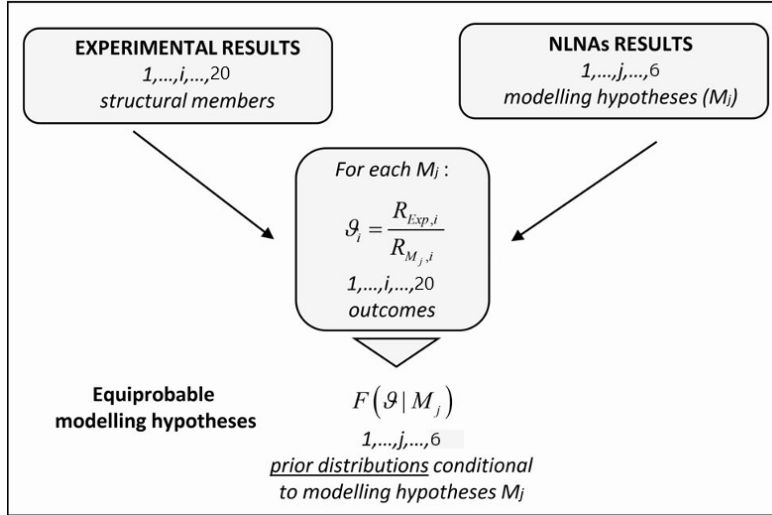


Figure 5.12: Prior information scheme

Table 5.18: Resistance model uncertainty random variables

Software	A			B		
	Brittle	LTS	Plastic	Brittle	LTS	Plastic
Model	1	2	3	4	5	6
S-0.157	0.933	0.933	0.814	1.671	1.554	1.214
S-0.314	0.942	0.942	0.899	1.283	1.236	0.932
S-0.628	0.956	0.956	0.909	1.337	1.228	1.165
S-0.942	0.981	0.981	0.938	1.444	1.135	1.036
B1S06	0.995	0.967	0.890	1.122	1.052	1.052
B1S10	1.144	1.113	1.113	1.172	1.065	1.099
B2S06	0.959	0.959	0.937	1.129	1.068	1.097
S06	1.100	1.100	0.931	1.367	1.228	1.330
S10	1.138	1.138	1.076	1.644	1.430	1.370
S8-90	1.044	1.044	0.922	1.294	1.121	0.908
F0S0	0.943	0.943	0.757	1.369	1.027	0.846
ST80	0.896	0.896	0.831	1.214	1.087	1.068
ST120	1.344	0.956	0.717	1.446	1.126	0.964
B44W2	1.092	1.076	1.000	1.420	1.420	1.543
B44W1.5	1.012	1.000	0.946	0.892	0.817	0.782
A01	0.795	0.795	0.685	1.099	1.099	0.957
A02	0.864	0.864	0.838	1.152	1.000	1.226
B02	0.940	0.940	0.940	1.214	1.101	1.127
RCTB-1	0.886	0.879	0.757	0.990	0.956	0.923
RCTB-3	0.983	0.950	0.792	1.118	1.096	1.075

Table 5.18 clearly shows that even in the case of beams that fail in a shear mode, the

theoretical extreme hypotheses about concrete’s tensile behavior are not sufficient to encompass the experimental peak load. In both software analyses, as predicted, θ is lower than 1 in the case of brittle behavior and it exceeds 1 in the plastic case. This is clear evidence of the ongoing challenge to capture with accuracy the shear failure mode, even having access to the most advanced NLNA tools. Especially software B struggles during the processing phase since the stirrups start playing a crucial role in the structural mechanism. The discrepancies discovered in the peak load estimation when comparing numerical simulation with experimental results underscore the difficulty in precisely predicting this complex behavior.

Compared to the flexural case, a possible explanation for the higher uncertainty in the outcomes could be the nature of the resistance mechanism. Indeed, it is not solely determined by the concrete properties or the reinforcement ones, but rather by the interaction and cooperation between these two materials. These numerous uncertainties may significantly affect the finite element models’ accuracy in replicating experimental behavior, and only an accurate post-processing investigation can reveal the reason behind an unsuccessful analysis.

Each time, especially in these types of analyses, the post-processing phase becomes the crucial part of the entire process because even the most precise modeling phase cannot always guarantee correct, or at least realistic, outcomes. To address this problem, four key characteristics have been considered when analyzing the results provided by the software:

- crack pattern development
- number of iterations per step
- strain in the reinforcement
- stress and strain distribution in the beam

Indeed, in some analyses, the last steps have been neglected because the provided results were not reliable, showing a high number of iterations, an unusual crack pattern, and an unlikely physical behavior. At this stage, software A helps the modeler because it displays the beam deformations and the crack development in real time during the analysis. This constant feedback makes it quite immediate to understand if the high number of iterations is a numerical issue or comes from the progressive opening of significant cracks. In table 5.18, most of the data values are farther from the unity compared to the previous case, indicating a larger uncertainty in the outcomes. This uncertainty may be compensated in terms of safety for the higher bias. This latter can become problematic not only when it arises from overestimation of the peak resistances but also when it leads to overly conservative and costly design decisions that may be inefficient and unsustainable. When comparing columns 2 and 4, which correspond to the LTS models obtained through a meticulous software calibration, it’s evident that software A captures more precisely than B the experimental results in terms of load. The same observations can be made for the other columns. By contrast, as shown by the θ values equal to 0.685 and 1.671 in the third and fourth models, respectively, even software A addresses some problems in replicating faithfully during the NLFEA the actual behavior of some RC structures. Moreover, it’s noteworthy that in both cases, most of the time, the properties with which the software performs better are the same, such as mesh dimensions and applied load for step. This consistency helps the analyst reduce the time needed to implement the same structure across different NLNA tools, facilitating the comparison of the different results and leading to a comprehensive post-processing phase.

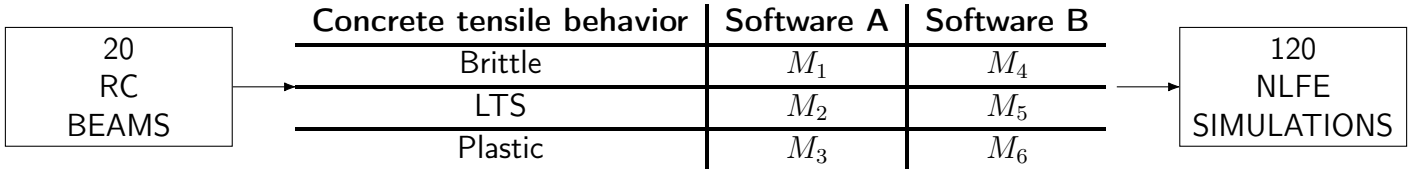
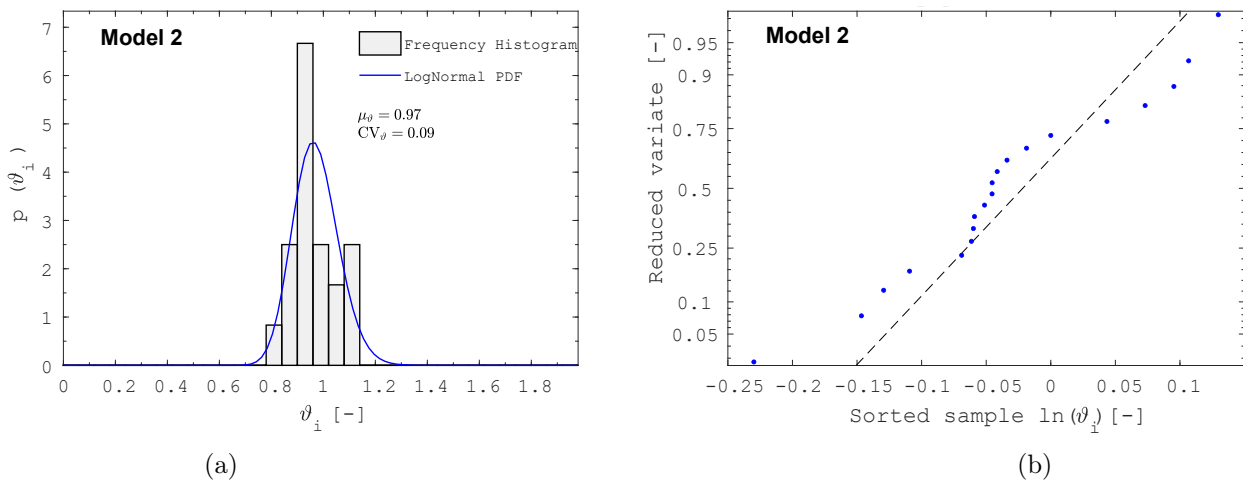


Figure 5.13: Modelling hypotheses and benchmark NLNAs

5.2.1 Statistic Inference

Also, in this case, the null hypothesis H_0 assumes that the sample is drawn from a log-normal distribution, according to the literature. The entire procedure regarding the statistical inference is the same as the flexural analysis, including all four sequential tests to prove that our sample, despite the uncertainty, fits well with the chosen probability distributions, avoiding making flimsy assumptions.

Before proceeding, the graphical check of the random variable θ , as shown in images 5.14 and 5.15, confirms that the log-normal distribution may provide an appropriate description of its variability, and it's worth moving forward with the optimization process. Figures 5.14a and 5.15a juxtapose the frequency histogram derived from the data with the log-normal probability density function. Meanwhile, the probability plots, in Figures 5.14b and 5.15b, confirm the alignment of points. In this case, the sample is even larger than in the flexural case; therefore, the good alignment of each point makes it an even more robust visual test to confirm the good choice of assuming this probability distribution. Similar behavior has been detected in the remaining modeling hypotheses, constituting the prior information. The consistency test was also implemented in line with the previous chapter: the six combined models were analyzed collectively, treating them as a unique sample of 120 random variables. Fortunately, all the tests have been passed, as shown in table 5.19, and the p -value has been evaluated for each case. To be consistent with the previous approach, the chosen α level for the analysis is assumed equal to 0.05, and as displayed in table 5.19, the p -value for all the models is greater than α , confirming that the models pass the statistical tests with an adequate margin of reliance.

Figure 5.14: (a) Frequency Histogram vs. Lognormal PDF of θ for prior information in Model 2, and (b) Probability Plot of θ for prior information in Model 2

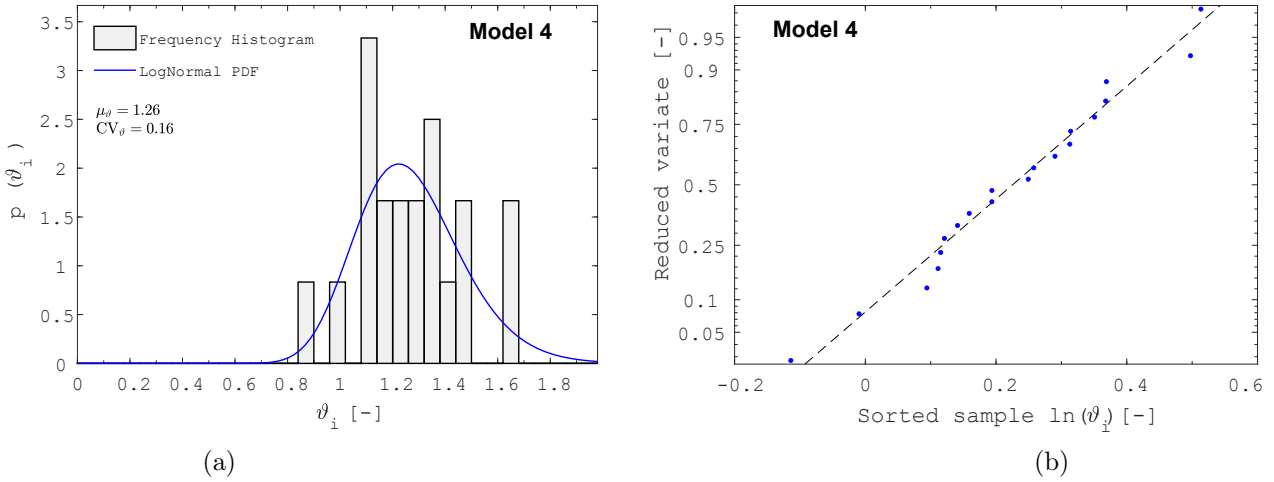


Figure 5.15: (a) Frequency Histogram vs. Lognormal PDF of θ for prior information in Model 4, and (b) Probability Plot of θ for prior information in Model 4

Models	Name Tests			
	Chi-Squared	Anderson-Darling	Jarque-Bera	Lilliefors
M1	Passed	Passed	Passed	Passed
P-value	0.223	0.320	0.107	0.302
M2	Passed	Passed	Passed	Passed
P-value	0.265	0.270	0.500	0.314
M3	Passed	Passed	Passed	Passed
P-value	0.185	0.482	0.500	0.291
M4	Passed	Passed	Passed	Passed
P-value	0.083	0.925	0.500	0.500
M5	Passed	Passed	Passed	Passed
P-value	0.348	0.086	0.500	0.059
M6	Passed	Passed	Passed	Passed
P-value	0.061	0.965	0.500	0.500
Mtot	Passed	Passed	Passed	Passed
P-value	0.258	0.051	0.068	0.195

Table 5.19: Test results

The results obtained in the subsection align perfectly with the literature, which suggests that a log-normal probabilistic distribution can effectively capture the statistical variability of the realizations of the variable θ [7].

5.2.2 Calibration of model uncertainty safety factor

Bayes approach A

The number of beams analyzed in the shear failure case is more than in the flexural case, but it is still not sufficient to generalize the results obtained from this sample without further strengthening the model. It is important to get applicable results as generally as possible, rather than a representation of a limited number of RC structures. The reason

is that the approach developed in this thesis aims to create a background for future NLN analyses, ensuring a stronger alignment of the outcomes with the experimental results, but also that they contribute to the development of the next generation of international Codes. Therefore, engineers will be sure that their cases during a project have been encompassed by the established new standards.

Table 5.20: Statistical parameters of the prior information distribution functions and statistical uncertainty

Models	Prior distributions $F(\vartheta M_j)$			Statistical uncertainty	
	μ_ϑ [-]	σ_ϑ [-]	CV_ϑ [-]	$C(1,1)$	$C(2,2)$
1	1.00	0.11	0.11	6.2E-04	1.2E-03
2	0.97	0.09	0.09	3.6E-04	7.3E-04
3	0.89	0.11	0.13	7.8E-04	1.6E-03
4	1.26	0.20	0.16	1.2E-03	2.5E-03
5	1.14	0.17	0.15	1.0E-03	2.0E-03
6	1.08	0.18	0.17	1.3E-03	2.6E-03

Table 5.21: Statistical parameters of the updating information distribution functions and statistical uncertainty

Models	Updating information $F_{M_j}(\theta z_j)$			Statistical uncertainty	
	μ_ϑ [-]	σ_ϑ [-]	CV_ϑ [-]	$C(1,1)$	$C(2,2)$
1	1.07	0.19	0.18	3.1E-04	6.2E-04
2	1.07	0.20	0.18	3.2E-04	6.3E-04
3	1.09	0.18	0.16	2.5E-04	5.0E-04
4	1.02	0.16	0.15	2.2E-04	4.4E-04
5	1.04	0.18	0.18	2.9E-04	5.8E-04
6	1.05	0.18	0.18	2.9E-04	5.8E-04

As already described in the previous section, to update the prior information with new information, the Bayesian updating approach is needed. This method gives the analyst the average distribution of θ and its statistical parameters like mean value μ_θ and standard deviation σ_θ . After that, the last phase requires the assessment of the model uncertainty safety factor γ_{Rd} [43]. The procedure is the same as that used in the flexural analysis and therefore, to avoid redundancy, the entire procedure is not repeated here. Instead, the focus is to highlight the results and the main differences from the previous case. The only difference is that here approach B is not carried on because it's still challenging to find literature dealing with shear failure in NLFEA with a substantial number of elements. It's not worth including in this work through approach B a case with fewer elements: it wouldn't add significant value to this work in terms of reduction of uncertainty. Tables 5.20, 5.21 and 5.22 summarize the information and respectively present the prior, updating, and posterior statistical parameters of the related probabilistic distributions. The posterior mean values tend to fall between the prior and updating values, demonstrating the Bayesian updating approach's ability to merge prior and new information. But in this case, the method aims to reduce the excessive positive bias present in the prior information, bringing the mean value closer to unity. This is quite evident in models 4

Table 5.22: Statistical parameters of the posterior information distribution functions and statistical uncertainty

Models	Posterior distributions $F(\vartheta M_j, z_j)$			Statistical uncertainty	
	μ_ϑ [-]	σ_ϑ [-]	CV_ϑ [-]	$C(1,1)$	$C(2,2)$
1	1.02	0.15	0.14	1.7E-04	7.4E-06
2	1.01	0.14	0.14	1.5E-04	5.8E-06
3	0.96	0.16	0.17	2.3E-04	1.4E-05
4	1.17	0.19	0.16	2.9E-04	2.1E-05
5	1.09	0.18	0.16	2.1E-04	1.2E-05
6	1.06	0.18	0.17	2.3E-04	1.4E-05

Table 5.23: Average statistical parameters $F_Z(\theta |)$

	Posterior distribution $F_Z(\theta Z)$	
	μ_ϑ [-]	CV_ϑ [-]
Average statistical parameters	1.05	0.16

and 5: the μ_θ values in the priors are 1.26 and 1.14 respectively, 1.02 and 1.04 in the updating, and 1.17 and 1.09 in the posterior distributions. Similar considerations involve the σ_θ values in models 2 and 3: starting with prior information of 0.09 and 0.11, the updating values increase up to 0.20 and 0.18, but the final posterior distributions show a significant reduction to 0.14 and 0.16.

These changes illustrate how the Bayesian updating process can refine the initial statistical parameters through each step, leading to more accurate estimates. This is explicitly highlighted by the reduction of the values $C(1,1)$ and $C(2,2)$ from an order of magnitude of 10^{-3} and 10^{-4} in the prior to 10^{-5} and 10^{-6} in the posterior distributions. Despite the decrease being significant, these values remain an order of magnitude higher than those evaluated in the flexural case.

Software A demonstrates lower standard deviations and mean values closer to 1, with consequently lower coefficients of variation. This is an indicator of more precise estimates and the statistical uncertainty values $C(1,1)$ and $C(2,2)$, which are in the first three models an order of magnitude lower than those obtained by software B. This significant difference may likely be attributed to the fact that software A is more specific for 2D RC structure analysis, where the stirrups play a key role in the failure mechanism. Software A demonstrates lower standard deviations and mean values closer to 1, with consequently lower coefficients of variation. This is an indicator of more precise estimates and the statistical uncertainty values $C(1,1)$ and $C(2,2)$, which are in the first three models an order of magnitude lower than those obtained by software B. This significant difference may likely be attributed to the fact that software A is more specific for 2D RC structure analysis, where the stirrups play a key role in the failure mechanism. As demonstrated by the PDF and CDF of Models 2 and 4 in images 5.16 and 5.17, the log-normal distribution fits well with the larger samples of the updating information, as highlighted by images 5.16b and 5.17b, where most points align closely with the line, indicating an even better alignment than in the previous case, despite the increased amount of data.

The entire process, from the prior probability distributions to the updating and posterior distributions, is illustrated in figure 5.18. The figures underline in red the final log-normal

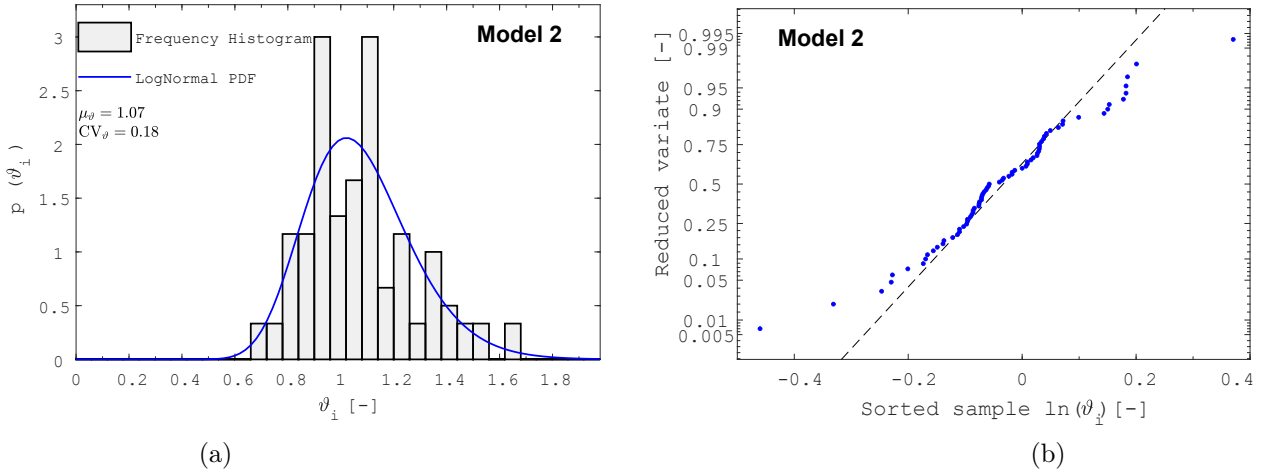


Figure 5.16: (a) Frequency Histogram vs. Lognormal PDF of θ for updating information in Model 2, and (b) Probability Plot of θ for updating information in Model 2

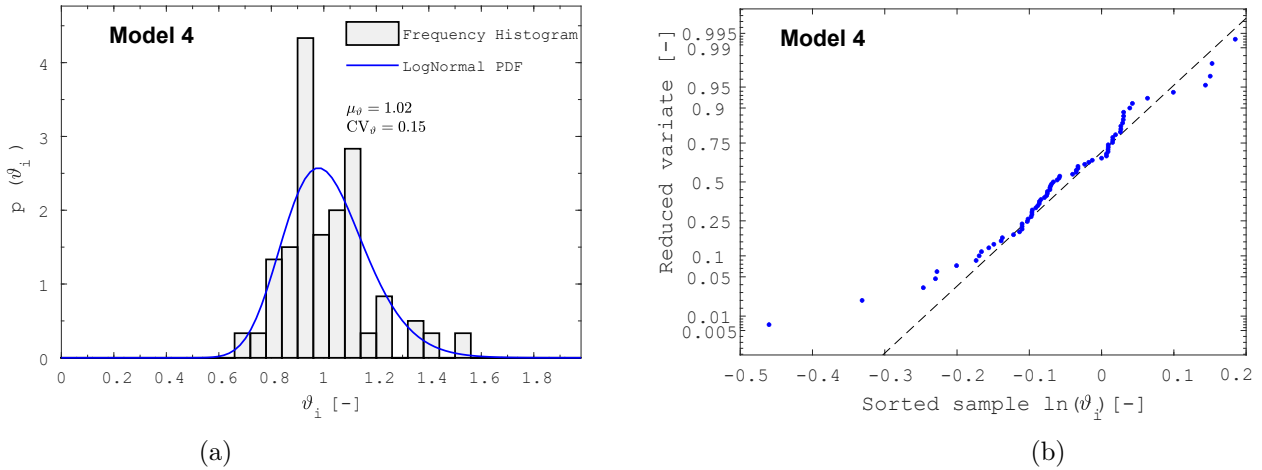


Figure 5.17: (a) Frequency Histogram vs. Lognormal PDF of θ for updating information in Model 4, and (b) Probability Plot of θ for updating information in Model 4

probability distribution, and table 5.23 presents its key statistical parameters. The next section will use these values to assess the model uncertainty safety factor γ_{Rd} . The posterior distributions, illustrated in blue in charts 5.18, fall between the more dispersed prior distributions (shown in gray) and the concentrated updating distributions (depicted in green).

According to our work, the log-normal distribution is the most suitable probabilistic model to represent the θ sample, with a mean, μ_θ , of 1.05 and a coefficient of variation, CV_θ , of 0.16. Before using them to calibrate γ_{Rd} , as explained later, the results obtained at the end of the Bayesian approach must be purified by the effect of the experimental uncertainty. The mean value above 1 indicates that the NLFEAs in the shear mechanism tend to underestimate the beam's resistance slightly, but on the other hand, the data points are quite scattered as shown by the high CV_θ . This greater variability implies a wider PDF bell, with a right-side tail that extends further into the unsafe zone, with values lower than 1. For these cases, it's important to note that some positive effects, such as confinement, are also completely omitted in this analysis.

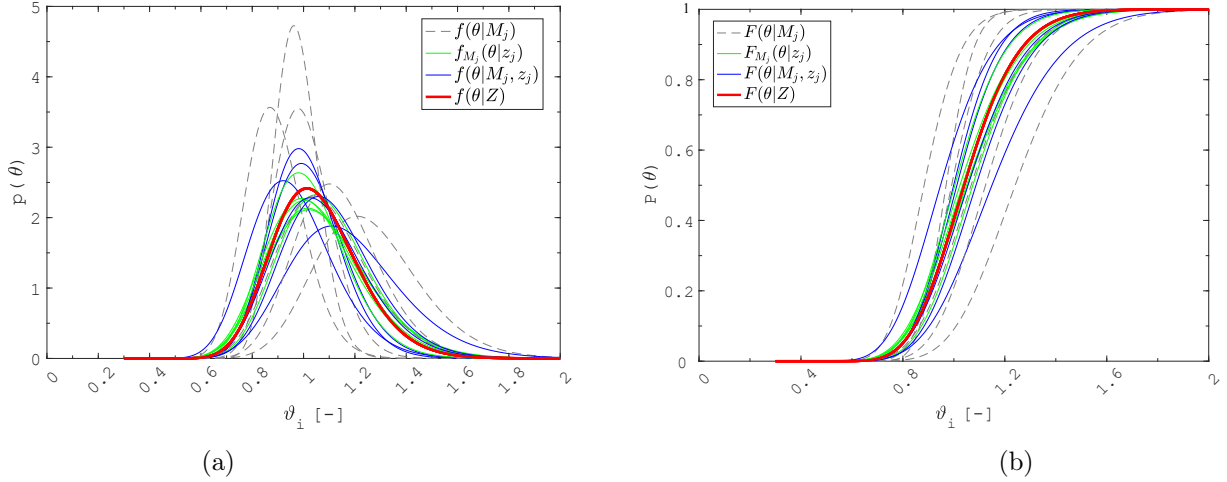


Figure 5.18: Probabilistic distributions related to prior, posterior, and updating information: Probability Density Functions (PDFs) (a) and Cumulative Distribution Functions (CDFs) (b)

5.2.3 Influence of Experimental Uncertainty

To estimate and minimize the impact of epistemic uncertainty in the GRF, a fundamental step before evaluating the model uncertainty safety factor is to isolate each type of uncertainty independently and refine the outcomes only at the end, deleting all of them through a specific safety factor. The experimental uncertainty is one of them (Reference 44 Model Uncertainty). As was done in the previous case, ε is treated as a random variable that follows a log-normal probability distribution with a mean value μ_ε equal to 1, and a coefficient of variation CV_ε of 0.05.

Experimental uncertainty arises from various factors, including geometric imperfections, misplacement of reinforcement, and imperfections related to load application. For instance, the stirrups are often assembled on-site, and their spacing may differ slightly from the technical drawings provided by the structural engineer. Similar problems can involve the angle α as well, especially during the casting phase, where it may deviate slightly from 90° .

By applying equations 5b, the $CV_{\theta,act}$ becomes slightly lower than the observed CV_θ , while the mean value $\mu_{\theta,act}$ remains exactly equal to μ_θ . Table 5.24 summarizes the key metrics for the log-normal probabilistic distributions obtained using the Bayesian method. These metrics reflect the resistance model uncertainty random variable θ , without considering the influence of experimental uncertainty ε . These results will be used in the next subsection to assess the γ_{Rd} .

Approach	Experimental uncertainty ε	Actual statistical parameters for resistance model uncertainty random variable ϑ	
		$\mu_{\vartheta,act}$	$CV_{\vartheta,act}$
A	Limited $V_\varepsilon \leq 0.05$	1.05	0.15

Table 5.24: Actual statistical parameters for resistance model uncertainty random variable ϑ

5.2.4 Assessment of the partial safety factor for resistance model uncertainty

The value of the resistance model uncertainty partial safety factor, γ_{Rd} , for RC beams, is determined by considering the target reliability index, the consequences of failure, and the FORM factor as prescribed by design codes. Another important aspect is whether the analysis involves existing or new structures, as this can affect the knowledge of the structural system's state of the art and therefore the safety factor that it needs. Based on the results of the previous section and summarized in the table 5.24, γ_{Rd} can be evaluated using equation 5.2 by adopting different target reliability values following the requirements imposed by the Codes.

The procedure follows the same method as described for the flexural case, but here, in line with the challenges highlighted during the modeling phase and the high level of uncertainty reflected by the significant $CV_{\theta,act}$, the modeling uncertainties are assumed to be dominant variables. They have more influence on the overall probability of failure compared to aleatory uncertainties, which are related to the random variability of material properties and actions. This shift in the dominant case underlines the critical task of accurately implementing NLFEMs in the shear failure analysis and relying on the outcomes.

This dominant hypothesis is supported by a $CV_{\theta,act}$ value higher than the CV value of 0.15 associated with the upper limits in the aleatory uncertainties, as noted in Bergetto's thesis. This indicates that the overall uncertainty in global resistance in the shear case, in contrast with the previous case, is primarily influenced by epistemic uncertainties, and therefore, the analyst has to choose to adopt a FORM sensitivity factor set at 0.8.

Table 5.26 presents the various values of γ_{Rd} applicable to different design scenarios, and for a more detailed analysis, table 5.25 provides γ_{Rd} values based on the assumption that model uncertainty does not dominate over aleatory uncertainty, with a FORM sensitivity factor of 0.32. For new structural systems with moderate failure consequences, a 50-year design lifetime, and $\beta = 3.8$, γ_{Rd} values proposed are 1.52 for the dominant case and 1.15 for the non-dominant case.

It is evident how the choice between the two approaches can impact the final design of the structure, reducing the resistance model uncertainty partial safety factor by roughly 25%. In practical terms, this reduction would decrease the amount of steel and/or concrete, resulting in a significant reduction in costs. However, this potential for savings may lead designers to adopt an inappropriate non-dominant factor for RC structures subjected to shear mechanisms, thereby unbalancing the previously balanced trade-off between safety and economic feasibility.

Table 5.25: Partial safety factors γ_{Rd} for RC beams in the hypothesis of non-dominant resistance variable depending on the target reliability level - Approach A

New structures	Service life	Consequences of failure	Reliability index β	FORM factor	Partial safety factor
	[Years]	[-]	[-]	α_R [-]	γ_{Rd} [-]
	50	Low	3.1	Non-dominant 0.32	1.11
	50	Moderate	3.8	Non-dominant 0.32	1.15
	50	High	4.3	Non-dominant 0.32	1.17
Existing structures	Service life		Reliability index β	FORM factor	Partial safety factor
	[Years]		[-]	α_R [-]	γ_{Rd} [-]
	50		3.1–3.8	Non-dominant 0.32	1.11–1.15
	15		3.4–4.1	Non-dominant 0.32	1.12–1.16
	1		4.1–4.7	Non-dominant 0.32	1.16–1.20

Table 5.26: Partial safety factors γ_{Rd} for RC beams in the hypothesis of dominant resistance variable depending on the target reliability level - Approach A

New structures	Service life	Consequences of failure	Reliability index β	FORM factor	Partial safety factor
	[Years]	[-]	[-]	α_R [-]	γ_{Rd} [-]
	50	Low	3.1	Dominant 0.8	1.39
	50	Moderate	3.8	Dominant 0.8	1.52
	50	High	4.3	Dominant 0.8	1.61
Existing structures	Service life		Reliability index β	FORM factor	Partial safety factor
	[Years]		[-]	α_R [-]	γ_{Rd} [-]
	50		3.1–3.8	Dominant 0.8	1.39–1.52
	15		3.4–4.1	Dominant 0.8	1.44–1.57
	1		4.1–4.7	Dominant 0.8	1.57–1.69

Conclusions

This thesis explores the application of the Global Resistance Format to estimate the design value of the global structural resistance, R_d , for RC beams subjected to flexural and shear failure. The global approach in the resistance mechanisms, involving advanced numerical methods such as NLFEMs, encompasses the progressive damage and the structure's ability to redistribute internal forces within the structures under different loading conditions. The research investigates the discrepancy between NLFE models and actual structures' performance by analyzing structural elements that show both, flexural and shear failure. The approach is based on comparing experimental results in terms of maximum load with those predicted by NLFE models and by examining these two sets of data, through the statistical inference procedure to validate the use of the log-normal distribution and the Bayesian updating process, it is possible to quantify the epistemic uncertainties that arise during the modeling phase. By assuming 3 model hypotheses that include all possible tensile concrete behaviors and cover any analyst assumptions for its constitutive law in software A and B, the results from 210 NLFEMs were gathered. The outcome of this methodology is the posterior probability function, which statistically represents the resistance modeling uncertainty random variable θ . Substituting in the R_d formula the key statistical parameters of θ , the resistance model uncertainty partial safety factor γ_{Rd} can be evaluated according to the necessary target reliability level. When analyzing the results, it's essential to distinguish the conclusions for the flexural case and the shear one. Regarding the first failure mode, partial safety factors γ_{Rd} values equal to 1.16 for Approach A and 1.08 for Approach B are found and they can be assumed as a satisfactory and consistent result, demonstrating a high level of reliability on both software. Approach B is analogous to the standard Approach A but includes 2 different phases in the Bayesian updating process, gathering information from the literature to further strengthen the model. In this case, the model uncertainty is non-dominant compared to the aleatory uncertainty, as demonstrated by a $CV_{\theta,act}$ of 0.104 and 0.098 for the approaches A and B respectively. The main difference between the 2 approaches lies in the mean values $\mu_{\theta,act}$, switching from a negative bias equal to 0.98 in approach A to 1.04 in approach B. On the other hand, the results of the shear analysis can be considered satisfactory and trustworthy as well. However, the level of uncertainty related to the modeling phase for shear failure is significantly greater, becoming the dominant factor with respect to the aleatory uncertainty. Indeed, the dominant hypothesis derives from the evaluated $CV_{\theta,act}$, which is equal to 0.15, the same value that is associated with the upper limits in the aleatory uncertainties. This means that, in the shear failure mode, the overall uncertainty in global resistance is mainly influenced by epistemic uncertainties. In this case, considering the higher level of uncertainty, the γ_{Rd} is set equal to 1.15. In the case of shear failure, only Approach A has been carried out due to the lack of comprehensive information in the literature that could help to enhance the model. Anyway, this case, even without the use of Approach B, has a positive bias with a mean value $\mu_{\theta,act}$ equal

to 1.05. Both cases are estimated under standard conditions: a new structural system, moderate failure consequences, a 50-year design lifetime, and a reliability index $\beta = 3.8$. These values reflect a moderately conservative approach that effectively addresses model uncertainties, ensuring safety and reliability in the design process. However, the Bayesian method is based on a robust framework, and it gains strength and precision by gathering more and more literature data, particularly with Approach B which can be implemented using these data as updating information in the first phase. For this reason, these outcomes should also be viewed as a preliminary benchmark, with future analyses that will further enhance them. Thankfully, with advancements in RC structural analysis, and the development and improvement of NLFE software, the research will be able to investigate deeper the shear failure mechanism in all its aspects.

The driving idea behind this research has been the objective of quantifying and minimizing the performance discrepancies between the numerical models and real structures during their service life, helping future users reduce the uncertainties related to the modeling aspect. Every model, even if the one realized with the most advanced and sophisticated tools, suffers numerical approximations and intrinsic uncertainties. This work will enable engineers to tackle the challenge of quantifying these epistemic uncertainties in NLFE analyses more efficiently.

In conclusion, image 5.19 clearly shows the dependency between the reliability index β and partial safety factor γ_{Rd} for both cases, the dominant and non-dominant hypotheses. This visualization allows to explore the trend of the safety factor varying one of the main variables that comes into play in its formula. It's worth noting the intersection for the non-dominant case between flexural problem Approach A and shear problem Approach A: the reason for this lies in the mean value $\mu_{\theta,act}$. While the flexural problem is characterized by a lower uncertainty, as highlighted by a $CV_{\theta,act}$ lower than the shear one; at the same time, the mean value of the flexural case is lower than zero, introducing a negative bias that increases the safety factor compared to the shear problem. Since the mean value appears in the denominator of the γ_{Rd} formula, it causes the intersection between the 2 curves, despite the overall lower uncertainty in the flexural case.

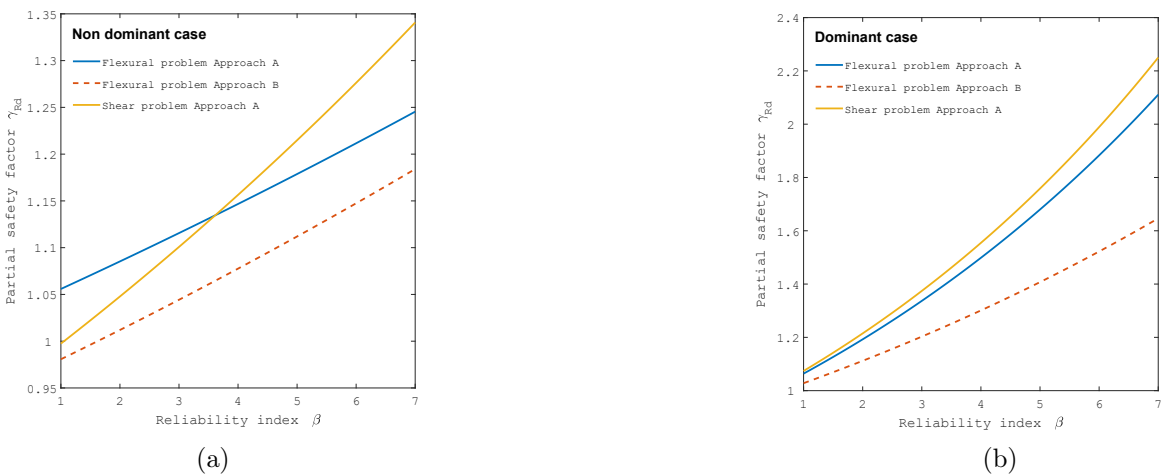


Figure 5.19: (a) Correlation between Reliability index β and Partial safety factor γ_{Rd} for non-dominant case, and (b) Correlation between Reliability index β and Partial safety factor γ_{Rd} for dominant case

Bibliography

- [1] Maria Antonietta Aiello and Antonio Bilotta. *Proceedings of Italian Concrete Conference 2022*. Springer, 2022.
- [2] Diego Lorenzo Allaix, Vincenzo Ilario Carbone, and Giuseppe Mancini. Global safety format for non-linear analysis of reinforced concrete structures. *Wiley*, 2012.
- [3] Beatrice Belletti, Cecilia Damoni, and Max A.N. Hendriks. Non-linear finite element analyses of existing reinforced concrete bridge beams. *Researchgate*, 2013.
- [4] Giuseppe Campione and Maria Letizia Mangiavillano. Fibrous reinforced concrete beams in flexure: Experimental investigation, analytical modelling and design considerations. *Elsevier*, 2008.
- [5] Paolo Castaldo, Diego Gino, Gabriele Bertagnoli, and Giuseppe Mancini. Partial safety factor for resistance model uncertainties in 2d non-linear finite element analysis of reinforced concrete structures. *Elsevier*, 2018.
- [6] Paolo Castaldo, Diego Gino, Gabriele Bertagnoli, and Giuseppe Mancini. Partial safety factor for resistance model uncertainties in 2d non-linear finite element analysis of reinforced concrete structures. *Elsevier*, 2018.
- [7] Paolo Castaldo, Diego Gino, Gabriele Bertagnoli, and Giuseppe Mancini. Resistance model uncertainty in non-linear finite element analyses of cyclically loaded reinforced concrete systems. *Elsevier*, 2020.
- [8] Paolo Castaldo, Diego Gino, and Giuseppe Mancini. Safety formats for non-linear finite element analysis of reinforced concrete structures: discussion, comparison and proposals. *Elsevier*, 2019.
- [9] Paolo Castaldo, Diego Gino, Giuseppe Carlo Marano, and Giuseppe Mancini. Aleatory uncertainties with global resistance safety factors for non-linear analyses of slender reinforced concrete columns. *Elsevier*, 2022.
- [10] The European Cement Association CEMBUREAU. The 5c approach: call for a concerted effort, 2018.
- [11] Chang-Koon Choi and Sung-Hoon Cheung. Tension stiffening model for planar reinforced concrete members. *Pergamon*, 1994.
- [12] Qian Chunxiang and Indubhushan Patnaikuni. Properties of high-strength steel fiber-reinforced concrete beams in bending. *Elsevier*, 1999.
- [13] Vincenzo Corrado, Ilaria Ballarini, and Stefano P. Corgnati. National scientific report on the tabula activities in italy, 2012.
- [14] Calogero Cucchiara, Lidia La Mendola, and Maurizio Papia. Effectiveness of stirrups and steel fibres as shear reinforcement. *Elsevier*, 2003.
- [15] A. de Putter. Towards a uniform and optimal approach for safe nlfca of reinforced concrete beams quantification of the accuracy of multiple solution strategies using a large number of samples. Master's thesis, Delft University of Technology, Delft, 2020.

-
- [16] Alessandro Dorato. Valutazione del coefficiente parziale di sicurezza per l'incertezza di modello in analisi non lineari agli elementi finiti di strutture in cemento armato soggette a caricamento ciclico. Master's thesis, Politecnico di Torino, Torino, 2019.
- [17] Hussein M. Elsanadedy, Tarek H. Almusallam, Saleh H. Alsayed, and Yousef A. Al-Salloum. Flexural strengthening of rc beams using textile reinforced mortar – experimental and numerical study. *Elsevier*, 2013.
- [18] M. Engen, M. A. N. Hendriks, J. A. Overli, and E. Alstedt. Solution strategy for non-linear finite element analyses of large reinforced concrete structures. *Elsevier*, 2015.
- [19] Morten Engen, Max A.N. Hendriks, Jochen Köhler, Jan Arve Øverli, and Erik Ålstedt. A quantification of the modelling uncertainty of non-linear finite element analyses of large concrete structures. *Elsevier*, 2017.
- [20] L. Evangelista and J. de Brito. Flexural behaviour of reinforced concrete beams made with fine recycled concrete aggregates. *KSCCE Journal of Civil Engineering*, 2017.
- [21] fib Bulletin. *Practitioners' guide to finite element modeling of reinforced concrete structures– State of the art report*. International Federation for Structural Concrete (fib), 2008.
- [22] fib Special Activity Group 5. Fib model code for concrete structures. *fib MC*, 2010.
- [23] Diego Gino. *Advances in reliability methods for reinforced concrete structures*. Phd thesis, Politecnico di Torino, Torino, 2019.
- [24] Diego Gino, Paolo Castaldo, Luca Giordano, and Giuseppe Mancini. Exact and invariant second-moment code format. *ASCE*, 1974.
- [25] Diego Gino, Paolo Castaldo, Luca Giordano, and Giuseppe Mancini. Model uncertainty in non-linear numerical analyses of slender reinforced concrete members. *Structural Concrete*, 2021.
- [26] Diego Gino, Elena Miceli, Paolo Castaldo, Antonino Recupero, and Giuseppe Mancini. Strain-based method for assessment of global resistance safety factors for nlnas of reinforced concrete structures. *Elsevier*, 2024.
- [27] EU BIM Task Group. *Handbook for the Introduction of Building Information Modeling by the European Public Sector*. European Commission, 21 european countries, 2016.
- [28] Rui Guo, Yu Ren, Mengqi Li, Peng Hu, Min Du, and Rui Zhang. Experimental study on flexural shear strengthening effect on low-strength rc beams by using frp grid and ecc. *Elsevier*, 2010.
- [29] Mostefa Hamrat, Bensaid Boulekbache, Mohamed Chemrouk, and Sofiane Amziane. Effects of the transverse reinforcement on the shear behaviour of high strength concrete beams. *Researchgate*, 2012.
- [30] M.A.N. Hendriks, A. de Boer, and B. Belletti. Guidelines for nonlinear finite element analysis of concrete structures. *Researchgate*, 2017.
- [31] JCSS. Jcss probabilistic model code, 2001.
- [32] Liu Jin, Jiangxing Zhang, Dong Li, and Xiuli Du. Meso-scale analysis of shear performance and size effect of cfrp sheets strengthened rc beams. *Elsevier*, 2022.
- [33] Chris G. Karayannis and Constantin E. Chalioris. Shear tests of reinforced concrete beams with continuous rectangular spiral reinforcement. *Elsevier*, 2013.
- [34] Chadon Lee P.E. and Jun-Yeop Kim and Seo-Young Heo. Experimental observation on the effectiveness of fiber sheet strip stirrups in concrete beams. *Journal of Composites for Construction © ASCE*, 2010.

- [35] Nathabandu T. Kottegoda and Renzo Rosso. *Applied statistics for Civil and Environmental engineers*. McGraw-Hill, 1997.
- [36] C. Lee, S. Lee, and S. Shin. Shear capacity of rc beams with carbon fiber-reinforced polymer stirrups with rectangular section. © ASCE, 2016.
- [37] Jiangxing Zhang Liu Jin, Dong Li Bo Song, Ping Li, and Xiuli Du. Effect of stirrups on shear performance of geometrically-similar reinforced concrete deep beams: An experimental study. *Elsevier*, 2023.
- [38] Hui Ma, Xiuying Gan qnd Yanli Zhao, and Zhonghui Xie. Shear performance test and nominal bearing capacity on the transfer beams of steel reinforced concrete in subway station structure. *Elsevier*, 2023.
- [39] Leonardo M. Massone, Eduardo Bedecarratz, Fabián Rojas, and Mario Lafontaine. Nonlinear modeling of a damaged reinforced concrete building and design improvement behavior. *Elsevier*, 2021.
- [40] Alberto Meda, Fausto Minelli, and Giovanni A. Plizzari. Flexural behaviour of rc beams in fibre reinforced concrete. *Elsevier*, 2012.
- [41] CEN members. Eurocode 1: Actions on structures - part 1-1: General actions - densities, self-weight, imposed loads for buildings. *Eurocodes*, 2002.
- [42] CEN members. Eurocode 2: Design of concrete structures - part 1-1 : General rules and rules for buildings. *Eurocodes*, 2004.
- [43] YKORA Miroslava and HOLICKY Milan. Assessment of uncertainties in mechanical models. *ResearchGate*, 2013.
- [44] Nadine Pressmair, Florian Brosch, Mathias Hammerl, and Benjamin Kromoser. Non-linear material modelling strategy for conventional and high-performance concrete assisted by testing. *Elsevier*, 2022.
- [45] M. A. Rashid and M. A. Mansur. Y. Reinforced high-strength concrete beams in flexure. *ACI Structural Journal*, 2005.
- [46] Filippo Sangiorgio. *Safety Format for Non-linear Analysis of RC Structures Subjected to Multiple Failure Modes*. Phd thesis, KTH Royal Institute of Technology, Stockholm, 2015.
- [47] Arthur Slobbe, Árpád Rózsás, Diego L. Allaix, and Agnieszka Bigaj van Vliet. On the value of a reliability-based nonlinear finite element analysis approach in the assessment of concrete structures. *Wiley*, 2019.
- [48] Baoyin Sun, Zhenrui Zeng, Yantai Zhang, Wei Shen, and Jinping Ou. An effective geometric nonlinear analysis approach of framed structures with local material nonlinearities based on the reduced-order newton-raphson method. *Elsevier*, 2023.
- [49] Muhammad Tahir, Zhenyu Wang, Kanwar Majid Ali, and Haytham F. Isleem. Shear behavior of concrete beams reinforced with cfrp sheet strip stirrups using wet-layup technique. *Elsevier*, 2019.